NANYANG
TECHNOLOGICAL
UNIVERSITY

OPEN WATER DISPOSAL OF BARGED SEDIMENT

ER JENN WEI

SCHOOL OF CIVIL AND ENVIRONMENTAL ENGINEERING

2017

OPEN WATER DISPOSAL OF BARGED SEDIMENT

ER JENN WEI

School of Civil and Environmental Engineering

A thesis submitted to the Nanyang Technological University
in fulfillment of the requirement for the degree of
Doctor of Philosophy

2017

Acknowledgement

First and foremost, I would like to express my sincere gratitude to my supervisor, Prof. Adrian Wing-Keung Law for spending his countless hours on discussion, guidance, and assistance while I was performing research, and writing this report. His professionalism and spirit of pursuing excellence in both science and engineering have deeply influenced me.

I would also like to thank my co-supervisor, Dr. E. Eric Adams, for his persistent help and support. He has been a role model to me for his rigorous thinking, professionalism and peacefulness in mind. I'm also very grateful to Eric and his wife for their hospitality during my stay in MIT.

I would like to recognize my colleagues, who are also my mentors, within the project team. I would like to thank Dr. Zhao Bing, Dr. Adrian Lai, Dr. Wang Ruo-Qian and Dr. Tree Chan for sharing their knowledge and experience with me. I would also like to acknowledge the financial support by the Singapore National Research Foundation (NRF) through the Singapore-MIT Alliance for Research and Technology center (CENSAM-IRG).

My work would have also not been possible without the assistance of many people in Hydraulics Modeling Laboratory and CENSAM Laboratory. I would like to show my gratitude to our lab officers: Mr. Foo Shiang Kim, Mr. Alwi Alkaff, Mr. Lim Kok Hin, Mr. Chia Key Huat and Ms. Tin Zar Lwin for their help and support on technical and administrative matters.

There are also friends who share my joy and pain, and make my graduate study a colorful and enriching journey. I would like to acknowledge Dr. Aaron Chow, Dr. Jiang Baoxin, Dr. Xie Chen, Mr. Ashish Nayan, Mr. Masoud Pourbozorg, Mr. Irvan

Luhung, Ms. Azusa Naota, Ms. Ishita Shrivastava, Ms. Cindy Wang and many others inside and outside NTU, in Singapore and elsewhere.

Last but not least, I would like to show my deepest gratitude and love to my family especially my parents for their dedication and support. Finally, I would like to specially thank my girl friend, Ms. Trinh Ha Linh for supporting my every decision, and tolerating my shortcomings.

Table of Contents

Summary

With the continuous growth of population and economy in coastal cities, dredging and land reclamation have become key activities to maintain the navigable depths in the ports and shipping channels for maritime industry, and increase the land for infrastructure development. The nature of these activities involves the disposal of sediment (i.e. reclaimed and dredged material) to a designated site during one of the stages in the projects. There are two major concerns associated with the open water sediment disposal, the accuracy of sediment placement and the loss of any associated contaminants into the ambient water. Therefore, it is essential to study the near-source sediment transport mechanisms in order to develop a better engineering model and improve the environmental assessment.

In the real disposal operation, bottom-split barge is commonly deployed to transport and dispose sediments, due to their large carrying capacity. Upon reaching the designated disposal site, the bottom of barge will open through which the sediments are released into the ambient water. The shear force at the sediment-water interface causes the leading sediments to roll up and form a sediment cloud with vortex ring structure. This is followed by a steady plume feeding sediment, momentum and buoyancy into the vortex ring. When the sediments are completely discharged from the barge, the disposed sediments then descend as a discrete sediment cloud, which behave like a single-phase miscible thermal with equivalent excess buoyancy. Thus, the dynamic behavior of a sediment cloud involves three regimes: (i) starting plume regime; (ii) thermal regime; and (iii) dispersive regime, when the sediment cloud descent velocity decreases to the level of individual particle settling velocity. This development process differs from the conventional view, which assumes the sediments are instantaneously released and experienced an initial acceleration regime before entering the thermal regime. Such conventional

view is therefore inaccurate for large volume releases, especially during the event of barge disposal.

Previous engineering models typically simplified and simulated the motion of barge-disposed sediments as three-dimensional (or axisymmetric) sediment thermal (i.e. instantaneous release from point source). This assumption enabled an efficient analysis but did not accurately represent the realistic manner as discussed above. The present study first developed a model, BSDM (Barged Sediment Disposal Model) to assess the behavior of sediment cloud due to barge disposal in the convective descent phase. BSDM considered the actual physical and release conditions, with the disposed sediments descending first as a starting plume before transiting into a discrete thermal after the sediments were fully discharged. The differential spreading of the sediment cloud due to the geometry of the barge opening with a rectangular shape and finite aspect ratio was also accounted for in the model. In summary, the model classified the dynamic behavior into six different regimes (two- and three-dimensional starting plume, thermal and dispersive regimes) with each regime modeled by the respective asymptotic solutions. Overall, the model substantially improved the predictions over previous models when compared with the experimental data.

The investigation on the barged sediment disposal was then further extended to the bottom collapse phase. When the sediment cloud reached the seabed, the momentum and buoyancy force induced by the density difference (between cloud and ambient) drove the collapsed cloud to intrude the ambient along the seabed as gravity currents. As the currents progressed, the suspended sediments were gradually settled out and deposited on the seabed. In the past, the modeling of gravity currents was carried out in either constant flux or constant volume manner. However, the gravity currents due to barge disposal might experience a transition from constant flux (starting plume) to constant volume (discrete thermal). Such interplay significantly affected the momentum and buoyancy of the currents as well as the spreading behavior, but had not been addressed in the past. In the present study, a modified Box-Model was proposed to assess the behavior of gravity currents. Besides the transition (from constant flux to constant volume), the geometrical factor of the barge opening was also included, and handled with the

volume discretization approach. An experimental study was conducted for model verification. The sediment deposition profiles were measured with LAM2D (Light Attenuation Method for 2D Data acquisition). Overall, the model predictions on the evolution of gravity currents and the subsequent deposition profiles were in good agreement with the experimental data.

A new flow regime from the instantaneous release of sediments into water was discovered by Wen and Nacamuli (1996) when the source Rayleigh number is large or, equivalently, the source cloud number (ratio of particle settling velocity to characteristic circulation velocity) is lower than a critical value of 3.2×10^{-2}. The disposed sediments were observed to penetrate the ambient water as a heavy clump, which had high resistance for the water to flow through and disintegrate the sediment mixture. While descending, the outer layer sediments were peeled off by the ambient water and suspended in the tail region, resulting a long wake-like sediment cloud. This formation was also termed as wake-like formation, as opposed to the thermal-like formation, where the disposed sediments descended as a coherent sediment thermal with negligible amount of sediments left in the tail region. Finally, the last part of the present study focused on the investigation on the formation process of sediment clouds with polydispersed sediment sizes. An experimental study was conducted by releasing mixtures of sediments with up to five sediment sizes, resulting the maximum diameter ratio (diameters of the coarsest to finest particles) of 10.7. The formation process was analyzed with composite cloud number, which is defined as the ratio of buoyancy weighted settling velocity to characteristic circulation velocity. A gradual transition from wake- to thermal-like formation was observed as the composite cloud number increased. Quantitatively, this transition was verified through the decreasing trend of the sediment cloud aspect ratio (length to width ratio). By comparing the transient development of the gross characteristics, a critical composite cloud number was derived to distinguish the wake- and thermal-like formation.

List of Publications

Journal Papers

1. Er, J. W., Law, A. W. K., Adams, E. E., and Zhao, B. (2016), "Open-Water Disposal of Barged Sediments," Journal of Waterway Port Coastal and Ocean Engineering-ASCE, doi: 10.1061/(ASCE)WW.1943-5460.0000341.
2. Zhao, B., Law, A. W. K., Adams, E. E., and Er, J. W. (2014), "Formation of Particle Clouds", Journal of Fluid Mechanics, Vol. 746, pp. 193-213.

Conference Presentations and Proceedings

1. Er, J. W., Law, A. W. K., Adams, E. E. and Yang, Y. (2015). "Light Attenuation Method for 2D Data Acquisition (LAM2D) – An Innovative Calibration Method", 68th Annual Meeting of the APS Division of Fluid Dynamics, Boston, USA.
2. Er, J. W., Law, A. W. K., Adams, E. E. and Zhao, B. (2015). "Barged Sediments Disposal Model (BSDM) for the Assessment of Open Water Disposal of Dredged Material", Dredging 2015, Savannah, USA.
3. Er, J. W., Law, A. W. K., Adams, E. E. and Zhao, B. (2015). "Flow Regime Classification for Barged Sediment Disposal", 36th IAHR World Congress, The Hague, Netherlands.
4. Er, J. W., Law, A. W. K., Adams, E. E. and Zhao, B. (2014). "Formation of Bi-disperse Particle Clouds", 67th Annual Meeting of the APS Division of Fluid Dynamics, San Francisco, USA.

5. Er, J. W., Zhao, B., Law, A. W. K., Lai, A. C. H. and Adams, E. E. (2014). "Flow Regime Classification for Barged Sediment Disposal", 33rd PIANC World Congress, San Francisco, USA.
6. Er, J. W., Zhao, B., Law, A. W. K. and Adams, E. E. (2013). "Sediment disposal from a model split barge", HYDRO 2013 International, Chennai, India.

List of Tables

List of Figures

List of Symbols

A	Dimensionless cross-sectional area of two-dimensional current
A_1	Opening area of the vessel or disposal bin
A_o	Inner area of the vessel of disposal bin
a	Cross-sectional area of two-dimensional current
B_o	Total buoyancy excess
b_o	Buoyancy per unit length
C_D	Drag coefficient
C_M	Added mass coefficient
C_S	Coefficient of sediment number
D	Ratio of current height to water depth (h_c/h)
D_b	Disposal bin height
D_o	Depth of sediment layer in the disposal bin
d_c	Diameter of hemispherical copper cup
d_p	Diameter of individual particles
d_{50}	Median diameter of individual particles
Fr	Froude number
F_B	Total buoyancy force
f	Friction factor
$f_{\mathrm{A,B}\ldots}$	Profile function
$f_{1,2\ldots}$	Function
g'	Reduced gravitational acceleration
H_c	Normalized current height
h	Water depth or depth of interest
h_c	Height of gravity current (or current height)
h_o	Initial height of gravity current
h_s	Sediment deposition thickness

h_x	Current height as a function of x
$K_{1,2\ldots}$	Coefficient
L	Disposal bin length
l_c	Cloud length
Nc	Cloud number
Ncc	Composite cloud number
Q	Normalized flux for gravity current flux
Q_o	Buoyancy flux
q	Flux for gravity current
q_o	Buoyancy flux per unit length
r_T	Cloud radius (or cloud radius in the transverse direction)
r_m	Radius of circular coordinate
r_o	Initial cloud or plume radius
r_s	Source radius for axisymmetric current
r_{50}	Median radius of individual particles
Re_p	Particle Reynolds number
S	Sediment number
t	Time
t_e	Fully discharged time
U_c	Normalized velocity of current front
u_c	Velocity of current front
u_f	Velocity based on frontal position or frontal velocity
u_{in}	Insertion speed
V	Total volume of material being disposed
V_c	Volume of gravity current
V_o	Total volume of sediments or particles in a single release
V_T	Total volume of ambient water
v	Kinematic viscosity
W	Barge opening width
W_b	Disposal bin width
w_s	Settling velocity of individual particles
x_c	Distance of current front
x_r	Spreading distance of axisymmetric current

x_l	Spreading distance of line or plane current
x_N	Spreading distance of currents
z_b	Tail position of sediment cloud
z_c	Penetration depth based on centroid position
z_{crit}	Critical depth of transition
z_d	Dispersive depth
$z_{d\mathrm{2D}}$	Dispersive depth of two-dimensional sediment cloud
$z_{d\mathrm{3D}}$	Dispersive depth of three-dimensional sediment cloud
z_e	Empty depth
z_f	Penetration depth based on frontal position
z_{fall}	Fallout height
z_t	Transition depth
α	Growth rate or spreading rate or entrainment coefficient
α_c	Growth rate or spreading rate or entrainment coefficient based on centroid position
α_f	Growth rate or spreading rate or entrainment coefficient based on frontal position
β	Settling number or normalized particle settling velocity
Δ	Normalized density difference
η	Shape factor, height to width ratio
ρ_B	Average density of disposed material in vessel or disposal bin
ρ_a	Density of ambient fluid
ρ_o	Initial density of thermal
ρ_s	Density of individual particles
Γ	Position vector relative to the axis
ν	Kinematic viscosity of water
ω	Barge opening speed or angular velocity
ω_E	Laboratory scale barge opening speed
ω_F	Field scale barge opening speed

Chapter 1

Introduction

In this chapter, the background information of open water sediment disposal is first introduced in Section 1.1, and the existing engineering models are discussed in Section 1.2. The development processes of sediment clouds are described in Section 1.3. The objectives and scope of present study are presented in Section 1.4. Section 1.5 outlines the contents included in this report.

1.1 Background

Open water sediment disposal is often practised in various activities such as land reclamation and management of dredged material. Land reclamation is the process of creating new land for infrastructure development, ecosystem protection, and so on, by filling water-covered areas with fill material. On the other hand, dredging is an activity that excavates the soils from water-covered areas for the purpose of increasing navigable water depth (improvement dredging), maintaining navigable water depth (maintenance dredging) or removing contaminated sediments (remediation dredging). Given the nature of dredging operations, the processes involve removing, transporting and disposing great amount of dredged material, which must be carefully managed to ensure the operations are completed in a cost-effective and environmentally safe manner. As a relatively low-cost solution, the dredged material is usually being disposed back to a designated disposal site, with two major disposal methods (Herbich, 2000): (i) direct open water and (ii) confined disposal. Direct open water disposal refers to the placement of dredged materials in rivers, lakes or oceans; while confined disposal is the placement of dredged material within diked islands or confined disposal cells (CAD) via barges, pipeline or hopper dredges. In general, direct open water disposal poses greater threat to the surrounding environment, as the disposed sediments are more susceptible to be carried away by ambient disturbances, such as waves and tidal currents. The establishment of engineering models is necessary to understand the transport of disposed sediment under different source conditions, and assess the impact on the environment around the disposal sites.

In the following, the current status of dredging and land reclamation in Singapore and United States is introduced in more detail.

1.1.1 Land Reclamation in Singapore

In Singapore, high population density and fast industrial development have created a constant need to reclaim land from the foreshore for various development projects along the coastal line, especially for airports, industrial, housing and recreation parks. The massive land reclamation started in 1965 and Singapore has increased its size by 23%, from 583 km^2 in 1965 to 716 km^2 in 2014 (Ho and Rajabifard 2016). The most recent Population White Paper (released on 29 January 2013, URL: http://www.population.sg/) reports that the population in Singapore is projected to reach between 6.5 million and 6.9 million by 2030. In order to support the growing population, the reclamation plan is to further increase its land to 766 km^2 (Ministry of National Development, released on 31 January 2013, URL: http://www.mnd.gov.sg/landuseplan/).

The calm wave environment and moderate tidal range prevailing along the coastline of Singapore, has enabled the reclamation work to be executed quite easily and economically. The tides in Singapore waters are predominantly semi-diurnal with mean and maximum tidal ranges of 2.3 m and 3.4 m, respectively. The current speed is generally weak, ranging from 0.1 – 0.2 m/s near shore and with maximum speed of about 2 m/s in deep water (information available on URL: http://www.nea.gov.sg/weather-climate/forecasts/tide-information). The waves of the southeast coast consist partly of wind generated waves and partly refracted swell penetrating from the east from the South China Sea during the NE-monsoon period; the maximum significant wave height is 0.6 m. Dredging is often carried out for routine maintenance of navigation channel and for port construction activities. The disposal of large quantities of dredged material poses a severe problem in Singapore, as there are limited approved disposal sites. Hence, coupling with the desire for sustainability, conversion of the dredged material to useful products is being explored.

The cost of reclamation is expected to increase as the reclamation work reaches deeper water depth such as 20 m or even more. Another factor contributing to the increasing cost of land reclamation is the lack of fill materials. Due to both environmental and political concerns, Singapore has faced difficulties importing sand from neighboring countries. Therefore, the need to fully utilize available sand material and avoid losses during reclamation operations becomes important to Singapore.

1.1.2 Dredging in the United States

The United States began to monitor and regulate dredging activities in 1972 with the establishment of the Clean Water Act as the guidelines for the discharge of dredged or fill material. The regulations and guidelines of dredged materials disposal in rivers and oceans are managed and published by U. S. Environmental Protection Agency (USEPA) in conjunction with the U. S. Army Corps of Engineers (USACE). These guidelines satisfy the National Environment Policy Act, Clean Water Act, and Marine Protection, Research and Sanctuaries Act and the state water quality regulations.

The Navigation Data Center of the Institute of Water Resources at the USACE collects data on dredging projects for all US navigable waterways and is publicly accessible though its website. The historical cost and dredged volume data between 1963 and 2012 are reproduced as bar charts in Figures 1.1 and 1.2. The USACE is primarily deployed for emergency situations or when industrial dredges are not available, and this accounts for about 20 % of the annual dredging volume (Eisma, 2006). The data shows that the annual dredging cost increased sharply in the year 1970s, remained about constant at 450 million dollars (M$) from 1980 to 1996, then increased steadily again after that and reached a maximum in 2010. However, the dredged volume showed a gradually decreasing trend from then. This might be due to the increased environmental restrictions on dredging and the subsequent disposal operations, which at the same time leads to the increase in the average cost per cubic meter.

To assess the geometrical and ecological conditions at the disposal site and collect information for scientific and public usages, all offshore disposal sites from Long Island to Maine are monitored by New England District of the USACE through DAMOS (Disposal Area Monitoring System) program started in 1977. The DAMOS monitoring surveys fall into two general categories: confirmatory studies and focused studies. Confirmatory studies are performed after the placement of dredged material in active disposal sites and the data are evaluated for strategic management. Focused studies are also performed periodically in inactive or historical disposal sites, and the data are evaluated for improving the placement and capping techniques in the future. The monitoring information is documented in technical reports and freely available online. For example, among the current active open water disposal sites in New England district, the water depths ranged from around 20 m in New London Disposal Site to 90 m in Massachusetts Bay Disposal Site.

1.2 Engineering Assessment Models

With the continued strengthening of environmental regulations, the assessment of environmental impact prior to the approval of disposal operations is typically required by the regulated agencies. Several engineering models had been developed in the past decades to model the dynamics of disposed sediments under various conditions and for different purpose. The transport processes of the disposed sediments are categorized into near and far field regions, distinguished by the mechanisms that govern the mixing and dynamics of the sediment clouds. Sediment clouds within the near-field region are driven by momentum and buoyancy, which is induced by the density difference between cloud and ambient fluid. From field evaluations, Bokuniewicz *et al.* (1978) summarized the fate of disposed sediments in this region into three sequential phases: (i) convective descent phase, during which the flow behavior is dominated by the release and source conditions; (ii) dynamic collapse phase upon impact with the seabed, during which horizontal spreading occurs; and (iii) passive-transport dispersion phase (or intermediate far-field), when the sediments are carried by the ambient currents and turbulence.

A summary of the models that were established to assess the behavior of sediment clouds in the near field region is illustrated in Figure 1.3. Reading the diagram bottom-up, Koh and Chang (1973) introduced the first model (referred as K&C model) for the short-term spreading of dredged material disposal in open sea. A following study by Brandsma and Divoky (1976) modified the K&C model to include the long term diffusion and came up with two models: DIFID (Disposal from an Instantaneous Dump) and DIFCD (Disposal from a Continuous Dump). A combination of these two models was then developed for the simulation of dredged material disposal from a hopper dredge (DIFHD). Johnson (1990) argued that the disposal of dredged material from a hopper usually has relatively high water content and the disposal operation is observed to be semi-continuous at the beginning of disposal. Johnson and Fong (1995) then combined and updated these models to propose the Short-Term FATE model (STFATE), which models the instantaneous disposal of material from hopper dredge and discretizes the initial semi-continuous release into a sequence of sediment clouds. To date, STFATE remains as one of the most popular tools in the field for engineering assessment.

There are two other models that were established for different purpose, with the basic formulation mainly following K&C model or STFATE. In the event of multiple discrete disposals, MDFATE (Multi-Dump FATE model) was created to simulate the change in bathymetry from numerous disposal events over a certain period. MDFATE simulates each disposal event using STFATE and LTFATE (Long-Term FATE model), which is the model used for long-term spreading. In addition, CDFATE – DROPMIX was designed to analyze the transport of high water content material (such as sediment plumes or slurry) that resulted from a continuous release. This kind of release conditions is modeled as a negatively buoyant jet, in which the jet will sink due to its density being greater than that of the ambient water. The sediments will then spread horizontally when reaching the bottom.

1.3 Development of Sediment Clouds

Figure 1.4 proposed a classification scheme to categorize the development of sediment clouds into three different processes (i.e. P1, P2 & P3) based on the source and release conditions, where z_{a-t} and z_e are the length of the acceleration regime and the empty depth, respectively. The scheme first compares these two physical length parameters to determine the type of release (i.e. instantaneous or continuous). The pictorial description of each development process is illustrated at the end of the scheme, the entrained fluid is presented as grey-colored fluid and sediments are shown in brown dots. The examination of this classification scheme is discussed in Appendix A and supported by an experimental study that described later in this report.

In general, the dynamic behavior of disposed sediments in the convective descent phase under homogeneous stagnant ambient conditions can be divided into three regimes (Rahimipour and Wilkinson 1992), including: (i) initial acceleration regime, within which the sediments become well mixed with water and descend as a solid body; (ii) thermal (or self-preserving) regime, within which the sediment cloud behaves self-similarly and starts to decelerate due to the entrainment of ambient stagnant water; and (iii) dispersive (or swarm) regime, within which the velocity of sediments slows to the level of individual particle settling velocity. Previous studies and the engineering models discussed in Section 1.2 are focused on the thermal regime, in which the sediment cloud is characterized by a coherent vortex ring structure. Its gross characteristics behave like a single-phase miscible thermal and can be modeled by using the asymptotic solutions:

$$\text{Two-dimensional thermal: } z \sim t^{2/3} \tag{1. 1}$$

$$\text{Three-dimensional thermal: } z \sim t^{1/2} \tag{1. 2}$$

where z is the penetration depth and t is the time. This development process (referred to as P1 in Figure 1.4) is classified as the thermal-like formation process by Zhao *et al.* (2014), who found that this regime occurred following the instantaneous release of sediments with source cloud number, *Nc* higher than 3.2×10^{-2}. The *Nc* is defined as the ratio of the settling velocity (w_s) of individual particles to the characteristic circulation velocity (w_t) within the sediment cloud.

In recent studies, two new development processes have been identified with different initial regimes: clump regime (Wen and Nacamuli 1996, Zhao *et al.* 2014) and starting plume regime. Similar to P1, the clump regime (P2 or wake-like formation process) occurs due to the instantaneous release of sediments, but with *Nc* lower than 3.2×10^{-2}. As illustrated in Figure 1.4, the clump regime features fast descending sediment clump(s), with sediments shedding along its path. The fundamental difference between clump and acceleration or thermal regimes is that the water flows around or through the sediments, respectively. During the acceleration regime, sediments are well mixed with the ambient water, and they move as a ballistic volume without losing significant sediment to the wake. The transition from clump to thermal regime is only possible if the sediment clump disintegrates within a short distance, so that the entrainment velocity at the rear of the leading vortex is strong enough to incorporate all the sediments lost in the wake into the sediment thermal.

The starting plume regime (P3 process) is expected when significant amounts of sediments are released in the disposal operation, and they require certain duration to be fully discharged. During this period, the sediments are continuously released into the ambient fluid from the source. The sediment cloud (or sediment plume in this case) is characterized as a thermal-like front head followed by a trailing stem. The gross characteristics can be modeled with the asymptotic solutions:

$$\text{Two-dimensional starting sediment plume: } z \sim t \tag{1. 3}$$

$$\text{Three-dimensional starting sediment plume: } z \sim t^{3/4} \tag{1. 4}$$

Unlike the clump regime, the sediments in the tail region will continuously supply the front head instead of becoming suspended in the water column. After the sediment is fully discharged, the sediment cloud will descend as a discrete thermal without leaving a great amount of sediment behind.

In summary, three development processes are classified based on the experimental observations reported in previous studies and in consideration of the realistic physical condition.

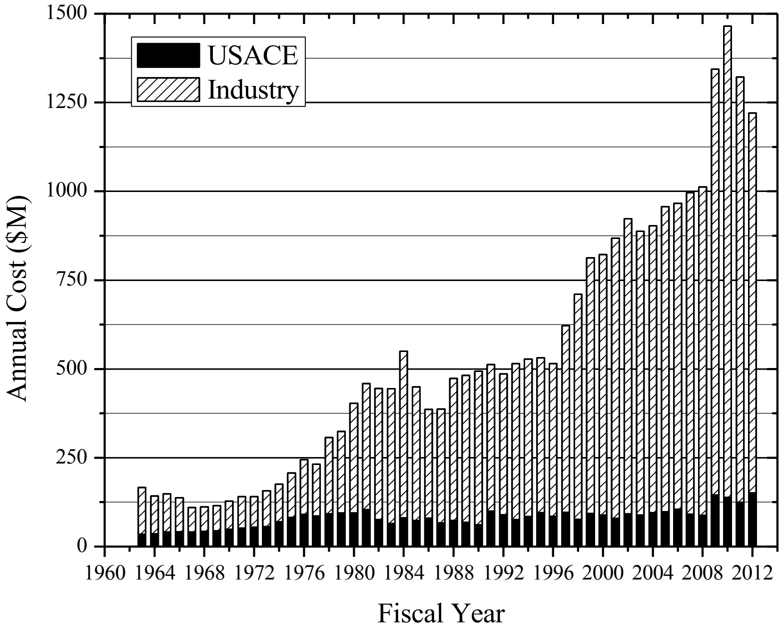

Figure 1.1 Actual dredging cost in US for the period 1963 – 2012

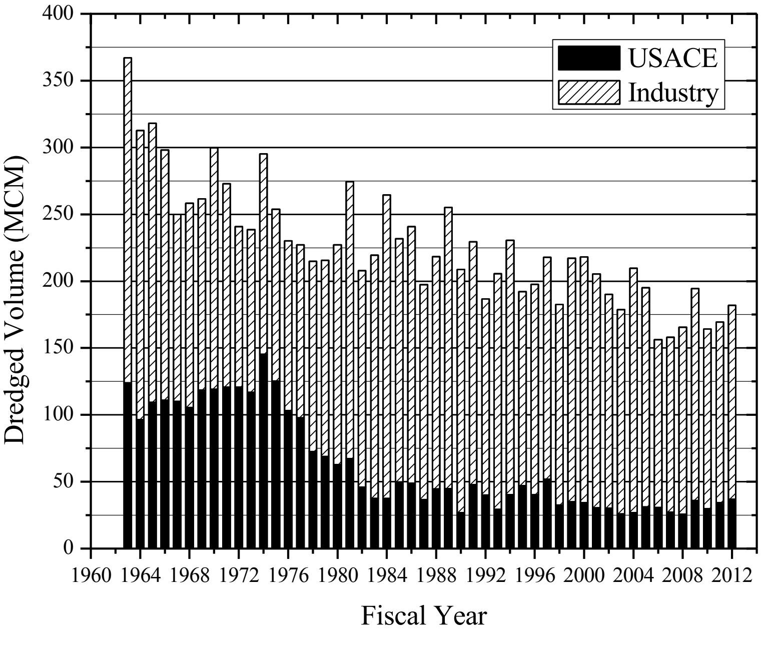

Figure 1.2 Total volume (cubic meters) of bottom sediments dredged in the US from 1963 – 2012

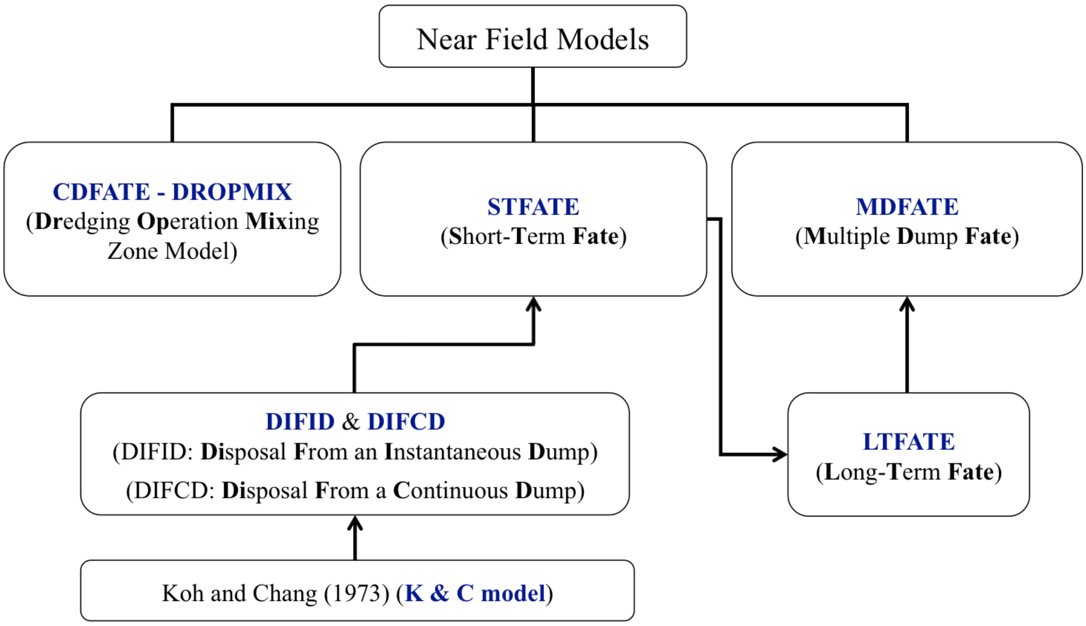

Figure 1.3 Summary on engineering models for near-field region

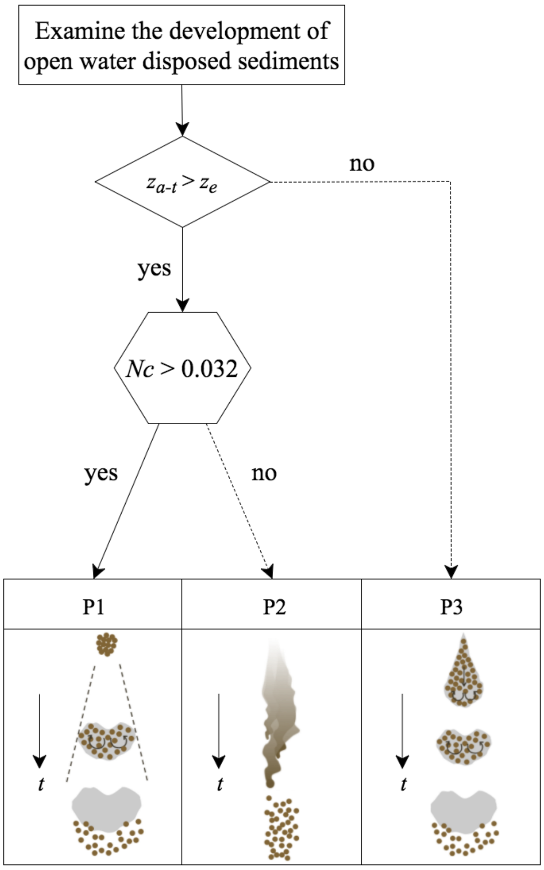

Figure 1.4 Classification of sediment clouds development processes

1.4 Objectives and Scope

If the water depth is sufficiently deep, the sediments will eventually become fully discharged and descend as a discrete sediment thermal (experiencing thermal regime), before entering the dispersive regime. Under this idealized condition, the existing engineering models are valid and appropriate for the assessment. However, the water depth in real operations is relatively shallow and in many cases, the thermal regime will not even form before the sediment clouds reach the seabed. This is especially true for large volume releases. Hence, incorporating the regimes prior to the thermal regime (i.e. acceleration, clump and starting plume) into the engineering model is more appropriate and realistic.

The present study proposes a model for assessing the behavior of sediment clouds and the subsequent gravity currents due to open water disposal from bottom-split barges, which are commonly employed in real operations due to their large carrying capacity (Eisma 2006). The model takes into account the realistic physical conditions in which sediments, due to the large and finite amount of sediment typically carried by the barge, will initially descend as a starting plume (as if from a continuous release) and then transit into a discrete sediment thermal after the barged sediments are fully discharged. Moreover, the model also includes the geometrical factors of the barge, which can significantly affect the source conditions and thus the subsequent descent process. The P3 process in Figure 1.4 is further classified into six different regimes depending of the comparisons between various length parameters and the water depth. The classification scheme and the predictions on gross characteristics of the sediment clouds are verified with an experimental study.

Upon impact with the seabed, sediment clouds will enter the bottom collapse phase and propagate horizontally along the seabed as gravity currents. Previous studies on particle-driven gravity currents were carried out with a Box-Model in either a constant volume or constant flux manner. However, due to the transition from plume (constant flux) to thermal (constant volume) involved during barge disposal, a modified Box-Model is proposed in the present study to account for this transition. The simulation of the final deposition thickness from the gravity currents is also included in the model and tested with laboratory experiments, using an improved light attenuation method to measure the sediment thickness. The volume discretization approach introduced by Zgheib (2015) is implemented to account for the transformation of current geometries due to the geometrical factors of the barge.

In practical dredging and land reclamation operations, the sediments involved typically include multiple grain sizes. However, previous studies on sediment clouds mainly involved a uniform grain size (Rahimipour and Wilkinson 1992, Noh and Fernando 1993, Bühler and Papantoniou 2001, Bush *et al.* 2003, Zhao *et al.* 2012, Zhao *et al.* 2013a, Zhao *et al.* 2014). A recent study by Lai *et al.* (2016) proposed an integral model to simulate the behavior of poly-dispersed sediment clouds for P1 process. From an engineering perspective, the formation of P2 process poses greater threat to the environment as larger amounts of sediments can become suspended in the water column. Therefore, the remaining part of the study focuses on investigating the development processes of sediment clouds with mixed grain sizes, and examining the critical source cloud number that distinguishes the development processes of P1 and P2 under this condition.

In summary, the experimental and analytical efforts in this study intend to achieve the following tasks:

1. Establishing a model to simulate the gross characteristics of barge-disposed sediment clouds in the convective descent phase – by adopting the asymptotic solutions of the respective flow regimes, and verifying these with an experimental study;
2. Developing an improved light attenuation method (LAM2D – Light Attenuation Method for 2D data acquisition) to measure the deposition due to particle-driven gravity currents, which will be applied in the next task;
3. Modifying the existing Box-Model and applying the transformation of current geometries to model the gravity currents due to barge disposal and the subsequent final deposition profile;
4. Quantifying the effect of mixed grain sizes on the formation process of polydispersed sediment clouds – by studying the degree of thermal-like behavior through the cloud aspect ratio, and determining the critical source cloud number from the transient development of gross characteristics.

1.5 Report Organization

This report is organized into eight chapters. Chapter 1 introduces some background information regarding open water sediment disposal. The objectives and scope are also described in this chapter. Chapter 2 presents a review on the literature about sediment clouds (sediment thermals and plumes) and gravity currents. Chapter 3 introduces the experimental setups and procedures as well as the principles of measuring technique that were designed and employed in the present study. The scaling from laboratory to field scale is also presented. Chapter 4 presents the model for assessing the motions of barged-disposed sediment clouds in the convective descent phase. Chapter 5 describes the improved light attenuation method, which is designed to measure the thickness of sediment deposition in aqueous environment and is applied in the following chapter. Chapter 6 presents the modified Box-Model to simulate the spreading of barged-disposed gravity currents in the bottom collapse phase and the final deposition. Chapter 7 discusses the formation process of sediment clouds with mixed grain sizes and determines a critical source cloud number. Finally, Chapter 8 summarizes the major findings and accomplishments during the course of this study together with a recommendation for future works. Some theoretical derivations and examination of classification scheme are included in the Appendices.

Chapter 2

Literature Review

The establishment of a barged sediment disposal model involves the investigation on the descending motion of disposed sediments within the water column, and the horizontal spreading of collapsed clouds after impact with the seabed. Under realistic physical conditions, the disposed sediments will initially descend as continuous plume (behave as starting plume), and then transit into a discrete sediment cloud (behave as thermal), due to the large and finite amount of sediments involved during the barge disposal. This transition also affects the spreading of gravity currents, within which the currents are initially driven by a constant flux (from the starting plume) and transit to constant volume currents when the sediments are fully discharged. In addition, the geometrical factor (aspect ratio) of the barges can also significantly affect the motion of the disposed sediments. The volume discretization approach introduced by Zgheib (2015) is adopted in the model to account for this geometrical transformation. The reviews in this report focus on miscible thermals, starting plumes, sediment thermals, clumps and gravity currents, which are the flows that are generally expected during the disposal of sediment from a bottom-split barge.

2.1 Miscible Thermals

During the self-preserving phase, the gross behavior (e.g. bulk size and descent velocity) of an instantaneous released sediment cloud has been proven to be similar to that of a miscible thermal by both dimensional analysis and laboratory observations (Rahimipour 1994). Therefore, the term “sediment thermal” is used in this report to represent the sediment cloud in its self-preserving (or thermal) regime. For simplicity, a miscible thermal is also referred to as "thermal" in this report.

Morton *et al.* (1956) studied both turbulent plumes and thermals in a stratified ambient. Three main assumptions were made in their theoretical study on the motion of thermals: (i) the rate of entrainment at the edge is proportional to the characteristic velocity of the thermal; (ii) the horizontal profiles of mean velocity and buoyancy are similar at all heights; (iii) the local variation of density is small compared to the ambient fluid density. The first assumption was known as the "entrainment assumption", which was proposed originally by Taylor (1946), who made the same assumption for studying a rising plume of buoyant air so that no details of internal flow structure were necessary. In the theoretical model of Morton *et al.*, the shape of the thermal was assumed to be spherical.

Scorer (1957) studied the motion of thermals by releasing salt solution without initial momentum by leveling the water inside and outside the cup. The thermals were made visible by a white precipitate from a thin hemispherical copper cup with a diameter of d_c. The initial density difference was less than 15%, and was less than 5% during the measured part of the thermal motion. The thermal started to decelerate after travelling about 1.5 d_c. Based on dimensional analysis

$$u_f = \mathrm{Fr}\left(g \frac{\rho_o - \rho_a}{\rho_a} r \right)^{1/2} \tag{2.1}$$

$$r = \alpha_f z_f \tag{2.2}$$

$$kz^2 = t \tag{2.3}$$

where z_f and u_f are the frontal position and velocity of the thermal as illustrated in Figure 2.1; t is the time of travelling; r is the maximum horizontal radius (i.e. half of the maximum horizontal extend); ρ_o is the initial density of the thermal; ρ_a is the density of ambient fluid; Fr is a Froude number, being the ratio between inertia forces and buoyancy forces; α_f is the entrainment coefficient; and k is a constant dependent on the total buoyancy of the thermal. The mean values of the coefficients determined by Scorer (1957) were: Fr = 1.2, $\alpha_f = 0.25$. He also suggested that the volume of the thermal be $V = (4\pi\eta/3)r^3$ with a shape factor $\eta = 9/(4\pi)$, which represent a slightly flattened spheroid that is more realistic instead of the spherical assumption made by Morton *et al.* (1956).

Turner (1973) suggested the following similarity solutions for axisymmetric thermals in a uniform density environment originating from a point source:

$$r = \alpha_c z_c \tag{2.4}$$

$$u_c = \left(\frac{F_B}{\rho_a}\right)^{1/2} z_c^{-1} f_{\mathrm{A}}\left(\frac{\Gamma}{r}\right) \tag{2.5}$$

$$g' = \left(\frac{F_B}{\rho_a}\right) z_c^{-3} f_{\mathrm{B}}\left(\frac{\Gamma}{r}\right) \tag{2.6}$$

where F_B is the total buoyancy force; Γ is a position vector relative to the axis of symmetry; g' [$= (\rho - \rho_a)/\rho_a g$] is the reduced gravitational acceleration,; α_c is the entrainment coefficient based on the centroid position and f_A and f_B are profile functions for u_c and g', respectively. The time dependence of r_{max} and u_c can be derived using $u_c = \mathrm{d}z_c/\mathrm{d}t$, and by neglecting the internal distributions of velocity and density:

$$r \propto \left(\frac{F_B}{\rho_a}\right)^{1/2} t^{1/2} \tag{2.7}$$

$$u_c \propto \left(\frac{F_B}{\rho_a}\right)^{1/4} t^{-1/2} \tag{2.8}$$

Papantoniou *et al.* (1990) compared the motion of thermals with those of momentum puffs. Without a continuous source of buoyancy, the momentum puff eventually lost its energy to overturning and entrainment after traveling a sufficiently long distance from the source, resulting in diminished entrainment capability compared to the buoyancy driven flow. It was suggested that an increase in the ratio of initial circulation to the total buoyancy would lead to a smaller entrainment rate.

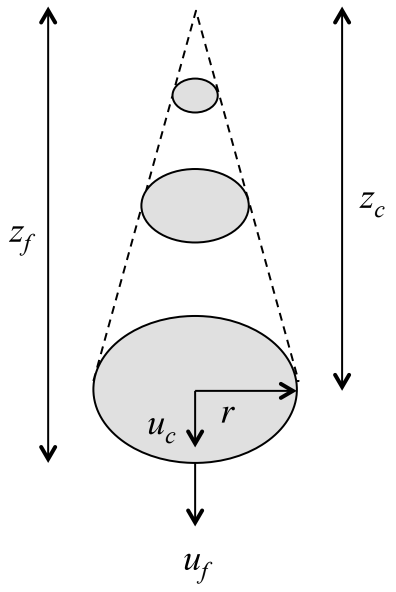

Figure 2.1 Definition sketch of single-phase thermal

2.2 Starting Plumes

The starting plume was first observed by Turner (1962) and described as a thermal-like advancing front head followed by a steady plume, as shown in Figure 2.2. Turner (1962) investigated theoretically and experimentally the motion of the advancing front of a vertical plume in neutral surroundings by emitting buoyant fluid at a constant rate from a point source. The advancing velocity of a starting plume may be less than that of a steady plume and moves with a constant fraction of the plume velocity at the same level. The entrainment rate for a three-dimensional starting plume, α_{SP} was found to be 0.174 and the proportional relationship between the front of starting plume, z_f and travelling time, t was suggested to be $z_f \sim t^{0.72 \pm 0.06}$.

Tsang (1970) conducted a laboratory study of two-dimensional starting plumes by releasing sugar and salt solutions made visible by potassium permanganate (red dye). Based on dimensional analysis, the leading edge of a two-dimensional starting plume, z_f could be expressed as

$$z_f = C\left(\frac{\Delta\rho q_i g}{\rho_a}\right)^{1/3} t \tag{2.9}$$

where C is a constant to measure the non-dimensional vorticity integration over the flow field of a two-dimensional starting plume and $\Delta\rho q_i g$ is the rate of buoyancy inflow per unit length of source. Linden and Simpson (1990) and Ching *et al.* (1993) had observed a similar relationship between the leading edge and time. They suggested the value of C to be 1 and 1.2, respectively.

Middleton (1975) developed a model to solve the three-dimensional turbulent starting plume by considering a steady plume feeding mass, momentum and buoyancy into a vortex ring. Middleton claimed that the descent velocity of the head vortex for a starting plume decays in the following manner:

$$u_f = \frac{5^{1/2}}{2\alpha^{1/2}} E^{3/4} Q_o^{\ 1/4} t^{-1/4} \tag{2.10}$$

where α is the entrainment coefficient of the steady plume; E is the ratio of mean vortex ring velocity to steady plume velocity at a height equivalent to the thermal center and Q_o is the buoyancy flux of steady plume. By integrating Equation (2.10) and substituting $\alpha = 0.09$ and $A = 0.49$ obtained from Turner's experimental result, Equation (2.10) can be converted to

$$z_f = 2.43 Q_o^{\ 1/4} t^{3/4} \tag{2.11}$$

which expresses the penetration depth of the starting plume.

Ching *et al.* (1993) carried out an investigation on the interaction between turbulent line plumes and sharp density interfaces. Through their results on the starting plume before it contacted with the density interfaces, the same relationship between the penetration depth and time as shown in Equation (2.9) was found with $C = 1.2$. They also found that the half width of the starting plume front head is linearly proportional to the penetration depth

$$r = \alpha z \tag{2.12}$$

where α is the spreading rate and has a value of 0.3 from experiments.

Ai *et al.* (2006) investigated the characteristics of both Boussinesq and non-Boussinesq starting forced plumes. The development of a starting plume was divided into two distinct periods: (i) period of flow development (PFD) and (ii) period of developed flow (PDF). They developed a similarity solution for starting plumes in the fully developed plume phase in PDF, which could be expressed as

$$z_f = 2.58 Q_o^{1/4} t^{3/4} \tag{2.13}$$

The expression was close to Middleton (1975)'s result as shown in Equation (2.11).

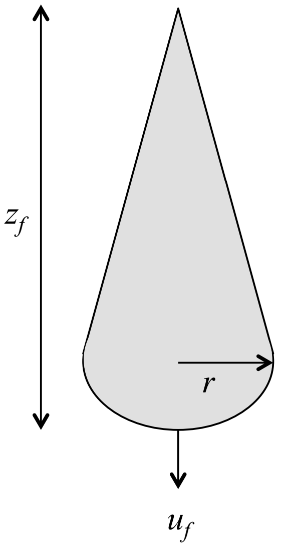

Figure 2.2 Definition sketch of starting plume

2.3 Sediment Thermals and Clumps

Koh and Chang (1973) investigated the theoretical and experimental studies on the dispersion and settling of barge disposed sediment in the ocean. They distinguished the motion of disposed sediment into 3 phases: (i) convective phase, within which the disposal sediment falls under the influence of gravity; (ii) dynamic collapse phase, occurring when the descending cloud arrives at a level of neutral buoyancy or the seabed where descent is impeded and horizontal spreading dominates; (iii) long term diffusion phase, where the transport and spreading of the sediment are dominated by ambient currents and turbulence. They developed a program to model the motion of a sediment thermal from barge disposal based on an integral approach. In their model, the sediment thermal was considered as a descending and expanding control volume, with no sediment loss during the self-preserving (or thermal) regime. The conservation equations were the same as Morton *et al.* (1956), but with the addition of added mass and drag forces as follow:

$$\frac{d}{dt}\left(\rho r^3\right) = 3\alpha_c \rho_a r^2 u_c \tag{2.14}$$

$$\frac{d}{dt}\left[V\left(\rho + C_M \rho_a\right)u_c\right] = F_B - 0.5\rho_a C_D \pi r^2 u_c{}^2 \tag{2.15}$$

$$\frac{dB}{dt} = \frac{d}{dt}V\left(\rho - \rho_a\right)g = 0 \tag{2.16}$$

where V is the volume of the thermal, assumed to be spherical (i.e. $V = 4\pi r^3/3$); u_c is the velocity of sediment cloud calculated based on the center of mass location; C_M and C_D are the added mass and drag coefficients. Equation (2.14) is based on the "entrainment assumption"; Equation (2.15) is based on the conservation of momentum due to buoyancy and drag forces; and Equation (2.16) is based on the assumption that there is no buoyancy loss to the ambient. Further simplification could be made if the Boussinesq approximation ($\rho \approx \rho_a$) is valid, and a linear relationship between the thermal radius and penetration depth could be derived from Equation (2.14) that is similar to Equation (2.4):

$$r = \alpha_c z_c \tag{2.17}$$

Krishnappan (1975) defined two stages for the motion of a sediment cloud in homogeneous ambient: (i) an initial entrainment stage, within which the cloud grew by entraining the ambient fluid; and (ii) a settling phase, within which the cloud velocity approached the settling velocity of individual particles. He also found that the growth rate was related to the particle size, and the sediment cloud behaved similarly to that of a miscible thermal when the particle size was small (d_p < 100 μm).

Buhler and Papantoniou (1991) performed laboratory experiments to simulate the dumping of rubble resulted from tunnel construction, and focused their research on the dispersive regime. The sediment cloud was found to enter the dispersive regime when the velocity of the front position of a sediment cloud reached 1.4 times the settling velocity of individual particle. The width of the sediment swarm was observed to grow linearly with the travelling distance, although the entrainment rate was much smaller than that in the self-preserving regime. They suggested that the growth in width might be caused by the wakes formed by falling particles and the random lateral oscillations of particles.

Rahimipour and Wilkinson (1992) studied the behavior of sediment cloud releases from a point source and distinguished the motion of sediment clouds into three regimes: (i) acceleration regime, within which the sediments moved as a solid body; (ii) thermal regime, within which the sediment cloud behaved like a miscible thermal, and was characterized by strong internal circulation; and (iii) dispersive (or swarm) regime, within which the sediments left the entrained fluid and settled at their own settling velocity. This development process was categorized as P1 in Figure 1.4. A cloud number (*Nc*), defined as the ratio between the settling velocity of individual particles and the characteristic circulation velocity (w_t), was proposed to govern the flow regimes:

$$Nc = \frac{w_s}{w_t} = \frac{w_s}{\sqrt{B_o / r_o}} = \frac{w_s r_o}{\sqrt{B_o}} \tag{2.18}$$

where w_s is the particle settling velocity. It was found that the growth of the sediment cloud became very slow when $Nc \approx 1.5$; thus the radius of the sediment cloud in the dispersive regime could be estimated as

$$r = 1.5\left(\frac{B_o}{\rho_a}\right)^{1/2} \frac{1}{w_s} \tag{2.19}$$

The entrainment coefficient was found to be a function of the cloud number as

$$\alpha = 0.31\left(1 - 0.44Nc^{1.25}\right), \text{ for } N_c < 1 \tag{2.20}$$

Noh and Fernando (1993) studied two-dimensional sediment clouds by releasing a mixture of fluorescent dye and glass beads from a funnel shaped release mechanism. They focused on the transition from self-preserving regime to dispersive regime of the two-dimensional sediment cloud, and visually identified the transition point by the separation of particles from the dyed parent fluid and the uniform downward motion of sediments without circulation pattern. They suggested that the critical depth of transition, z_{crit} from self-preserving to dispersive regime should not be solely determined by w_s as concluded by Buhler and Papantoniou (1991) but also by total buoyancy and ambient viscosity, v:

$$\frac{z_{crit} w_s}{v} \propto \left(\frac{b_o}{v w_s} \right)^C, C \approx 0.3 \tag{2.21}$$

where b_o is the kinematic buoyancy force per unit mass per unit length. They explained that the physical significance of w_s/v in the above equation was that the larger the ambient fluid viscosity and the smaller the particle size were, the longer in distance the self-preserving regime remained. The experimental results also showed that the size of the sediment cloud continued to grow at the same rate as that in its self-preserving phase due to the turbulence generated during that phase. They also suggested that the transition might occur when $u_f < w_s$ as long as the ambient turbulent intensity was strong enough to keep the particles in suspension.

Johnson and Fong (1995) developed a numerical model called STFATE (Short-Term FATE) for computing the water column concentration and bottom disposition resulting from a dredged material disposal operation by barge. Their model introduced the concept of multiple convecting clouds to model the disposal operation when the discharged duration had similar magnitude compared to the sediment cloud descent duration. Based on the conservation of energy and mass, the insertion speed for individual layers of sediment was expressed as

$$u_{in} = \frac{\left(\rho_{\mathrm{AV}} gh - \rho_a gh \right)}{\frac{1}{2} \rho_{\mathrm{AV}} \left[1 + f - \left(\frac{A_1}{A_o} \right) \right]} \tag{2.22}$$

$$\rho_{\mathrm{AV}} = \frac{\rho_B V_T - \sum_i \rho_i V_i}{V_T - \sum_i V_i} \tag{2.23}$$

where f is the friction factor; A_1 and A_o are the opening and inner areas of the disposal vessel; ρ_B is the average density of the disposed material in vessel; V_T is the total volume being disposed; ρ_i and V_i are the average density and volume of the individual layer in the vessel. Each layer ultimately became a convecting cloud and the convective descent phase for each layer was modeled through the three-dimensional thermal model developed by Koh and Chang (1973).

Ruggaber (2000) conducted experiments on sediment clouds by releasing silt and glass beads of various sizes into a glass tank. The cloud number (*Nc*) as proposed by Rahimipour and Wilkinson (1992) was employed to scale the sediment volume of laboratory scale to that of realistic field scale. He studied the effect of particle size, water content, and initial momentum on the behavior of sediment cloud. He found that the variation of growth rate was larger for cohesive sediment as compared to non-cohesive one. The self-preserving regime was further divided into "thermal" and "circulating thermal" regimes, and the growth rates ranged from 0.2 to 0.3 and 0.1 to 0.2, respectively. The "circulating thermal" regime was characterized by the presence of vortex ring structures. He also quantified the amount of sediment in the trailing stem using a sediment capture mechanism within the tank.

Bush *et al.* (2003) preformed experiments by releasing glass beads into both homogeneous and stratified ambients. For the studies of sediment clouds in homogeneous ambients, they found that the transition between self-preserving and dispersive regime could be quantified using the particle Reynolds number, Re_p $(=\frac{w_s d_p}{\nu})$. For particles in the range of 0.1 to 300, the fallout height (z_{fall}) of individual particles in the dispersive regime was found to be

$$\frac{z_{fall}}{d_p} = (11 \pm 2)\left[\frac{(B_o/\rho_a)^{1/2}}{w_s d_p}\right]^{5/6} \tag{2.24}$$

where B_o is total excess buoyancy. For higher particle Reynolds numbers, the relationship could be simplified and depend exclusively on the number of particles (N_p) and size of particles released as in the following form:

$$z_{fall} = (9 \pm 2) d_p N_p^{1/2} \tag{2.25}$$

The growth rate of the sediment cloud (α) was found to be independent of the initial payload mass as well as the Rayleigh number (*Ra*) and had a mean value of 0.25.

The behavior of sediment cloud in ambient currents were studied by Gensheimer *et al.* (2012). They classified the current velocity into three regimes (i.e. weak, transitional, and strong) and quantified the thresholds of those regimes for various sizes of sediments. It was observed that in weak currents, the sediment clouds behaved as if they were in quiescent conditions and was simply advected by the currents. As the current velocity increased, the vortex cores formed during the circulating thermal stage began to be damaged, and the cloud spread more widely and was slowed down due to the enhanced mixing with ambient fluid. In strong currents, the vortex structure was completely destroyed or even never formed. They also measured the sediment loss outside the designated disposal area due to ambient currents.

Zhao *et al.* (2013a) investigated the effects of regular surface waves on the instantaneously released sediment clouds. The release mechanism was synchronized with the wave generator to control the wave phase of release. The results showed that the sediment cloud was passively advected by the wave orbital motion, and there was no significant phase lag between the sediments and surrounding water particles. The growth rate of the sediment clouds was found to be similar to those in a stagnant condition. A passive advection model was proposed to predict the motion of a sediment cloud in the wave environment. This model super imposed the wave orbital velocity onto the descent velocity of the sediment cloud under the stagnant condition. The prediction was found to be in good agreement with the experimental data.

The formation of the clump regime (P2 process) was first observed by Wen and Nacamuli (1996) when investigating the effects of three nondimensional parameters on the motion of sediment cloud. They released wetted particles above the water surface through a cylinder container. By adopting the initial half-width of the sediment cloud, r_o and particle settling velocity, w_s as the length and velocity scales, respectively, the three nondimensional parameters could be expressed as: (i) Rayleigh number, Ra = $F_B/(\rho_a w_s^2 r_o^2)$; (ii) Reynolds number, Re = $(\rho_a w_s r_o)/\mu$; and (iii) Froude number, Fr = $w_s/(g' r_o)^{1/2}$. They concluded that as Ra approached the critical value of 1000, the sediments penetrated the ambient water as sediment clumps (even for the sediments in the non-cohesive range), characterized by a fast-moving particle rich core and continuously shedding particles to the tail region (wake). The entrainment rate was found to reduce drastically with limited lateral growth when the sediments formed clumps.

In a following study, Zhao *et al.* (2014) examined the relationship between the formation of clump regime and cloud number, Nc (= $1/\mathrm{Ra}^{1/2}$) with the analogy of flow passing through a porous sphere. The level of flow resistance (for water to flow through the pores) was estimated as the hydraulic gradient across the sphere and the associated seepage velocity. By considering two asymptotic cases (i.e. small and large particles), the seepage velocities of both cases could be expressed as the source cloud number, Nc. Hence, the tendency to form in the clump regime increased with a decrease in particle size and increase with volume of released. A critical cloud number ($Nc = 3.2 \times 10^{-2}$ or equivalently $\mathrm{Ra} < 10^3$ as noted by Wen and Nacamuli (1996)) to distinguish the wake- and thermal-like formation process was determined and verified through an experimental study.

Figure 4 of Zhao *et al.* (2014), which is reproduced here as Figure 2.3, presented a series of images that illustrated the gradual transition from thermal- to wake-like formation as Nc decreased. When $Nc > 3.2 \times 10^{-2}$ (Figure 2.3a), the sediments experienced the acceleration and thermal regimes (P1 process) that were mostly described and observed in other studies (Rahimipour and Wilkinson 1992, Bush *et al.* 2003, Lai *et al.* 2013). As Nc decreased, a transitional regime was observed whereby the sediments initially descended and accelerated as a heavy clump due to high flow resistance through the pores, and sediments were peeled off from the clump. When the clump reduced to a sufficiently small size, and the water was able to flow through the pores and caused the clump to disintegrate, the sediments would behave again as a dense fluid. During this transition, the clump at the front transformed into a leading thermal and engulfed the sediments in the tail region to descend together like a sediment thermal. As Nc decreased further, the sediment clumps persisted for longer distances, as the resistance for water to flow through the clumps was higher. The lateral spreading was limited by both the downward flow induced by the dense clump and the reduced turbulent entrainment compared to a particle thermal. When the leading clumps eventually disintegrated, the induced thermals were too weak to engulf all the sediments in the tail region. Therefore, the development of the frontal position after the clump disintegration did not follow closely the asymptotic solution ($z_f \sim t^{1/2}$).

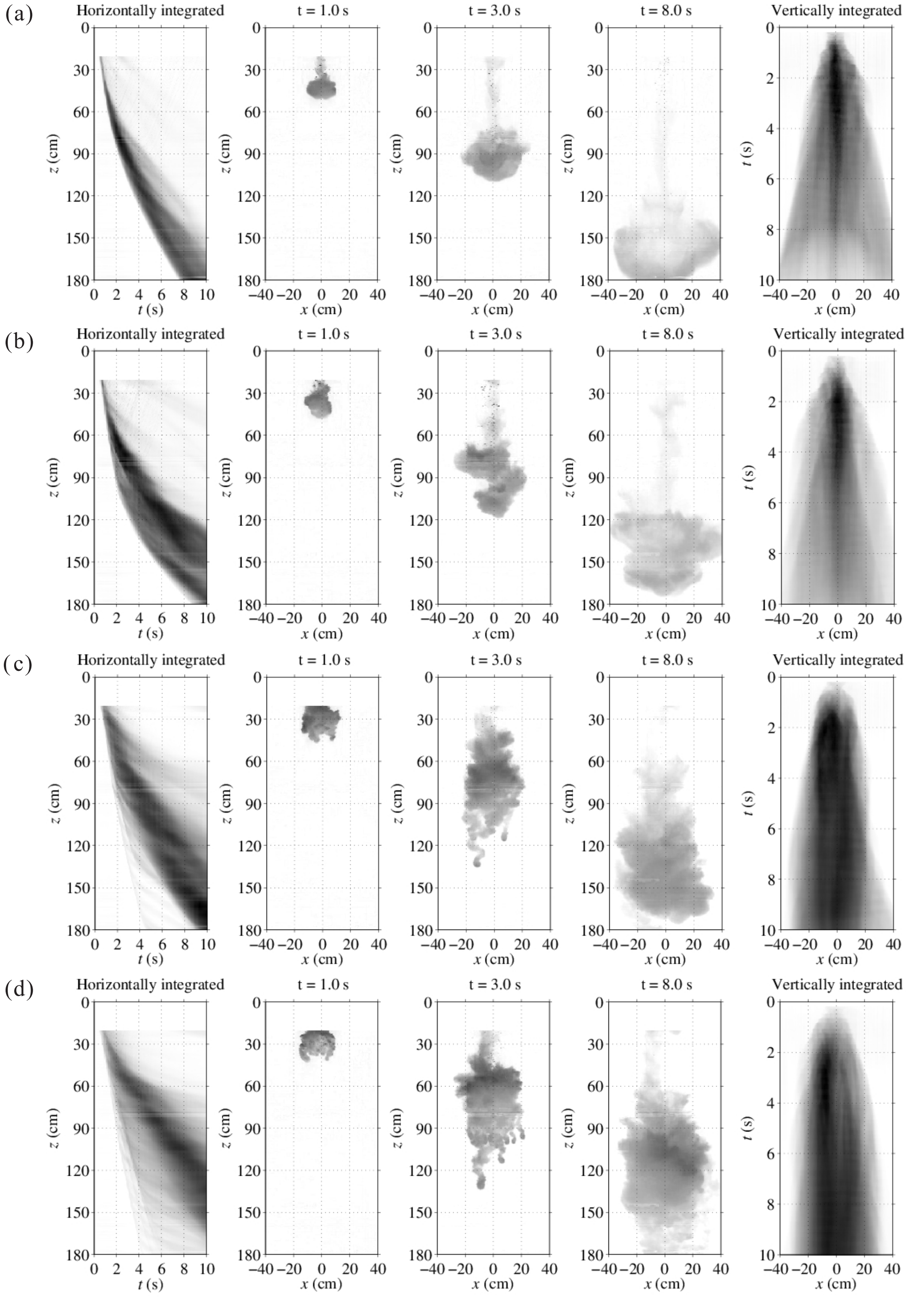

Figure 2.3 Integrated view and instantaneous images: (a) $Nc = 5.9 \times 10^{-2}$; (b) $Nc = 2.4 \times 10^{-2}$; (c) $Nc = 7.7 \times 10^{-3}$; and (d) $Nc = 2.9 \times 10^{-3}$. (Adapted from Zhao *et al.* 2014)

2.4 Gravity Currents

One of the first studies of gravity currents was Fay's (1969) observation of spilled-oil in water that tended to spread outward on the water surface in the form of a continuous layer. Fay (1969) distinguished the dynamic behavior of the spreading into three phases: (i) the beginning phase in which only gravity and inertial forces are important; (ii) an intermediate phase in which gravity and viscous forces dominate, and (iii) a final phase in which surface tension is balanced by viscous forces. He derived a mathematical expression for the spreading of an axisymmetric gravity current, x_r at the beginning phase, by balancing the horizontal buoyancy (gravity) and inertial forces, which could be expressed as:

$$x_r \sim (g'V_c)^{1/4} t^{1/2} \tag{2.26}$$

where g' is reduced gravity and V_c is the volume of gravity current. This relationship was argued to be valid until the viscous force dominated the current and balanced the buoyancy force (i.e. intermediate phase). Subsequently for a current dominated by viscous force, he determined that the spreading was as follow:

$$x_r \sim (g'V_c^2 v^{-1/2})^{1/6} t^{1/4} \tag{2.27}$$

where v is the fluid kinematic viscosity. By equating Equations (2.26) and (2.27), the time for the transition from inertial to viscous dominated current was derived as:

$$t^* = (V_c/vg')^{1/3} \tag{2.28}$$

Hoult (1972) solved the Shallow-Water equations of the currents and applied the Froude number condition, $\mathrm{Fr} = c/(g'h_c)^{1/2}$ for the current head. Through a series of two-dimensional experiments, he concluded that the best fit to the results came when $\mathrm{Fr} = (1.4)^{1/2}$ and obtained the following solutions for the spreading of the current:

$$x_l = 1.6\,(g'a)^{1/3} t^{2/3} \tag{2.29}$$

$$x_r = 1.3\,(g'V_c)^{1/4} t^{1/2} \tag{2.30}$$

where x_l and x_r are the spreading distance of the two- and three-dimensional gravity current, respectively and a is the volume of current per unit length. To derive the solutions for spreading in the viscous phase, he retained the viscous terms in the

Shallow-Water equations and neglected the inertial terms. The x_l and x_r were then expressed as:

$$x_l = 1.5(g'^2 a^4/v)^{1/8}\, t^{3/8} \tag{2.31}$$

$$x_r = 0.94(g'^2 V_c^4/v)^{1/12}\, t^{1/4} \tag{2.32}$$

where the constant coefficients 1.5 and 0.94 were determined from experiments.

Huppert and Simpson (1980) conducted a set of laboratory experiments by releasing finite volume of negatively buoyant fluids into homogeneous ambient fluid through a release mechanism called 'lock-exchange'. A finite volume of buoyant fluid was held at one end of the channel, blocked by a removable plate. When the experiment was initiated, the plate was removed instantaneously and the buoyant fluid intruded into the ambient fluid as gravity current. Two type of receiving flumes were employed in this study: (i) a 9.6 m long channel to examine the two-dimensional currents, and (ii) a sector of 12° with length of 3.5 m to examine the three-dimensional axisymmetric currents. Based on the experimental results, they distinguished the motion of gravity currents into three phases: (i) slumping phase, within which the depth ratio of current to intruded fluid ($D = h_o/h$) is greater than 0.075 and the current is retarded by the counterflow in the fluid, (ii) inertial phase, within which $h_o/h < 0.075$ and the buoyancy force of the intruding fluid is balanced by the inertial forces, and (iii) viscous phase, within which the buoyancy force is balanced by viscous force. They introduced the concept of a 'Box-Model', by assuming the currents evolved through a series of equal-area rectangles or equal-volume cylinders (i.e. $hl = a = h_o l_o$ for two-dimensional line current and $\pi h R^2 = V_c = \pi h_o R_o^2$ for three-dimensional axisymmetric current), with the current front following the Froude number conditions, which could be expressed as:

$$Fr = \frac{1}{2}\left(\frac{h_o}{h}\right)^{-1/3}, \text{for } 0.075 \le \frac{h_o}{h} < 1 \tag{2.33}$$

$$Fr = 1.19, \text{ for } \frac{h_o}{h} \le 0.075 \tag{2.34}$$

With these assumptions, Huppert (2006) derived a general solution for the spreading of currents, x_N, which can be expressed as

$$x_N = f\left(\mathrm{Fr}\right)\left(g'a\right)^{(2-n)/6} t^{(4-n)/6} \tag{2.35}$$

where f (Fr) is a function dependent on the Froude number, Fr as shown in Equations (2.33) and (2.34) under two different conditions, a is the cross-sectional area in two-dimensional (n = 0) or the volume in three dimensional (n = 1) currents.

Rottman and Simpson (1983) performed experiments with a similar setup as described in Huppert and Simpson (1980), but only focused on the two-dimensional gravity current. They observed that upon removal of the plate, the negatively buoyant fluid accelerated from rest to constant speed in a very short instance, and moved along the channel bed away from the end-wall. At the same time, a backflow was also generated by the ambient fluid above the current and flowed towards the end-wall. The subsequent motion of the backflow depended on the initial current height ratio (h_o/h). When h_o/h < 0.7, the backflow was reflected by the end-wall and propagated away from the wall with speed slightly greater than the speed of the current front, eventually overtaking the current front. On the other hand, when h_o/h > 0.8, the backflow towards the end-wall formed an internal hydraulic drop, which was an abrupt decrease in the current-ambient fluid interface. The critical h_o/h to distinguish the occurrence of different behavior was between 0.7 and 0.8. They proposed the two-layer fluid Shallow-Water equations to include the effect of backflow.

Particle gravity currents are usually found in environmental and geological phenomena like snow avalanches, sand storms and lava flows during the volcanic event. Unlike homogenous (or single-phase) gravity currents, the particles will settle out as the current propagates downstream, hence reducing their bulk density as well as the buoyancy force. Bonnecaze *et al.* (1993) studied the two-dimensional gravity currents by releasing a finite volume of suspension into water through the 'lock-exchange' release mechanism. The suspension was made by mixing monodisperse, non-cohesive silicon carbide particles with water and kept behind the gate before release. They assumed the dynamics of the currents were dominated by a balance between inertial and buoyancy forces, with the viscous force being neglected. By extension of previous successful analyses on fixed volume single-phase gravity currents (Hoult 1972, Rottman and Simpson 1983), they developed the single- and two-layer Shallow-Water equations to model the behavior of the particle-driven gravity currents. Due to the presence of particles, a transport equation for the particle concentration was derived by assuming that the particles were vertically well mixed in the current, advected by the mean flow and settled out through the bottom of the currents. The single-layer model was applied under the conditions of deep water, with negligible entrainment from ambient fluid. The three main governing equations are:

(i) conservation of mass,

$$\frac{\partial h_x}{\partial t}+\frac{\partial}{\partial x}\left(u_x h_x\right)=0 \tag{2.36}$$

(ii) conservation of momentum,

$$\frac{\partial}{\partial t}\left(u_x h_x\right)+\frac{\partial}{\partial x}\left(u_x{}^2 h_x+\frac{1}{2}g'\left(\phi\right)h_x{}^2\right)=0 \tag{2.37}$$

and (iii) conservation of particles,

$$\frac{\partial \phi}{\partial t}+u_x\frac{\partial \phi}{\partial x}=-w_s\frac{\phi}{h_x} \tag{2.38}$$

where x is the horizontal coordinate along the current, $h_x(x, t)$ and $u_x(x, t)$ are the current height and velocity field along x, respectively, and ϕ is the particle volume fraction. To solve the above equations, two boundary conditions were applied: (i) zero flow at the end wall ($x = 0$), i.e. $u_x(0, t) = 0$, and (ii) at the front of the current, $u_c = \mathrm{Fr}\,[g'\phi h_c]^{1/2}$, where Fr = 1.19 was proposed by Huppert and Simpson (1980) through experimental study. When $w_s = 0$, which is similar to the single-phase gravity currents, Equations (2.36) to (2.38) posed a similarity solution that agreed well with Hoult (1972). A two-layer model adopted the same governing equations for the gravity current layer, plus the conservations of mass and momentum for the upper (or backflow) layer, which could be expressed as

$$\frac{\partial h_u}{\partial t} + \frac{\partial}{\partial x}\left(u_u h_u\right) = 0 \qquad (2.39)$$

$$\frac{\partial}{\partial t}\left(u_u h_u\right) + \frac{\partial}{\partial x}\left(u_u{}^2 h_u\right) - \gamma h_u \frac{\partial h_x}{\partial x} + h_u \frac{\partial p}{\partial x} = 0 \qquad (2.40)$$

where p is the pressure at the interface between two layer of fluids. To reduce the number of variables, the depth and velocity of the upper layer ambient fluid (h_u and u_u) could be written in terms of the variable that described the current (h_x and u_x). Because the total depth of the two layers was fixed, the current and upper layers are related by

$$h_x\left(x,t\right) + h_u\left(x,t\right) = 1 \qquad (2.41)$$

By using Equations (2.36), (2.39) and (2.41), the boundary condition of zero flow at the end-wall could be deduced as

$$u_x\left(x,t\right) h_x\left(x,t\right) + u_u\left(x,t\right) h_u\left(x,t\right) = 0 \qquad (2.42)$$

Using the above two conditions and adding the linear combinations of equations (2.37) and (2.40), the combined two-layer momentum equation could be derived and the interfacial pressure (p) was eliminated:

$$\frac{\partial}{\partial t}\left(u_x h_x\right) + \left(1 - h_x\right)\frac{\partial}{\partial x}\left[u_x{}^2 h_x + \frac{1}{2}\left(\phi - \gamma\right) h_x{}^2\right] + h_x \frac{\partial}{\partial x}\left[u_x h_x \left(1 - h_x\right)\right] = 0 \qquad (2.43)$$

In summary, the two-layer model consisted of three main equations: (2.36), (2.38) and (2.43) for three variables: h_x, u_x and ϕ, together with the appropriate boundary conditions: (i) zero flow at the endwall, and the Fr condition at the current nose given as:

$$u_c = \mathrm{Fr}\left(g'\phi h_c\right)^{1/2} \qquad (2.44)$$

where Fr = 1.19 when $0 \leq h_o/h \leq 0.075$ and Fr = 0.5 $h_c^{-1/3}$ when $0.075 \leq h_o/h \leq 1$.

In a following study, Bonnecaze *et al.* (1995) examined the three-dimensional axisymmetric particle gravity currents for both fixed volume and constant flux releases. They proposed the single-layer Shallow-Water equations to model the currents motion with the same assumptions, and extra advective transport equation for the particles were made as discussed in their previous work (Bonnecaze *et al.* 1993). The governing Shallow-Water equations for axisymmetric (three-dimensional) cases were similar to those of two-dimensional cases, and their dimensionless form were given as:

$$\frac{\partial h^*}{\partial t^*}+\frac{1}{r^*}\frac{\partial}{\partial r^*}\left(r^* u^* h^*\right)=0 \tag{2.45}$$

$$\frac{\partial}{\partial t^*}\left(u^* h^*\right)+\frac{1}{r^*}\frac{\partial}{\partial r^*}\left(r^* u^{*2} h^*\right)+\frac{\partial}{\partial r^*}\left(\frac{1}{2}\phi^* h^{*2}\right)=0 \tag{2.46}$$

$$\frac{\partial \phi^*}{\partial t^*}+u^*\frac{\partial \phi^*}{\partial r^*}=-\beta\frac{\phi^*}{h^*} \tag{2.47}$$

where the lengths, time, velocity and particle volume fraction (ϕ) were non-dimensionalized by h_o, $(h_o/g_o')^{1/2}$, $(g_o' h_o)^{1/2}$, and ϕ_o, respectively. h_o is the characteristics height of the current, which is either the initial height of the current for the instantaneous release of a fixed volume or the height at the inlet for a constant flux of suspension and β [$= w_s / (g_o' h_o)^{1/2}$] is the settling number. Again, to close the equations, two sets of boundary conditions were employed for both release conditions. A common boundary condition was the Fr condition for the current front, which was expressed in Equation (2.44). The value of Fr for a fixed volume release was determined to be the same as for two-dimensional currents with Fr = 0.72. The second boundary condition was zero flow at the end-wall (r = 0), $u\ (0, t) = 0$, and constant flux at the source location with source radius (r_s). The flux Q_o is specified by $u\ (r_\mathrm{o}, t)\ h\ (r_\mathrm{o}, t) = Q/2\pi r_\mathrm{s}$.

Dade and Huppert (1995) derived the following analytical solutions for the Box-Model to describe the motion of a particle-driven gravity current (X_c and H_c are the dimensionless current front and current height, respectively) with constant particle volume, under both deep and shallow water conditions:

$$\text{deep water: } X_c \approx \left(A/\sigma_d{}^2\right)^{1/3} f_d\left(\sigma_d T\right),\ H_c \approx 0.68 c_d Q_o{}^{2/3} \Psi_d T^{-2/3} \tag{2.48}$$

with

$$\sigma_d = \left(\frac{\beta}{3.4 c_d A^{2/3}} \right)^{3/5}, \ \Psi_d = 1 + \left(\sigma_d T \right)^{5/3} \tag{2.49}$$

$$f_d(\sigma_d T) = -0.59 c_d^{1/2} \left[\begin{array}{l} \ln\left[1 + \left(\sigma_d T \right)^{1/3} \right] + \sum_{n=0}^{1} \cos\left\{ \frac{(2n+1)2\pi}{5} \right\} \ln\left[\begin{array}{l} 1 + \left(\sigma_d T \right)^{2/3} \\ -2\left(\sigma_d T \right)^{1/3} \cos\left\{ \frac{(2n+1)2\pi}{5} \right\} \end{array} \right] - \\ 2\sum_{n=0}^{1} \sin\left\{ \frac{(2n+1)2\pi}{5} \right\} \left(\arctan\left[\frac{\left(\sigma_d T \right)^{1/3} - \cos\left\{ \frac{(2n+1)\pi}{5} \right\}}{\sin\left\{ \frac{(2n+1)\pi}{5} \right\}} \right] - \frac{(4n-3)\pi}{10} \right) \end{array} \right] \tag{2.50}$$

and

$$\text{shallow water: } X_c \approx \left(AD^2 / \sigma_s^{\ 6} \right)^{1/7} f_s\left(\sigma_s T \right), \ H_c \approx 1.59 c_s Q_o^{\ 6/7} \Psi_s T^{-6/7} \tag{2.51}$$

with

$$\sigma_s = \left(\frac{D^{2/7} \beta}{6.9 c_s A^{6/7}} \right)^{7/13}, \ \Psi_s = 1 + \left(\sigma_s T \right)^{7/13} \tag{2.52}$$

$$f_s(\sigma_s T) = -0.29 c_s^{1/6} \left[\begin{array}{l} \ln\left[1 + \left(\sigma_s T \right)^{1/7} \right] + \sum_{n=0}^{5} \cos\left\{ \frac{(2n+1)6\pi}{13} \right\} \ln\left[\begin{array}{l} 1 + \left(\sigma_s T \right)^{2/7} \\ -2\left(\sigma_s T \right)^{1/7} \cos\left\{ \frac{(2n+1)\pi}{13} \right\} \end{array} \right] - \\ 2\sum_{n=0}^{5} \sin\left\{ \frac{(2n+1)6\pi}{13} \right\} \left(\arctan\left[\frac{\left(\sigma_s T \right)^{1/7} - \cos\left\{ \frac{(2n+1)\pi}{13} \right\}}{\sin\left\{ \frac{(2n+1)\pi}{13} \right\}} \right] - \frac{(4n-11)\pi}{26} \right) \end{array} \right] \tag{2.53}$$

where A is the normalized cross-sectional area of two-dimensional current, c_d and c_s are the coefficients, T is the dimensionless time, and D is the ratio of current height to water depth. The distributions of particle deposits were computed from the amount of particles settled at each time instant within the current length, X_N. Based on comparison with Bonnecaze *et al.* (1993)'s results, both the X_c and H_c achieved a good agreement. The comparison in particle deposition thickness was improved after the introduction of an adjustable coefficient, which was determined experimentally to be near unity.

Ungarish and Zemach (2005) clarified the slumping behavior of a homogenous gravity current of fixed volume release. They presented analytical and numerical results of single- and two-layer Shallow-Water equations with four different correlations for the Fr condition at the current nose. They showed that the slumping phase was observed in two-dimensional gravity currents for any value of h_0/h. However, for $h_0/h > 0.5$, this phase was complicated by the backward (and forward, after reflection) upper layer ambient fluid. They had also revisited the Box-Model, which was widely used for both single-phase and particle-driven gravity currents. Several defects of the Box-Model were pointed out when applied to model the slumping phase: (i) the Box-Model failed to predict this phase under a deep ambient condition ($h_o/h < 0.075$), whereas both the Shallow-Water predictions and experiments indicated a short but obvious slumping phase, (ii) the constant velocity predicted by the Box-Model was not truly constant, and (iii) the reliance on Froude number (Fr) correlations received no theoretical backing. Despite the problems, the Box-Model remarkably could produce accurate predictions with tolerable error (< 10%). They argued that the Box-Model was good to be used as a guiding approximation of the propagation, but not for the initial slumping phase.

Nguyen *et al.* (2012) simulated the convective descent of two-dimensional sediment clouds and the propagation of gravity currents using a two-phase flow model under both stagnant and ambient current conditions. To justify the simulated results, they performed an experimental study by releasing the sediments from a barge-like release mechanism. From the simulated and experimental results, the current fronts were observed to increase linearly with time at the beginning (i.e. constant spreading rate), before the spreading rates reduced with time (t^n, $n < 1$) due to the particles settling out from the currents, and hence reducing the buoyancy force. The spreading rates were affected by the initial solid concentration and the released volume. The effect of particle size was only observable at large t, when the larger particles settled out faster than the finer ones. An overestimation in the current heights was observed, and they explained that this was due to the fact that the vertical stem (trailing stem) of the sediment plume was not fully contributing to the current during the experiments, whereas the simulation assumed all the particles in the stem would enter the current. With the principle of mass conservation, the simulated current height was expected to be higher, as the horizontal extent of the currents was the same.

Zgheib (2015) examined the motion of a constant volume gravity current released from a non-axisymmetric source. He observed the switch in the major axis when the current was released from a rectangular source, and noticed that the shape of current would not grow as the source geometry. To account for this transformation in geometries, he proposed an Extended Box-Model (EBM) with volume discretization approach to model the motion of homogeneous gravity current in all directions. The EBM could be expressed in the following:

$$U_c = \mathrm{Fr}\sqrt{H_c},\ \mathrm{Fr} = \min(0.5D^{-1/3}, 1.19) \tag{2.54}$$

$$\frac{\partial \sigma h_c}{\partial t} = 0 \tag{2.55}$$

$$\frac{\partial x_f}{\partial t} = u_c \frac{\partial y_f / \partial s}{\sqrt{\left(\partial x_f / \partial s\right)^2 + \left(\partial y_f / \partial s\right)^2}} \tag{2.56}$$

$$\frac{\partial y_f}{\partial t} = u_c \frac{-\partial x_f / \partial s}{\sqrt{\left(\partial x_f / \partial s\right)^2 + \left(\partial y_f / \partial s\right)^2}} \tag{2.57}$$

$$\frac{\partial \sigma}{\partial t} = u_c \tag{2.58}$$

where U_c (= $u_c/(g_o'h_o)^{1/2}$) and H_c (= h_c/h_o) are the normalized velocity and height at the current front, x_f and y_f represent the location of the current front in the x-y plane, σ is the arc length of the advancing front (i.e. perimeter of the current), and s is an independent variable representing the distance measured along the circumference of the front. The Box-Model was illustrated as Equations (2.54) and (2.55), which represent the Fr conditions that conservation of mass, respectively. Equations (2.56) to (2.58) represent the kinematic relation of the discretized sub-volume, with each modeled as an individual Box-Model. The schematic diagram for the definitions of

s and σ, and the volume discretization method are illustrated in Figures 2.7 – 2.8 of Zgheib (2015).

2.5 Summary

Through the literature review on the topics of miscible and sediment thermals, sediment clumps, sediment plumes and gravity currents, several main research areas that are essential for further exploration are identified and summarized briefly as below.

- The investigation of open water sediment disposal and the establishment of engineering models generally assumed the sediment clouds are experiencing thermal regimes upon released from the source. The initial acceleration regime is often overlooked, as the length of this regime is too short to be recorded during the laboratory experiments, and the inclusion of data does not affect the conclusions. This assumption is appropriate only if two conditions are fulfilled: the sediment is instantaneously released and $Nc > 3.2 \times 10^{-2}$. In real open water disposal operations, these conditions are usually not met due to the given shallow water depth and large release volume especially during barge disposal. Hence, to better study the behavior of disposed sediments and develop a model for the purpose of engineering assessment, realistic physical conditions need to be considered.
- Sediment disposal from barges have been investigated through numerical and experimental studies. However, the geometrical factors of the barge (barge length, bottom opening width, aspect ratio, etc.) are not taken into account, despite the fact that the dimensions are often comparable to the water depth at disposal site. Therefore, there is practical interest to examine the effect of barge geometry and include this in the proposed model.
- The gravity currents have been modeled with a Box-Model under condition of either constant volume or constant flux release. In barged sediment disposal operations, the gravity currents are expected to experience a transition from constant flux to constant volume. Therefore, it is necessary to include this transition into the existing Box-Model, to better predict the

spreading of gravity currents due to barge disposal and the subsequent sediment deposition.

- The investigation on sediment clouds has mainly focused on uniform sediment size, while actual disposal operations usually involve sediments with mixed sizes. Therefore, it is useful to examine the formation processes of sediment clouds with mixed sediment sizes.

The issues listed above that are currently unresolved and motivate the present research work. Detailed research methodologies, results and findings are elaborated in the following respective chapters.

Chapter 3

Experimental Methodologies

In this chapter, the experimental facilities and data extraction procedures are described. The present study utilizes two types of measurement techniques: (i) flow visualization to measure the dynamic gross characteristics of the disposed sediments (both sediment cloud and gravity current), and (ii) light attenuation method (LAM) to acquire the sediment deposition thickness. The common facilities and accessories involved in the present study are first introduced in Section 3.1. The procedures of measurement and the subsequent analysis are described in Section 3.2, followed by the definition of gross characteristics in Section 3.3. The detailed experimental conditions and selection criteria of certain parameters are given separately in individual chapters.

3.1 Experimental Setups and Facilities

The general experimental setups and facilities are described in this section, with their connections illustrated in Figure 3.1. A certain amount of sediment was initially filled into a release mechanism and placed above, at or slightly below the water surface. The images of sediments underwater were illuminated by a spotlight and captured by video cameras. In order to convert the pixel values into real dimensions, a scale factor was taken by placing a meter ruler vertically at the center of the release mechanisms before each batch of experiments. On the other hand, for experiments measured with LAM, the sediment deposition profile was backlighted by a light panel and captured by a DSLR (Digital Single-Lens Reflex) camera. In order to convert the attenuated intensities in each pixel into the physical sediment thickness, inverse-calibration was performed with the pre-determined calibration curves.

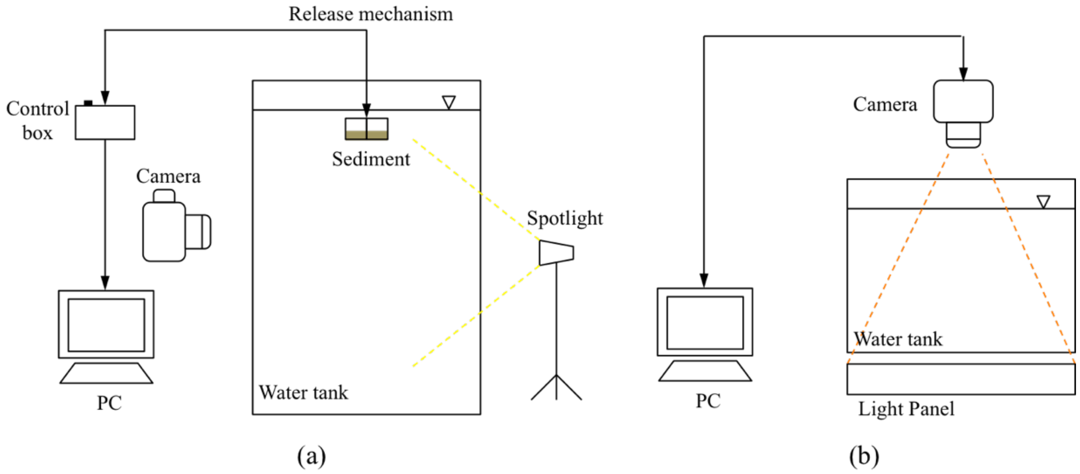

Figure 3.1 General experimental setup; (a) flow visualization, (b) LAM measurement

3.1.1 Water Tanks

Two tanks were employed in the present study, to achieve a wide range of water depths and conditions. Experiments that required deeper water depth were carried out in the Houdini (II) tank, which was located in the CENSAM laboratory of the SMART Center. The study of sediment clouds in the convective descent phase due to barge disposal was performed here. The tank had dimensions of 2.2 m (high) × 2.4 m (long) × 1.2 m (wide). All the sides and bottom of the tank were constructed with glass to facilitate the illumination as well as image acquisition from the sides.

A glass tank in the Hydraulics Modeling Laboratory of the School of Civil and Environmental Engineering, NTU was used to perform the experiments that required shallower water depth. The development of LAM2D (Light Attenuation Method for 2D Data Acquisition), study of composite sediment clouds and bottom collapse of sediment clouds due to barge disposal were performed here. This tank had dimensions of 1.0 m (high) × 2.85 m (long) × 0.85 m (wide). The bottom of the tank was elevated 0.85 m above the floor so that the light panel could be mounted below the tank.

3.1.2 Type of Sediments

To simulate non-cohesive sediments, glass beads manufactured under the trade name Ballotini Impact Beads by Potters industries, Inc. (Malvern, Pennsylvania) were adopted. Various sizes were used to represent non-cohesive sediments ranging from fine to coarse grain sizes in the field conditions. These glass beads had an approximate density (ρ_s) of 2.5 g/cm^3 and ranged in size from 0.045 to 0.850 mm. They were selected for their uniformity and high reflectivity, therefore enhancing the visualization of the disposed sediments. The corresponding properties of the glass beads are listed in Table 3.1 with the settling velocity, w_s is determined from the Dietrich (1982)'s expression. The equations will be introduced in Section 3.3.2.

Table 3.1 Ballotini Impact Glass Beads

Type	Size Range [mm]	d_{50} [mm]	w_s [mm/s]
A	0.600 ~ 0.850	0.725	105.5
B	0.425 ~ 0.600	0.513	71.3
D	0.212 ~ 0.300	0.256	29.3
AE	0.090 ~ 0.150	0.120	9.3
AH	0.045 ~ 0.090	0.068	3.5

Note: w_s is calculated based on the particles settling in water

3.1.3 Release Mechanisms

In real disposal operations, various types of disposal equipment (e.g. pipelines, barges and backhoes) can be employed to release the sediments. In laboratory experiments, various release mechanisms had also been reported to simulate the release of sediments from different equipment. For example, Koh and Chang (1973) injected the materials through a modified syringe into ambient water to mimic the pipelines discharge. Rahimipour and Wilkinson (1992) adopted a spherical clamshell mechanism to simulate the release of sediments from backhoes. Buhler and Papantoniou (2001) released the sand through a funnel with a nozzle to simulate the disposal of sand from barges. The present study applied three types of release mechanisms for various purposes.

3.1.3.1 Bottom-Split Model Barge

This release mechanism is an automated laboratory-scale model split barge with controllable operating parameters to simulate the disposal of barged sediments in a realistic manner. The model barge system consisted of 3 parts with each function differently: (i) a control box equipped with a motor controller (EMP400 Series from Orientalmotor) to control the model barge operating parameters (e.g. opening angular velocity, ω and opening width, W) by using HyperTerminal, a program comes with Windows, (ii) an opening mechanism, using a stepping motor and a set of gears to mechanically open the model barge, and (iii) the model barge itself (Figure 3.2 (b)), which was fabricated using two separated semi-closed rectangular boxes. The model barge was designed from an actual barge scaled down and had dimensions of 20 cm (bin length, L) × 4 cm (bin height, D_b) × 4 cm (bin width, W_b). The scaling analysis will be covered in Section 3.3.

During the experiments, sediments were first loaded in the rectangular boxes from the opening above and uniformly spread throughout the area. The water level inside was maintained to be the same as the ambient water, to minimize the backflow of ambient water into the model barge when opening. Once the experiment was initiated, the two rectangular boxes rotated in opposite directions with angular velocity, ω, specified in HyperTerminal. An opening was formed in the middle through which the sediments were released, resulting in a rectangular release with aspect ratio L/W. In terms of variability, the current setup provided more consistent and reliable control compared with previous manual operations discussed in the literature.

3.1.3.2 Latex Covered Tube Release

This release mechanism consisted of a cylindrical tube with the bottom sealed with a layer of latex sheet, as illustrated in Figure 3.3. The sediments mixtures were initially filled inside the cylindrical tube and placed above the water surface. A motor-driven needle was positioned along the center of the tube with its tip touching the membrane (following the design of Lundgren *et al.* (1992)). By activating the motor, the needle would make a 0.5 cm downward displacement and pierce the latex, resulting in an instantaneous and axisymmetric point release of sediments.

Despite the short releasing time, a higher variation was observed due to the uneven rupture of the latex sheet as compared to the other two release mechanisms (i.e. spring loaded and electrical controlled single-sided trap door) that were discussed in Zhao (2014). Zhao (2014) quantitatively tested the variability of these three release mechanisms with an identical test condition. A faster penetration was observed from the sediments released through the single-sided trap door mechanisms, which might be attributed to the 'knife edge' of the sediment cluster upon impact with the water surface. In order to achieve a higher degree of symmetry compared to the single door release mechanism, the latex covered mechanism was adopted in the study of composite sediment clouds (in Chapter 7).

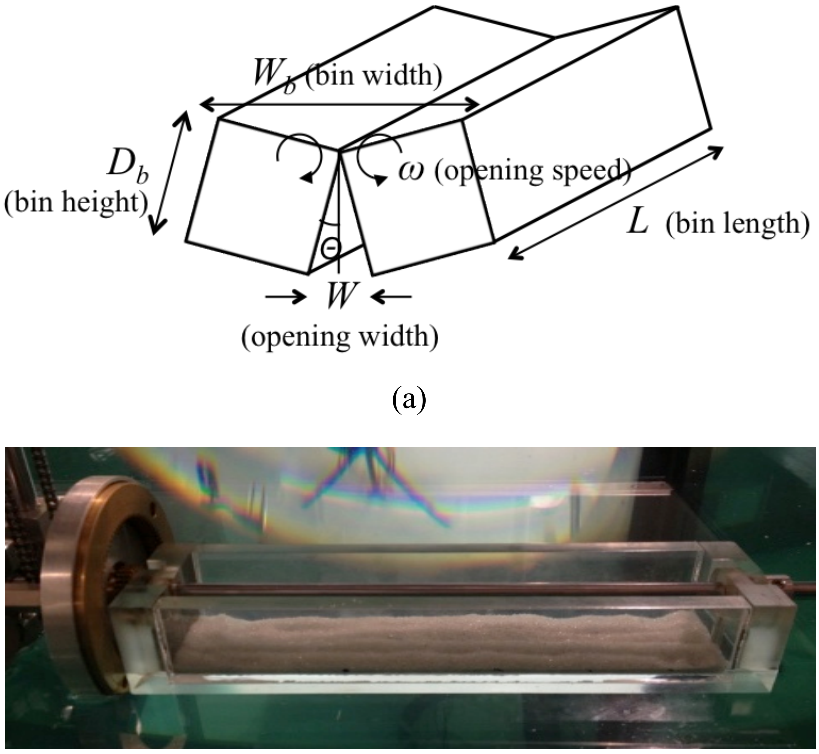

(a)

(b)

Figure 3.2 (a) schematic of model barge (disposal bin); (b) photograph of laboratory scale model spilt barge

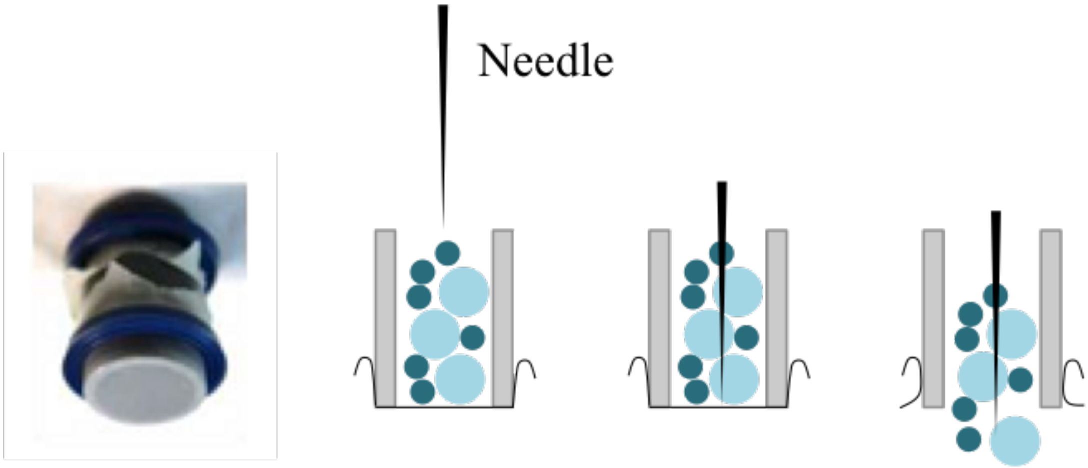

Figure 3.3 Schematic of sediment disposed from latex sealed tube

3.1.3.3 Funnel Release

Two disposal events with identical test conditions (i.e. amount of release and particle size) would experience different development processes when both were released through different release mechanisms. In contrast to the instantaneous release of sediments from the latex covered tube with an opening radius of 0.9 cm, a funnel with smaller opening (opening radius of 0.5 cm) usually formed a continuous release due to the longer release duration. Based on the observation, the sediment cloud from continuous release had lesser variability than the instantaneous release, which might fall into wake-like formation regime.

In the development of LAM2D (in Chapter 5), the proposed calibration technique required the generation of highly consistent deposition profiles, and hence the funnel release mechanism was chosen. Sediments were initially filled inside the funnel with the opening blocked by a stopper, as illustrated in Figure 3.4. Once the experiment was initiated, the stopper was manually removed and the sediments discharged through the opening, resulting in a continuous and axisymmetric point release. Depending on the amount of sediments and the opening size of the funnel, the discharged time could be estimated from the Beverloo equation (Mankoc *et al.* 2007).

Note that the classification of instantaneous and continuous releases followed the diagram introduced in Figure 1.4. In any case, when the amount of sediment is limited, the sediment may be instantaneously release through the funnel and vice versa (i.e. continuous release through the latex-seal tube is possible when the amount of sediment is excessive).

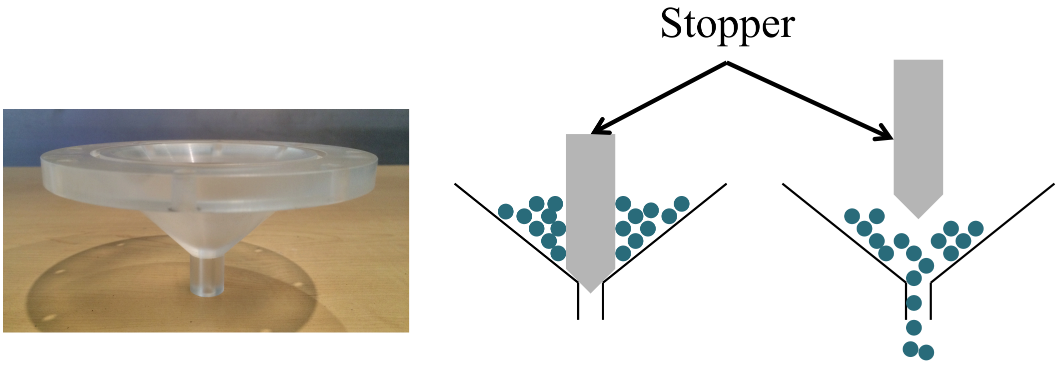

Figure 3.4 Schematic of funnel

3.1.4 Light Panel

A customized light panel was fabricated to develop LAM2D (in Chapter 5) and later adopted to measure the sediment deposition profile due to barge disposal (in Chapter 6). The application of LAM was first reported in Barnett (1991). Instead of using a light panel, he aligned a light bulb with convex lens to generate a parallel light source, shined through the targets (jets and plumes) onto a translucent screen before being recorded by videotape. The densities and concentrations variations were then analyzed from the videos. Following the same principle, Cenedese and Dalziel (1998) used an array of four fluorescent tubes, placed underneath the tank to serve as the light source. This design provided a more stable and uniform light source, which was then widely used in different studies (Leppinen and Dalziel 2001, Munro and Dalziel 2005, Njifenju *et al.* 2013).

Several criteria had to be considered during the design stage of a light panel. The dimensions of the light panel were the most important, and depended on both the measurement domain and the available space beneath the glass tank (2.85 m × 0.85 m as mentioned previously). In the preliminary study, the measurement domain was estimated to be ~1.0 m (long) × 0.5 m (wide). The second criterion was the selection of light source, which depended on the natural of flows or profiles to be measured. High frequency lighting (up to 30 kHz) could be used for measuring dynamic flows to reduce the light flickering issue. However, the current study employed normal lighting (50 Hz for Singapore) as the deposition profiles to be measured were in stagnant condition. After considering several options, fluorescent tubes were finally chosen because the light was emitted in a radial manner as compared to LED light which was directional, and it had less variation with respect to intensity than halogen and OHP lights (Kikkert 2006).

The current light panel was fabricated with fourteen 1.5 m (~5 ft.) long T8 fluorescent tubes, which was arranged equidistant covering a width of 0.85 m in an aluminum rectangular box. In the current setup, the generation of a uniform light sheet over the measurement domain was important. To improve this condition, the box cover was designed with light diffuser material (acrylic diffusion sheet). By increasing the panel depth (= 0.15 m, the distance between tubes and diffusion sheet), the uniformity of the light sheet could be greatly enhanced. In addition, the inner frame of the box was painted with highly reflective paint to promote reflections and improve the uniformity of the light at the edges of the box.

3.1.5 Cameras

3.1.5.1 Video Camera

Two video cameras (model: SONY HDR-XR550E & SONY HDR-CX900E, resolution: 1080 × 1920 pixels, 25 frames per second) were used as the recording tools. The placements of video cameras were different for each study. In Chapters 4 and 6, since the sediments were disposed from a rectangular opening, the descending and spreading motions were different along both longitudinal and transverse directions. Thus, the motions of the disposed sediments were captured from two directions. In the experiments of composite sediment disposal (Chapter 7), sediment clouds were released in an axisymmetric manner. The entrainment and spreading behavior were expected to be the same in all directions. Hence, the experiments were recorded from a single direction. The recorded videos allowed the user to extract the gross characteristics through image analysis by using MATLAB customized programs.

3.1.5.2 DSLR Camera with CMOS Sensor

A Nikon D700 DSLR (Digital Single-Lens Reflex) camera with CMOS and color sensor, equipped with a 24-70 mm *f*/2.8L lens was employed along with the light panel for LAM2D. The selection criteria for camera parameters (i.e. exposure time, *f*-stops, ISO sensitivity) and the specific values used in individual studies will be discussed in the respective chapters. The camera was mounted on top of the water tank, facing vertically downward toward the light panel. The distance between the camera and the measurement domain (sediment profile) was adjusted to achieve a balance between the needs to reduce the barrel distortion (i.e. increase in the distance between camera and target) and to retain a good resolution (i.e. decrease in the distance between camera and target). Finally, it was determined that the optimal distance was for the camera to be placed 1 m apart from the bottom of the tank. Each pixel in the captured images corresponded to an area of 0.34×0.34 mm^2. The captured images were inverse-calibrated with the pre-determined calibration curves to obtain the profile of sediment thickness.

3.2 Measurement and Data Extraction Techniques

In the present study, two types of measurement techniques were performed: (i) flow visualization to determine the dynamic behaviors of the disposed sediments in both convective descent and bottom collapse phase, and (ii) LAM to measure the sediment profiles deposited from gravity currents. The primary data were collected in the format of videos and photos for the above-mentioned techniques, respectively. In this section, the principles of image analysis and inverse calibration are introduced, followed by defining the gross characteristics that were employed in the present study.

3.2.1 Image Analysis

The extraction of information from recorded videos was achieved through image analysis using customized MATLAB programs. The data were extracted with an integrated approach, which was introduced by Burridge and Hunt (2012) to study and present the transient development of irregular turbulent fountains in a continuous manner. In the post-processing, each image frame recorded by the video cameras first had a constant background subtracted, and then was converted into gray scale image (i.e. an image in which every pixel has a value between 0 (black) and 255 (white)). Figure 3.5 illustrates a time series of images of a sediment cloud after release from the model barge. To access the vertical motion, the gray scale value on each pixel was summed up horizontally to produce a column vector at each time frame and then combined in time series to yield a horizontally integrated image (i.e. the panel in the upper left of Figure 3.5). To trace the horizontally spreading, the same integration was performed vertically (i.e. the panel in the lower right of Figure 3.5). The integrated images provided a quasi-steady representation of the transient flow phenomenon, and qualitatively described the spatial and temporal distributions of particles. The frontal position and cloud size were determined from the horizontal and vertical integrated images respectively.

Note that, in the study presented in Chapter 6, the extraction process was rather straightforward because the gravity currents had less variation than the descending clouds. After the image had the background subtracted and converted to gray scale image (Figure 3.6 (a)), the edge of the currents was determined and filled with white blob (Figure 3.6 (b)). The current fronts were then retrieved based on the maximum horizontal extent of the white blob (green dots). To determine the current height, the gravity currents had to be identified (yellow boxes), to distinguish them from the sediment plume that was releasing from the barge. Within the yellow boxes, the current heights were the highest locations of the white blob in both directions and were marked as red dots.

3.2.2 Inverse Calibration for LAM

Quantitative information of the sediment deposition profile was acquired through the light attenuation method (LAM). The principle of LAM involves the attenuation of light intensity transmitted through the sediment layer, and the sediment thickness is then determined based on the attenuated intensity. In this case, the two most important parameters are the reference (I_{ref}) and attenuated (I) intensities, which represent the intensities received by the camera without and with the presence of the sediment layer, respectively (Figure 3.7). Upon transmitting through the sediment layer, the incident light is absorbed and reflected/refracted. The transmission ratio can be calculated as the ratio of attenuated intensity to the incident intensity. Nine ratios between 0 and 1 can be identified to account for the absorption (i.e. C_a, C_w, C_g, C_p) and reflection/refraction losses (i.e. $C_{a\text{-}g}$, $C_{g\text{-}w}$, $C_{w\text{-}a}$, $C_{g\text{-}p}$, $C_{p\text{-}w}$). The subscripts a, g, w and p represent the media of air, glass, water and particles, respectively. The interfaces between the media are noted with hyphen (-). Thus, I_{ref} can be expressed in the following equation (Kikkert 2006):

$$I_{ref} = C_a \times C_w \times C_g \times C_{a\text{-}g} \times C_{g\text{-}w} \times C_{w\text{-}a} \times I_{source} \tag{3.1}$$

where I_{source} is the source intensity, while I can be represented as

$$I = C_a \times C_w \times C_g \times C_{a\text{-}g} \times C_{g\text{-}w} \times C_{w\text{-}a} \times C_p \times C_{g\text{-}p} \times C_{p\text{-}w} \times I_{source} \tag{3.2}$$

Hence,

$$I/I_{ref} = C_p \times C_{g\text{-}p} \times C_{p\text{-}w} \tag{3.3}$$

Thus, the ratio of attenuated to reference intensity is dependent on the characteristics of the particles (i.e. h_s and d_{50}, where h_s is the sediment thickness and d_{50} is the particle size). Equation (3.3) can be formulated as

$$I/I_{ref} = f_1\,(h_s, d_{50}) \tag{3.4}$$

with each particle size having its own unique calibration curve.

From the captured images, I of each pixel represented the averaged attenuated intensity in an area of size 0.34 × 0.34 mm^2, which also implied that any changes in sediment thickness within this area were not identified. However, this error is less than the variation (standard error) due to the inverse-calibration, and will be discussed in Chapter 5. Equation (3.4) can be reformulated as Equation (3.5) for the inverse-calibration:

$$h_s = f_2\,(I/I_{ref})\,d_{50} \tag{3.5}$$

In Chapter 5, different calibration curves are determined for different range of h_s/d_{50} and will be discussed in detail in the subsequent chapter.

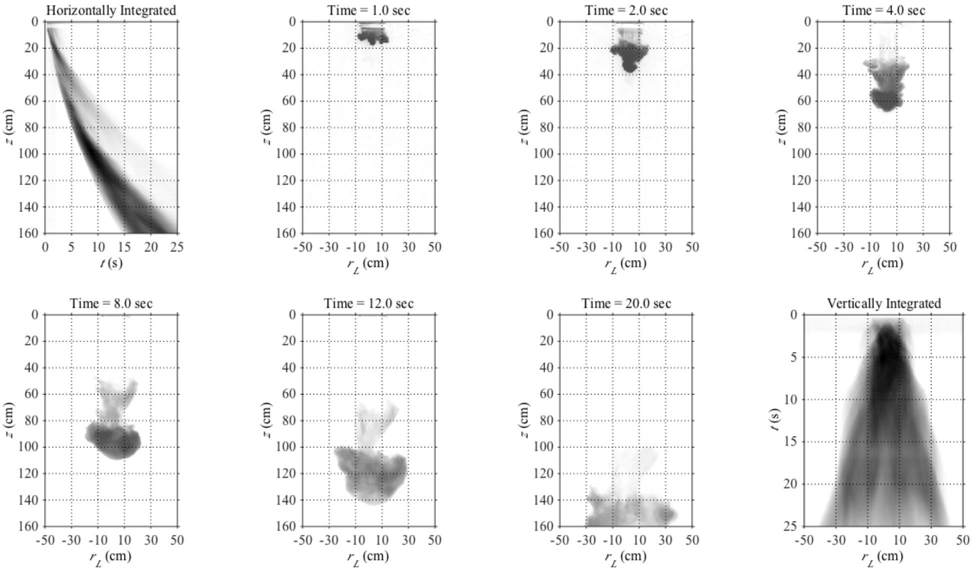

Figure 3.5 Horizontal and vertical integrated images

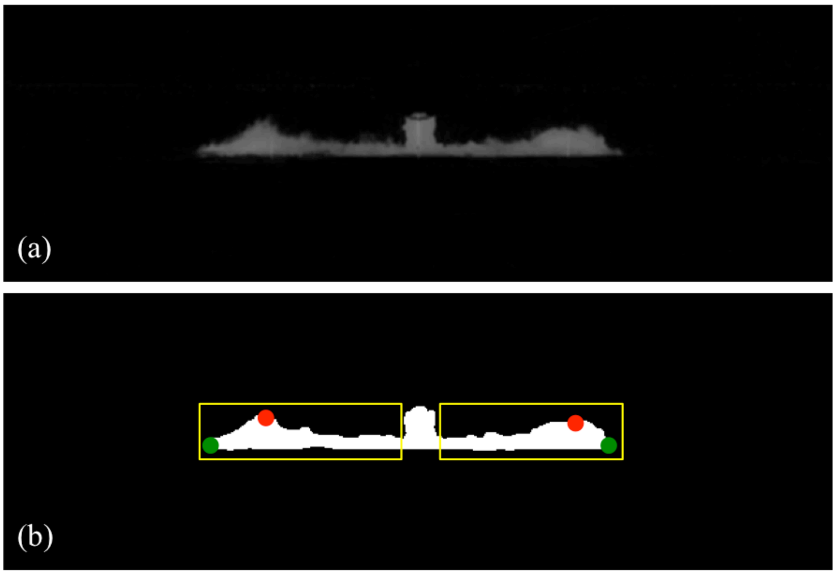

Figure 3.6 Gray scale image of gravity current and the subsequent processing

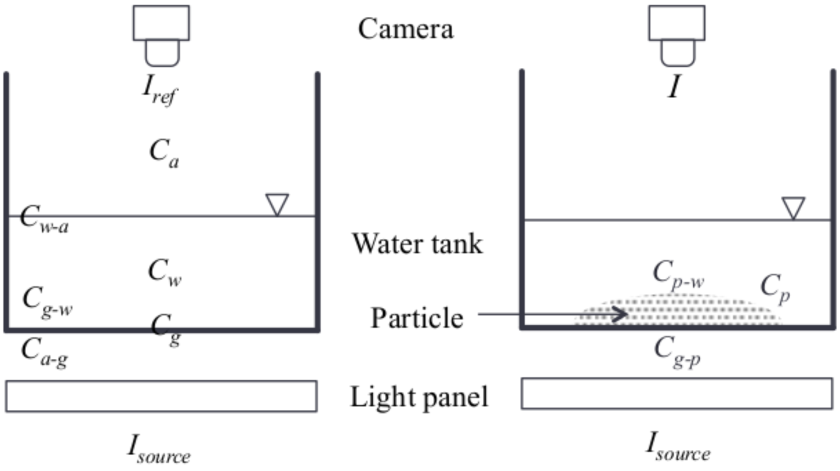

Figure 3.7 Schematic diagram of the principle of LAM

3.2.3 Definition of Gross Characteristics

The disposed sediments may descend as plumes, thermals or clumps depending on the source and release conditions. In general, these are called sediment clouds. For sediment clouds in the water column, the lateral cloud radius and penetration depth are the most common parameters to represent the growth and descent process. After impact with the seabed, the sediment clouds continue to propagate laterally as gravity currents. For gravity currents, the current front and current height are the most common parameters to describe the motion and spreading behavior. As the gravity currents propagate downstream, the suspended sediments may settle out and deposit on the seabed. The thickness of sediment can be applied to quantitatively represent the sediment deposition profile. In the subsequent sub-sections, the definition of these parameters are defined in detail and illustrated with schematic diagrams.

3.2.3.1 Cloud Radius

The definition of cloud radius adopted in the current study is the maximum cloud width, which could be obtained from half of the maximum horizontal extent of the cloud, and was most commonly used in previous experimental studies (Buhler and Papantoniou 1991, Noh and Fernando 1993, Wen and Nacamuli 1996, Li 1997, Bush *et al.* 2003, Zhao *et al.* 2014). In the vertically integrated image, the value of cloud radius was extracted from the distance between the first and last non-zero pixels.

In the present study, two types of cloud radius, transverse radius, r_T and longitudinal radius, r_L were recorded. They represent the radius of sediment cloud recorded in the transverse/longitudinal direction, respectively. The schematic diagram in Figure 3.8 shows the physical lengths of r_T and r_L. In the previous studies of two-dimensional starting plumes and thermals, the reported radius was usually r_T based on the current definition. For simplicity, a cloud radius is also referred to as 'transverse radius, r_T' in this report.

3.2.3.2 Cloud Frontal Position

Regarding the analysis of the vertical position of the sediment cloud, previous studies in stagnant ambient commonly determined the front position of the cloud and calculated the descent velocity based on time derivative ($u_f = \mathrm{d}z_f/\mathrm{d}t$) (Buhler and Papantoniou 1991, Noh and Fernando 1993, Wen and Nacamuli 1996, Li 1997, Bush *et al.* 2003, Zhao *et al.* 2014). This was probably due to the ease of distinguishing the extreme point in the horizontally integrated image. The frontal position, z_f, of the sediment cloud adopted in the present study is shown in Figure 3.8.

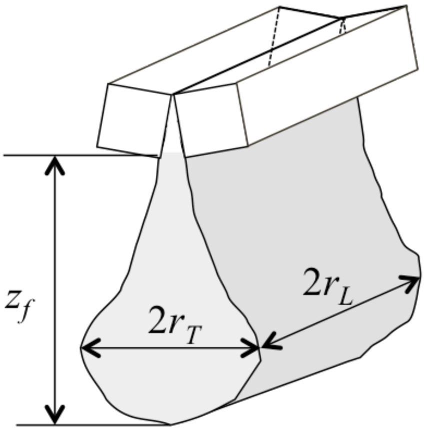

Figure 3.8 Definition of transverse radius, r_T; longitudinal radius, r_L and frontal position, z_f

3.2.3.3 Current Front and Current Height

After impact with the bottom, the sediment cloud continued to spread horizontally in the form of a gravity current, as illustrated in Figure 3.9. Under the conditions of stagnant ambient and the absence of a vertical wall, two gravity currents were generally formed, propagated in opposite direction and away from the source (Linden and Simpson 1990, Hogg *et al.* 2005, Nguyen *et al.* 2012). Here, the current front, x_c is defined as half of the maximum horizontal extent as shown in Figure 3.9, and was most commonly used in the previous studies. The definition of current height, h_c adopted in the present study is the maximum height of the current excluding the area of the sediment plume (dashed rectangular box in Figure 3.9).

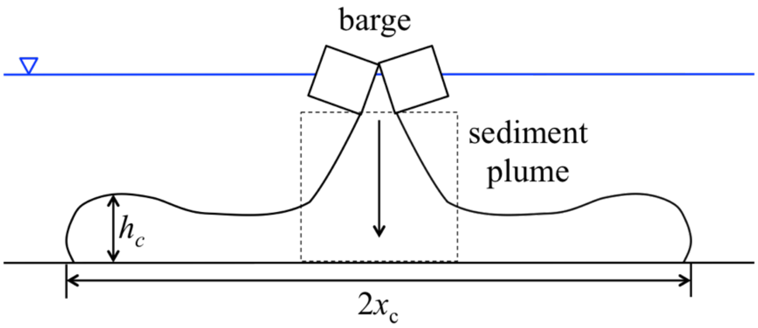

Figure 3.9 Definition of current front, x_c and current height, h_c

3.2.3.4 Deposition Thickness

Previous studies defined several parameters, such as deposition depth, deposition thickness, layer thickness, and mass or volume per unit area, to quantitatively describe a profile generated from the deposition of sediments (Johnson *et al.* 1988, Dong *et al.* 2007, Yoshida *et al.* 2012). Although the naming is different, these parameters are physically the same, defined by the vertical height of a sediment layer at specific location or coordinate (x, y). In the present study, deposition thickness, h_s is employed as illustrated in Figure 3.10.

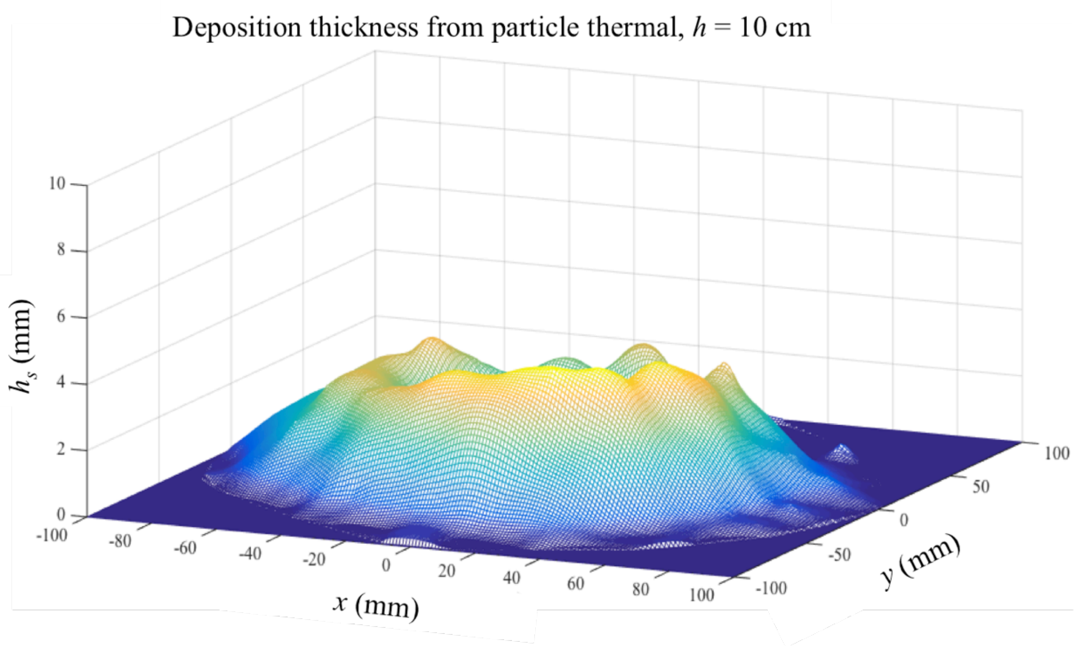

Figure 3.10 Definition of deposition thickness, h_s

3.3 Scaling Analysis

The correlation between laboratory and field scales was performed through two types of scaling similarly to previous studies (Gensheimer *et al.* 2012, Zhao 2014). The bulk characteristics were scaled through volumetric scaling, and the size of individual particles was scaled through cloud number scaling.

3.3.1 Volumetric Scaling

It is assumed that the motion of sediment clouds is dominated by their total buoyancy rather than the property of individual particles. Therefore, the laboratory dimensions from the present study can be linked to the field conditions through scaling analysis. The scaling between laboratory and field conditions involved the length scale (L) derived from volumetric scaling (Equation (3.6)), and the velocity (U) and time (T) scales can be established based on Froude scaling (White 1999), as derived in Equation (3.7).

$$L_F = L_E \left(\frac{V_F}{V_E} \right)^{1/3} \tag{3.6}$$

$$\begin{gathered} Fr_F = Fr_E \\ \frac{U_F}{\sqrt{gL_F}} = \frac{U_E}{\sqrt{gL_E}} \\ U_F = U_E \sqrt{\frac{L_F}{L_E}} \;\&\; T_F = T_E \sqrt{\frac{L_F}{L_E}} \end{gathered} \tag{3.7}$$

where the subscript "*F*" and "*E*" denote the field and laboratory (experiment) scales. This type of scaling was performed to scale the bulk characteristics. For example, using the typical volume of a barge for sediment disposal (V_F = 1000 m^3) and the volume of glass bead chosen in a single release in the laboratory (V_E = 80 cm^3), a length ratio of $L_F/L_E \approx 232$ was derived. The length, velocity and time scales from the volumetric scale should also be applied to scale the water depth and barge opening speed.

3.3.2 Cloud Number Scaling

The scaling of particle size was achieved by conserving the ratio between the individual particle settling velocity to the characteristics cloud descent velocity through a cloud number, *Nc* (Rahimipour and Wilkinson 1992):

$$Nc = \frac{w_s r_o}{\left(B_o\right)^{1/2}} \tag{3.8}$$

where r_o is the initial equivalent cloud radius and B_o is the total buoyancy excess. Thus, given the laboratory properties (like particle size and total release volume) and the field release volume, the settling velocity of the corresponding sediments in the field can be calculated. The conversion between settling velocity and particle size was achieved through the empirical relationship developed by Dietrich (1982) for spherical particles:

$$\begin{aligned}\log_{10} w_* = -3.76715 + 1.92944 \log_{10} D_* - 0.09815\left(\log_{10} D_*\right)^2 - \\ 0.00557\left(\log_{10} D_*\right)^3 + 0.00056\left(\log_{10} D_*\right)^4\end{aligned} \tag{3.9}$$

where

$$w_* = \frac{w_s^{\,3}}{\left(\rho_p/\rho_a - 1\right) g v} \tag{3.10}$$

$$D_* = \frac{\left(\rho_p/\rho_a - 1\right) g d_p^{\,3}}{v^2} \tag{3.11}$$

where v is the kinematic viscosity of ambient fluid. The above expression is applicable for particle size ranging from 0.01 mm to 100 mm. The back calculation of particle sizes from a known settling velocity was done iteratively through MATLAB.

Wang *et al.* (2015) tested the cloud number scaling discussed above through two-phase computational fluid dynamics (CFD) modeling for a wide parametric range. They simulated the sediment clouds with various initial masses (ranging from 3 g to 12 kg) and particle diameter (ranging from 0.51 mm to 2.20 mm). By comparing the development of the bulk characteristics of both the solid and fluid phases, the cloud number scaling was found to be appropriate for sediment clouds.

Chapter 4

Barged Sediment Disposal Model

4.1 Introduction

Various activities, such as land reclamation and management of dredged materials, often involve the open water disposal of sediments. The volume of sediments involved can be very substantial, for example Bever *et al.* (2014) reported that ~2.3 mil m^3 of sediments are dredged annually from San Francisco Bay. To carry out these open water disposal operations typically require the pre-approval from regulatory agencies, and the approval requirements include the evaluation of water quality impact in the water column (USEPA/USACE 1991, USEPA/USACE 1998, EPA 2004). Hence, it is essential to be able to assess the fate and transport of the disposed sediments in the coastal environment with sufficient accuracy for the purpose of impact assessment.

The present study focuses on the open water disposal of sediments with bottom-split barges, which are commonly deployed in real operations (Eisma 2006) due to their large carrying capacity, with up to ~1000 m^3 of sediment volume that can be transported at a time (Miyamoto *et al.* 1993). The sediments are released to the underlying water column through the bottom opening of the barge beneath the water surface. The transport processes of the disposed sediments are categorized into near and far field regions, distinguished by the mechanisms that govern the mixing and dynamics of the sediment cloud.

Note: The material presented in this chapter has been published in the Journal of Waterway, Port, Coastal, and Ocean Engineering, doi: 10.1061/(ASCE)WW.1943-5460.0000341

For the near field region, the field evaluation by Bokuniewicz *et al.* (1978) showed that the dynamic behavior of the disposed sediments in the water column generally experiences three sequential phases: (i) convective descent phase, during which the flow behavior is dominated by the source conditions and gravity (i.e. buoyant convective flow); (ii) dynamic collapse phase upon impact with the seabed, during which the horizontal spreading occurs; and (iii) passive-transport dispersion phase (or intermediate and far field), when the sediments are carried by the ambient currents and turbulence. Furthermore, in the convective descent phase, the development of a sediment cloud is generally classified into the classical three regimes: acceleration, thermal (self-preserving) and dispersive regime as suggested by Rahimipour and Wilkinson (1992), also referred to P1 process (in Figure 1.4) in the present study. It is noted, however, that the distinction of the three regimes by Rahimipour and Wilkinson is based on the assumption of an instantaneous release, which may not be valid when the sediment volume is large such as barged releases.

In the literature, there were two main studies performed to examine the near field transport of the disposed sediment from the open water barge disposal. Koh and Chang (1973) developed a mathematical model (referred as K&C model) based on the self-preserving miscible thermal to analyze the motion of the sediment cloud. The assumptions of point source and instantaneous release were adopted in their model for simplicity. Subsequently, Johnson and Fong (1995) established a numerical model, STFATE (short-term fate) to compute the water column concentration and bottom disposition due to barged releases. The basic formulation of STFATE follows Koh and Chang (1973), with the barged volume being discretized into a sequence of three-dimensional releases with varying insertion speed. STFATE has been widely used for engineering analysis in the industry (Howlett 2003, Bailey *et al.* 2004). However, we note that the point source axisymmetric assumption by STFATE enables an efficient analysis but does not actually represent the actual physical conditions in a realistic manner. Upon release from the barge, the sediment cloud should first descend as a two-dimensional (2D) sediment curtain before transiting to an axisymmetric three-dimensional (3D) bowl shape sediment cloud. The flow regime transitions should also be closely related to the barge's geometry. Furthermore, with the large amount of sediments involved in the barge disposal, the duration for the sediments to be fully discharged and the duration for the sediments to descend through the water column may be of the same order of magnitudes. Therefore, the sediment cloud may behave as a continuous release in the beginning, as described in the P3 process of Figure 1.4, rather than as an instantaneous point source approximated by the K&C and STFATE models. In summary, the existing models have oversimplified the complexity of the sediment cloud behavior in the barge disposal operations.

Apart from these two models and the other engineering models that summarized in Figure 1.3, there were also numerical studies that investigated the particle clouds dynamics within the convective descent phase using computational fluid dynamics, CFD (Harada *et al.* 2013, Lai *et al.* 2013, Wang *et al.* 2014). The numerical results revealed comprehensive flow features of both the solid particle and entrained fluid phases, which were difficult to measure through experiments. However, the advanced numerical approaches require substantial computational resources, which are too demanding for engineering applications at the moment.

As mentioned earlier, the disposed sediment would eventually enter the far field region, when the transport of the sediments is primarily driven by the ambient currents. A far field model can then be applied to predict the fate of suspended sediments and long-term bathymetry changes in the disposal sites. An example is the Surface-water Modeling System (SMS), which uses the particle tracking methods (Lackey and MacDonald 2007). These far field models generally cover a large area beyond the disposal and dredging locations for impact assessment, and require the input from near field models (e.g. STFATE) to provide the boundary conditions around the disposal location for their simulations.

The objective of this study is to develop a new model that can improve the representation of the physical conditions of barged sediments disposal in the convective descent phase (near field region). The P3 process, which is mostly expected in many real operations, is further distinguished into six different regimes. An experimental investigation was performed in the present study to validate the model. The simulation of a field disposal operation was also presented as an application example. In the following, the development of the new model is first presented. The model predictions are then compared to the experimental results for assessment.

4.2 Model Description

The new barged sediment disposal model (called BSDM) is based on a classification scheme of the sediment cloud behavior with six different flow regimes (four asymptotic cases plus two cases pertaining to the dispersive regime). The gross characteristics of each regime are computed from the respective asymptotic solutions. The classification scheme is introduced in the following sub-sections, together with computation of the gross characteristics in the flow regimes.

4.2.1 Flow Regime Classification

The classification scheme classifies the flow regimes of the sediment cloud based on the comparisons of the physical length parameters that represent the dynamic influences on the cloud behavior. The approach bears similarity to the one adopted by the popular software CORMIX for buoyant jets assessment. The scheme includes three dominant physical length parameters: the empty depth, z_e, transition depth, z_t and dispersive depth, z_d. Besides the three length parameters, the parameter, h is used to indicate the vertical location in the water column where the characteristics of the sediment cloud are assessed (the value can be defined by the users). Their definitions and illustrations are given in Table 4.1 and Figure 4.1, respectively. z_{a-t} is the length of acceleration regime and the examination of $z_{a-t} > z_e$ is discussed in Appendix A.

Figure 4.2 shows a schematic diagram of the classification scheme (tree chart with $z_{a-t} < z_e$). At the final stage of the classification, the flow regimes with the respective pictorial descriptions are presented. In the pictures, the boxes at the top represent the barge or disposal bin. The fluid entrained by the sediments is shaded in grey, and the dots denote the sediment particles. In the classification, the first step is to compare z_e with h. If the barged sediments are fully discharged before the sediment cloud front reaches h (i.e. $z_e < h$), the sediment cloud at that location will behave like an instantaneous thermal. Otherwise, the sediment cloud will behave like a continuous plume.

Towards the end of the thermal regime, the descent velocity of the sediment cloud decreases, approaching the particle settling velocity, w_s (Zhao *et al.* 2012). Hence, the settling motion of the particles would surpass the internal circulation of the thermal, and the particles would then separate from the entrained fluid. The depth where the sediment separates from the entrained fluid is defined as the dispersive depth, z_d (Rahimipour and Wilkinson 1992). In the classification scheme, when z_d is smaller than h, the sediment cloud will enter the dispersive phase at z_d.

For barges with a narrow bottom opening (i.e. large L/W ratios, where L is the disposal bin length and W the opening width), the sediment plume/thermal should be predominantly two-dimensional (2D) before transiting to three-dimensional (3D) with anisotropic entrainment. The difference between 2D and 3D flow regimes is also shown in Figure 4.2. In the 2D flow regimes (C1, C3 and C5), the sediment cloud behaves as if it is released from a line source, and the spreading occurs mainly in the transverse direction. However, in the 3D flow regimes (C2, C4 and C6), the spreading occurs axisymmetrically, and the sediment cloud behaves as if it is released from a round or point source. The 2D flow regimes transit to 3D flow regimes at z_t.

In the following, the dimensional analysis for z_e and z_t will be presented. The independent variables include the disposed sediment volume, V_o, median particle diameter, d_{50}, sediment density, ρ_s, ambient density, ρ_a and dimensions of the disposal bin bottom opening (L and W). Subsequently, the quantitative equations for z_d proposed by previous studies will also be presented.

4.2.1.1 Empty Depth, z_e

As described in Table 4.1, the empty depth, z_e, is defined as the penetration depth of the sediment cloud front at the instance when all the sediments have been completely released (or emptied) from the barge. The formulation of z_e requires two steps: the first step occurs at the source (barge or disposal bin) and the second step involves the descending motion of the discharged sediment cloud.

The duration for the sediments to be fully-emptied from the barge, t_e, is considered first. The formulation of t_e is based on the idea that upon opening of the barge doors, a convective vertical exchange occurs between the underlying water and barged sediments through the bottom opening (L and W) of the disposal bin, being driven by the potential energy due to the depth of the sediments inside the bin D_o (= $V_o/(LW_b)$ where W_b is the disposal bin width). The other variables that can influence t_e are the reduced gravitational acceleration, g' (= $g (\rho_s-\rho_a)/\rho_a$, where ρ_s is the sediment density and ρ_a the ambient density), d_{50} of the sediment particles, and the kinematic viscosity, v of the ambient fluid. Hence,

$$t_e = f(L, W, V_o, g', d_{50}, v) \tag{4.1}$$

Here, V_o is used instead of D_o, because it represents the physical meaning of t_e better. Next, using dimensional analysis, we can obtain the following functional form:

$$t_e\sqrt{\frac{g'}{V_o^{1/3}}} = f_2\left(\frac{LW}{V_o^{2/3}}, \frac{L}{V_o^{1/3}}, \frac{W}{d_{50}}, D^*\right) \tag{4.2}$$

where $D^* = d_{50}g'^{1/3}/v^{2/3}$ is the dimensionless particles diameter (Aguirre-Pe *et al.* 2003). The π-term, W/d_{50} (= R_{barge}), is equivalent to the dimensionless radius, R (= D/d_{50}, D is the opening diameter of the orifice) adopted in previous studies of particles discharge from an orifice (Mankoc *et al.* 2007, Janda *et al.* 2008). In particular, Mankoc *et al.* (2007) investigated the discharges of particles from 3D round and 2D line orifices through experimental and numerical studies. They found that in Beverloo's law, there is no dependence on the d_{50} when $D >> d_{50}$, which would also be applicable to our situation. We shall also show later that the independency was also observed in the experimental data. Thus, Equation (4.2) can then be reduced to:

$$t_e\sqrt{\frac{g'}{V_o^{1/3}}} = f_3\left(\frac{LW}{V_o^{2/3}}, \frac{L}{V_o^{1/3}}, D^*\right) \tag{4.3}$$

Furthermore, assuming that the effect of the aspect ratio of the bottom opening is not significant in determining the empty time as compared to the opening area, Equation (4.3) can then be simplified further as:

$$t_e\sqrt{\frac{g'}{V_o^{1/3}}} = f_4\left(\frac{LW}{V_o^{2/3}}, D^*\right) \tag{4.4}$$

In the second step, the descending motion of the sediment cloud is governed by the bulk characteristics of the buoyancy of the barged release, i.e. V_o and g' together with t_e. Hence, with dimensional analysis, z_e can be expressed in the following form:

$$\frac{z_e}{V_o^{1/3}} = f_5\left(t_e\sqrt{\frac{g'}{V_o^{1/3}}}\right) \tag{4.5}$$

Table 4.1 Physical length parameters for barged sediment disposal

Physical length parameter	Description
Empty depth, z_e	The distance at which the transition from plumes (continuous) to thermals (instantaneous) takes place
Transition depth, z_t	The distance at which the sediment cloud transits from two-dimensional into three-dimensional (3D) flow regimes
Dispersive depth, z_d	The distance at which the solid sediment particles leave the entrained fluid and settle at their respective settling velocities
Water depth, h	Water depth or depth of interest within the water column

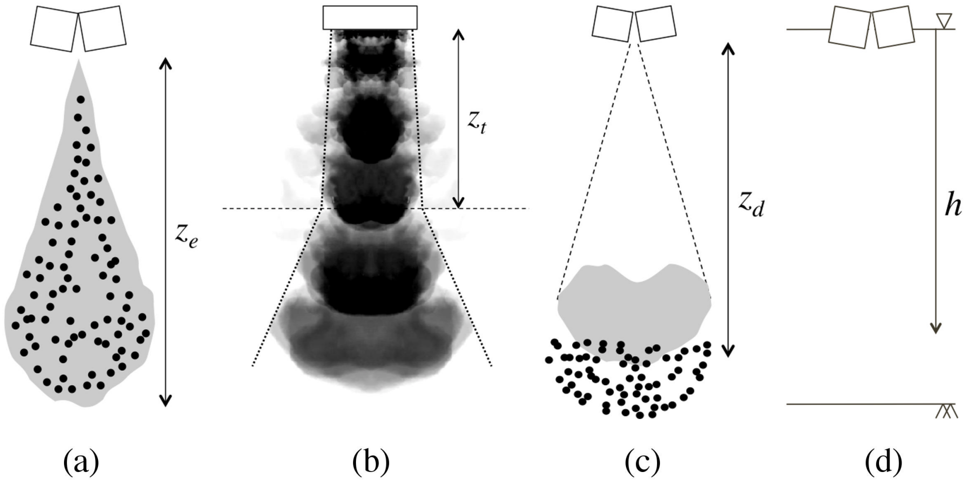

Figure 4.1 Illustration for physical length parameters, (a) empty depth, z_e, (b) transition depth, z_t, (c) dispersive depth, z_d and (d) depth of interest, h

4.2.1.2 Transition Depth, z_t

Also described in Table 4.1, the transition depth, z_t is determined from the penetration depth of sediment cloud when the longitudinal spreading rate ($\alpha_L = \mathrm{d}r_L/\mathrm{d}z$) is equal to the transverse spreading rate ($\alpha_T = \mathrm{d}r_T/\mathrm{d}z$). In other words, z_t represents the location whereby the spreading becomes axisymmetric. Clearly, z_t is affected by the geometrical characteristics of the bottom opening, L and W. In addition, from the literature, the spreading rates of the starting plume and thermal regimes before z_t have been found to be distinctly different (Ching *et al.* 1993, Lee and Chu 2003). Hence, z_t would also be affected by the duration of the release, t_e. Thus, we have

$$z_t = f_6\,(t_e, L, W, g') \tag{4.6}$$

Using dimensional analysis again,

$$\frac{z_t}{L} = f_7\left(\frac{t_e\sqrt{g'}}{\sqrt{L}}, \frac{L}{W}\right) \tag{4.7}$$

The function f_7 has to fulfil two conditions: (i) when $L/W = 1$ (i.e. when the sediments are being released from a square or round (point) source), z_t should be equal to zero and the sediment cloud enters the 3D regimes directly, and (ii) when L/W increases, z_t should also increase.

From Equations (4.4), (4.5) and (4.7), the length parameters are dependent on W (both LW and L/W with fixed L) and d_{50} (D^*). We thus designed the experimental study by disposing various sizes of sediment from different opening widths. The experimental results were used to calibrate Equations (4.4), (4.5) and (4.7), which would be discussed in Section 4.3.2.2, as well as validate the model.

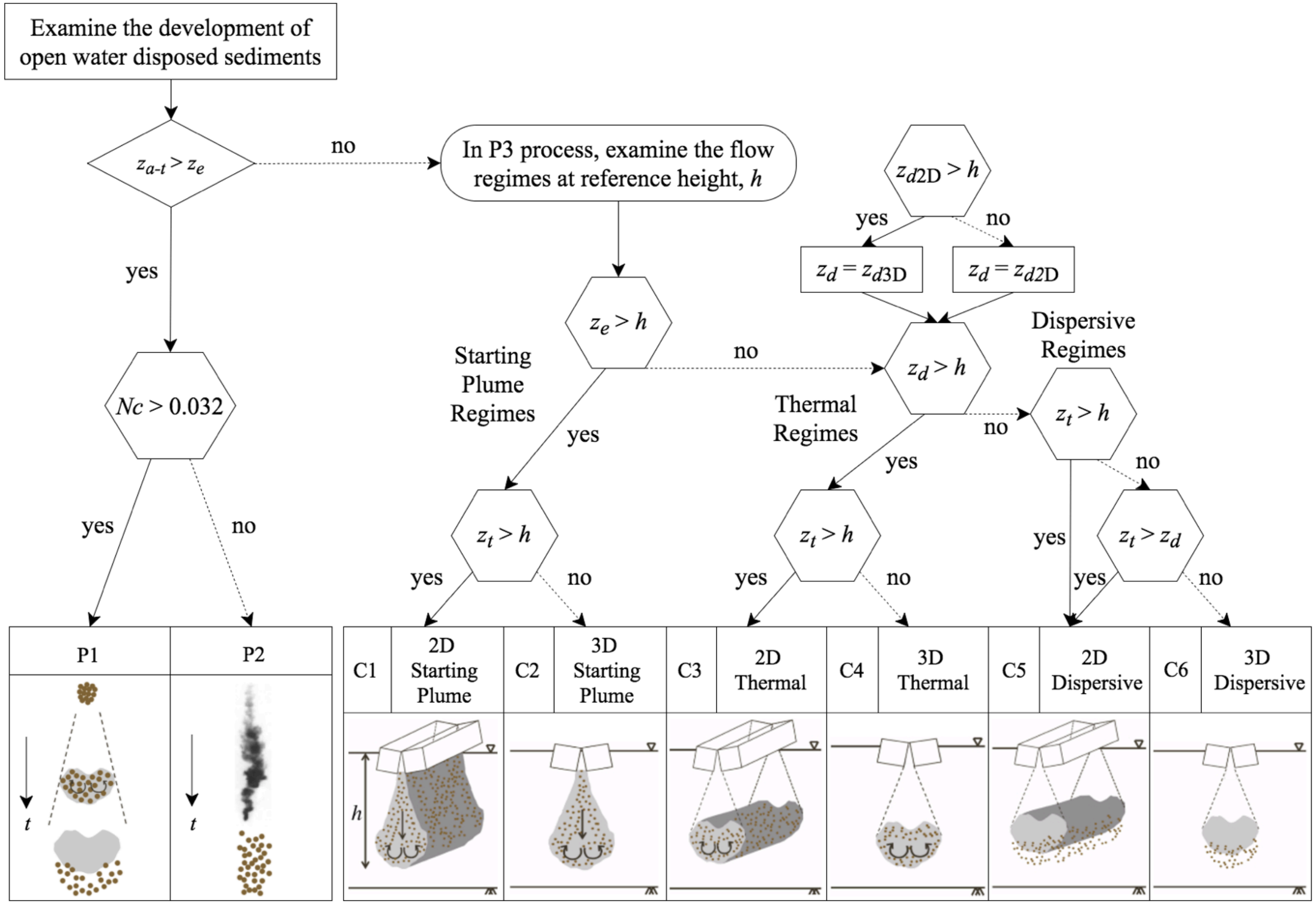

Figure 4.2 Flow regime classification for the open water disposal of sediments from a bottom-split barge

4.2.1.3 Dispersive Depth, z_d

The value of z_d is determined based on empirical functions proposed by previous studies. Noh and Fernando (1993) examined the dispersive depth of a two-dimensional sediment thermal by releasing a mixture of glass beads and fluorescent dye. They observed the separation of sediments from the entrained fluid after the sediment mixture travelled some distance away from the source, and defined this distance as the 2D dispersive depth, $z_{d2\mathrm{D}}$. They then developed a proportional relationship with the source total buoyancy per unit length, b_o (= $g'V_o/L$) as

$$\frac{z_{d2\mathrm{D}} w_s}{v} \propto \left(\frac{b_o}{v w_s} \right)^C, \ C \approx 0.3 \tag{4.8}$$

Adapting their results and including the effect of particle Reynolds number, Re_p (=$w_s d_{50}/v$), Equation (4.8) can be further expressed as

$$z_{d2\mathrm{D}} = 308 \, \mathrm{Re}_p \left(\frac{g'V_o}{v w_s L} \right)^{0.3} \frac{v}{w_s} \tag{4.9}$$

Bush *et al.* (2003) studied the 3D transitional depth into the dispersive phase for round sediment thermals. In their study, $z_{d3\mathrm{D}}$ was found to be Re_p-dependent at low Re_p. This dependency was attributed to the influence of particle-particle interactions, and decreased as Re_p increased. They proposed the following equation to compute $z_{d3\mathrm{D}}$ for Re_p in the range of 0.1 – 300:

$$z_{d3\mathrm{D}} = 11 \left(\frac{(g'V_o)^{1/2}}{w_s d_{50}} \right)^{5/6} d_{50} \tag{4.10}$$

Equations (4.9) and (4.10) are employed in our model to estimate the dispersive depth of 2D and 3D sediment thermals, respectively.

4.2.2 Computation of Gross Characteristics

The transient development of the gross characteristics (i.e. frontal velocity, u_f, frontal position, z_f and cloud radius, r_T) of the sediment cloud is computed from the asymptotic solutions of the respective flow regime. In the computation, three assumptions have been made: (i) the transitions between two flow regimes occur instantaneously; (ii) the average buoyancy flux of the starting plumes is used during the release (i.e. buoyancy flux per unit length, $q_o = B_o/Lt_e$ and buoyancy flux, $Q_o = B_o/t_e$, in other words the stem loss during the descent is negligible), and (iii) the sediment cloud in the starting plumes and thermals regimes has self-similar behavior.

Here, we would like to note that STFATE computes the gross characteristics by discretizing the volume of barged sediments into a sequence of three-dimensional instantaneous releases for the analysis (Johnson and Fong 1995). The total buoyancy excess of each release is varied with the insertion speed, u_{in} determined based on the gravitational force by the sediment depth remaining in the barge as follow:

$$u_{in} = \frac{(\rho_{AV} gh - \rho_a gd)}{\frac{1}{2}\rho_{AV}\left[1.0 + f - \left(\frac{A_1}{A_o}\right)^2\right]} \tag{4.11}$$

where ρ_{AV} is the average density of the remaining material in vessel, f is the friction factor; A_1 and A_o are the opening and inner areas of the disposal vessel. The number of releases, N (up to 6), can be specified by the user. Hence, the insertion speed is greatly influenced by N and t_e. Depending on the value inputted by the user, multiple possible solutions are computed for a single set of disposal conditions (e.g. V_o, L, W, d_{50}, etc.) (Dong *et al.* 2007) which is not physically realistic. Comparatively, BSDM calculates t_e directly from the disposal conditions and provides only a single solution for every condition.

For the third assumption of self-similar behaviour, the concept of simultaneous virtual distance and time origins (Zhao *et al.* 2012) is adopted at the transition point to provide a continuous connection between two flow regimes. The concept can be explained schematically in Figure 4.3. Essentially, both the virtual distance, z_o and time origins, t_o refer to the same virtual point source of buoyancy where the cloud originates with a zero radius. In the model, after the transition of flow regimes from 2D to 3D, the sediments are then assumed to be released from a virtual point source from the transition point onward.

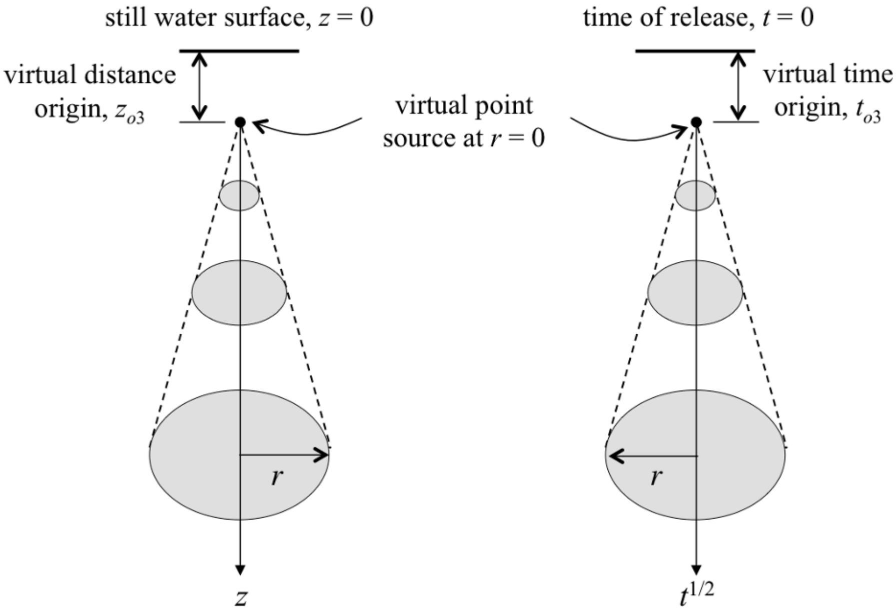

Figure 4.3 Simultaneous virtual distance and time origins (3D thermal)

4.2.2.1 Asymptotic Solutions

The gross characteristics of the sediment thermal in the self-preserving phase can be predicted by using the asymptotic solutions derived from miscible thermals with equivalent buoyancy (Rahimipour 1994). The solutions of u_f and r_T for the 2D starting plume were first derived by Tsang (1970) based on dimensional analysis as follow:

$$u_f = K_1 q_o^{1/3} \tag{4.12}$$

$$r_T = \alpha_{2DSP} z_f \tag{4.13}$$

Ching *et al.* (1993) also obtained the same expressions but with different values of K_1 and α_{2DSP} of 1.20 and 0.30, respectively. In the current experiments (discussed in the following), the value of K_1 and α_{2DSP} are found to be 1.29 and 0.29, which are very close to those suggested by Ching *et al.* (1993). In BSDM, the values from the current experiments are adopted.

For the 3D starting plume, the asymptotic solutions are adopted from Ai *et al.* (2006) as follow:

$$u_f = \frac{3}{4} K_2 Q_o^{1/4} \left(t - t_{o1}\right)^{-1/4} \tag{4.14}$$

$$r_T = \alpha_{3DSP}(z_f - z_{o1}) \tag{4.15}$$

Table 4.2 summarizes the values of K_2 and α_{3DSP} from previous studies (Turner 1962, Middleton 1975, Diez *et al.* 2003, Ai *et al.* 2006). The study by Ai *et al.* (2006) were performed with advanced Particle Image Velocimetry (PIV) and Planar Laser Induced Fluorescence (PLIF) which had a higher level of accuracy than the measurement approaches in other previous studies. Hence, their values are adopted in the model. However, the reported values are quite close to each other,and small variations do not have a significant effect on the model predictions.

The derivation of the solutions for 2D thermal is shown in the Appendix B, with Equations (B4) and (B6) representing the solutions of r_T and u_f, respectively. The value of α_{2DT} is adopted from Noh and Fernando (1993) who suggested a value of 0.46 for α_{2DT}. On the other hand, the solutions for 3D thermal are based on semi-analytical solutions, and the derivation is shown in the Appendix C with Equations (C6) and (C7) being the solutions of u_f and r_T, respectively. Note that, Bush *et al.* (2003) reported a value of 0.25 for the spreading rate of 3D sediment thermal, α_{3DT}.

4.2.2.2 Computation Steps

To summarize, the model adopts the following computation steps for the classification:

1. Determine the characteristics of the barged sediments to be disposed, such as q_o, Q_o, b_o and total excess buoyancy, B_o (= $g'V_o$)
2. Use the 2D starting plume solutions (Equations (4.12) and (4.13)) to calculate u_f and r_T until z_f reaches z_e or z_t
   - if $z_e < z_t$, the flow will transit into the 2D thermal regime first (Figure 4.4), otherwise the flow will transit into the 3D starting plume regime
3. Compute the virtual distance (z_{o2}) and time origin (t_{o2}) of the 2D thermal by Equations (B4) and (B6), respectively, with u_f and r_T being the values at $z_f = z_e$

4. Substitute z_{o2} and t_{o2} from step 3 into Equations (B4) and (B6), and then use these two equations to compute the u_f and r_T in the 2D thermal regime until z_f reaches z_t, after which the flow transits into the 3D thermal regime
5. Compute the virtual distance (z_{o3}) and time origin (t_{o3}) for the 3D thermal by Equations (C6) and (C7) with u_f and r_T being the values at $z_f = z_t$
6. Substitute z_{o3} and t_{o3} calculated from step 5 into Equations (C6) and (C7), and then compute the u_f and r_T in the 3D thermal regime.

Table 4.2 Summary of the values of K_2 and α_{3DSP} for 3D starting plumes

Previous studies	K_2	α_{3DSP}
Turner (1962)	2.54	0.18 ± 0.03
Middleton (1975)	2.43	0.18 ± 0.03
Diez *et al.* (2003)	2.70	0.16
Ai *et al.* (2006)	2.58	0.16 ± 0.03

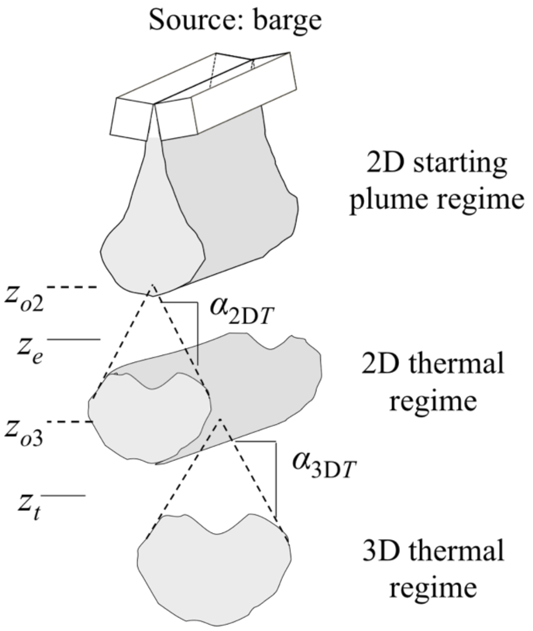

Figure 4.4 Development of flow regimes for barged sediment disposal

4.3 Experiments

4.3.1 Experimental Setup

The experiments in the present study were carried out in a water tank with dimensions of 2.4 m (length) × 2.2 m (height) × 1.2 m (width). The sides of the flume were constructed with glass to facilitate the image acquisition. Fresh water was used as the ambient fluid with a water depth of 2 m. A model barge (Figure 4.5, made with two rectangular acrylic boxes) was designed from an actual barge scaled down through volumetric scaling with dimensions of 20 cm (bin length, L) × 4 cm (bin height, D_b) × 4 cm (bin width, W_b). A finite amount (112g) of uniform-size particles (Ballotini Impact beads, Potters Industries, Inc.) with a density, ρ_s of 2.5 g/cm^3 was used as the sediments for all tests. Once the experiment was initiated, the two rectangular boxes would rotate in opposite directions with an angular speed, ω (= 1.5 rad/s), forming an opening in the middle through which the glass beads were released. In the present study, four particle sizes were considered: size A with a median diameter, d_{50} = 0.725 mm, B: 0.513 mm, D: 0.256 mm and AE: 0.120 mm. The opening width, W ranged from 0.5 to 4 cm was considered with the corresponded L/W had a similar value to that of the field situation. A complete list of experimental conditions was summarized in Table 4.3. Note that since L was fixed in the model barge, a larger L/W in the present experiments corresponded directly to a smaller LW.

The motions of the disposed sediments were illuminated by a spotlight and recorded using two video cameras (SONY HDR-XR550E & SONY HDR-CX900E, with a resolution of 1920 × 1080 pixels at 25 fps) from both the longitudinal and transverse directions (placement of video cameras shown in Figure 4.5). The extraction of gross characteristics of the sediment cloud from the experimental recorded videos was achieved through the 'Integrated Approach' using a customized MATLAB program. The gross characteristics (frontal position, z_f and cloud sizes, r_T and r_L) were defined in Section 3.2.3. Each test condition was repeated 5 times to ensure repeatability. The average results with the error bars showing the scattering were reported in the subsequent analyses.

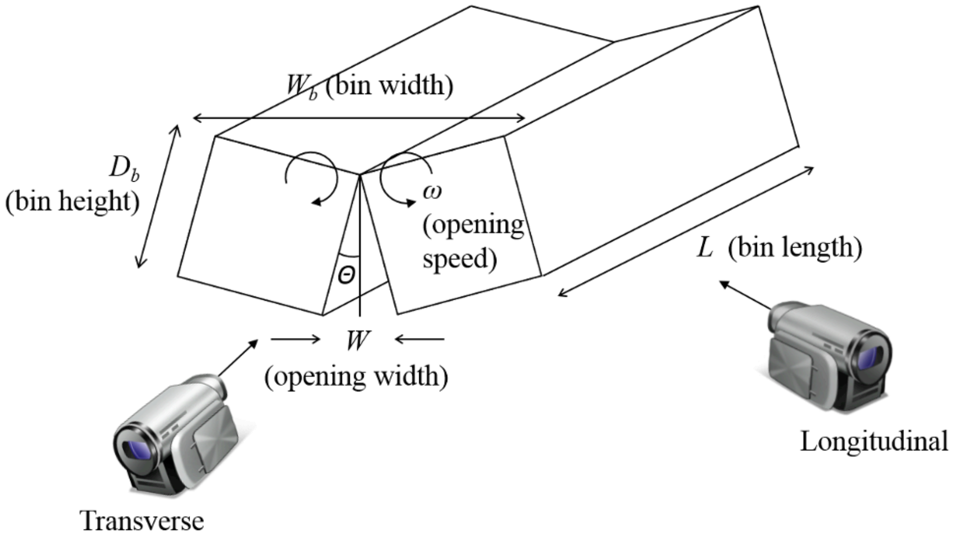

Figure 4.5 Placement of video cameras

Table 4.3 Experimental Conditions

Test Notation	W [cm]	L/W	LW [cm^2]	d_{50} [mm]	Re_p
A1LW05	4	5	80	A: 0.725	76.5
A1LW10	2	10	40		
A1LW24	0.8	24	17		
A1LW40	0.5	40	10		
A2LW05	4	5	80	B: 0.513	36.5
A2LW10	2	10	40		
A2LW24	0.8	24	17		
A2LW40	0.5	40	10		
A3LW05	4	5	80	D: 0.256	7.5
A3LW10	2	10	40		
A3LW24	0.8	24	17		
A3LW40	0.5	40	10		
A4LW05	4	5	80	AE: 0.120	1.2
A4LW10	2	10	40		
A4LW24	0.8	24	17		
A4LW40	0.5	40	10		

4.3.2 Experimental Observations

The descending motion of the sediment clouds after the barge release is shown in Figure 4.6. The dark pixels (or area) illustrate the area covered by sediments. The value of t_e for each experiment is indicated in the figure. Clearly, when $t < t_e$, the sediments can be observed to discharge continuously from the barge opening with a 'thermal-like' front head, and the sediment cloud had a typical tadpole shape similar to the buoyant starting plume described by Tsang (1970) and Ai *et al.* (2006). After the sediments were emptied from the barge at a larger time when $t > t_e$, the sediment cloud then descended in a self-preserving manner. Later on, the sediment cloud entered the dispersive phase when the descending velocity slowed to the level of particle settling velocity.

In some experiments (e.g. A1LW05), the starting plume regime only lasted momentarily after the release was initiated. When L/W increased (e.g. Experiment A1LW40), the sediments would discharge at a slower rate due to the narrower opening width. As a result, the starting plume regime was extended for a longer time. Comparing Experiments A1LW05 and A4LW05 with the same L/W, the value of t_e increased when d_{50} decreased. Thus, the starting plume regime was easier to be achieved with smaller d_{50} and larger L/W. For example, comparing Experiments A1LW05 and A4LW40, the tadpole shape of the starting plume regime was easily captured in the later case.

Figure 4.7 illustrates the development of the sediment cloud during Experiment A3LW40 in both longitudinal and transverse directions. The black horizontal line marks the vertical location where the transition from two-dimensional (2D) to three-dimensional (3D) flow regimes occurred. The depth of this transition point is defined as the transition depth, z_t. The dashed lines plot the spreading of the sediment cloud, with the slope representing the spreading rate, α. From the figure, it can be seen that the spreading rate in the longitudinal direction, α_{L1} was less than the transverse direction, α_T in the beginning of the descent process. When the transverse radius, r_T subsequently reached a size comparable to the longitudinal radius, r_L, it began to grow at the same rate ($\alpha_{L2} \approx \alpha_T$). Viewed from the top, the observation above showed that the sediment cloud transited from approximately elliptical to circular. Hence, the flow regimes were governed by the comparative spreading rates in the two directions. In 2D flow regimes, α_L is generally small compared to α_T. However, in 3D flow regimes, the spreading in both directions are similar. For barge releases, the sediment cloud behaves in a 2D manner in the beginning of the descent process, and then transits to 3D when the frontal position of the sediment cloud reaches z_t.

In summary, the flow regimes experienced by the sediment cloud can be categorized into starting plumes and thermals as well as 2D and 3D flow regimes. The experimental results also suggested that the transition depths, z_e and z_t are strongly related to the geometry of the barge opening and d_{50}.

4.3.2.1 Two-dimensional Starting Plume Regime

In all the experiments, at the beginning of the descent process, a 2D starting plume regime typically occurred with the sediments continuously released from the barge and negligible longitudinal entrainment. The results at the initial time were compared to the asymptotic solution of a 2D starting plume. Note that Tsang (1970) and Ching *et al.* (1993) found a linear relationship between the frontal position of a starting plume and the time of discharge, t (i.e. $z_f \sim t$) with the coefficient of proportionality, K_1 ranging from 1 to 1.2.

Figure 4.8 plots the transient development of the sediment cloud frontal position with time. The data are plotted in the region where $z_f < z_e$ and/or z_t. The characteristics scales, L_n and T_n are defined as

$$L_n = q_o^{2/3} g'^{-1}, \; T_n = q_o^{1/3} g'^{-1} \tag{4.16}$$

and they are used to normalize the experimental results in the 2D starting plume regime. The values of q_o are assumed to be constant for each test condition within the starting plume regime. In the figure, the normalized results tend to collapse into a single linear curve, with an average slope of 1.29. The linearity of the curves illustrates that the assumption of constant q_o is valid and the slope indicates that starting sediment plumes descend slightly faster than the corresponding single-phase starting plume. Figure 4.9 shows the lateral growth of a 2D starting plume in the transverse direction. The fitted spreading rate, α_{2DSP} is 0.29, which is very similar to the spreading rate of a single-phase starting plume.

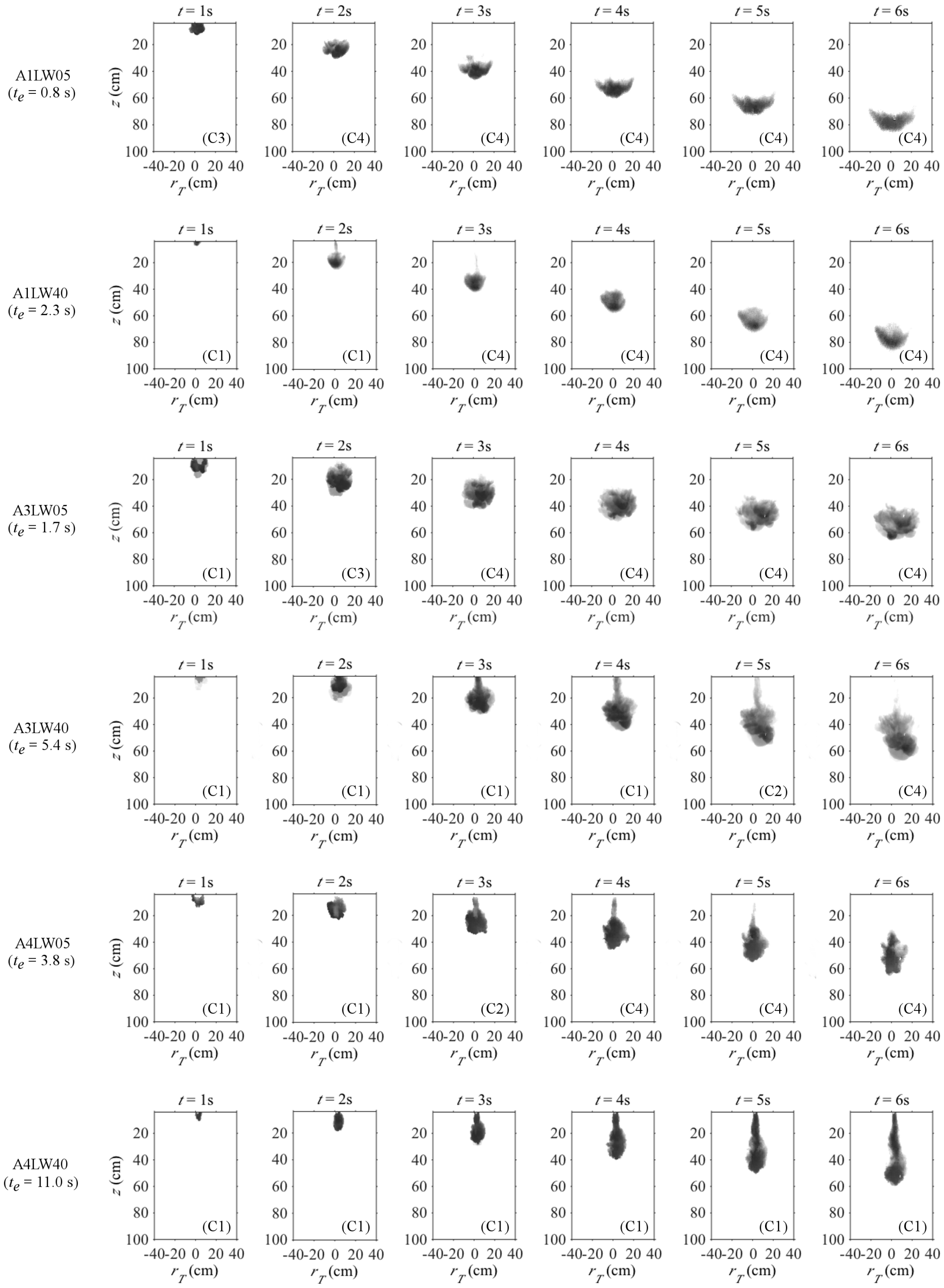

Figure 4.6 The descending motion of sediment clouds released from barge (Note that the features of 2D and 3D regimes can not be observed from this figure as the sediment clouds are recorded from the transverse direction)

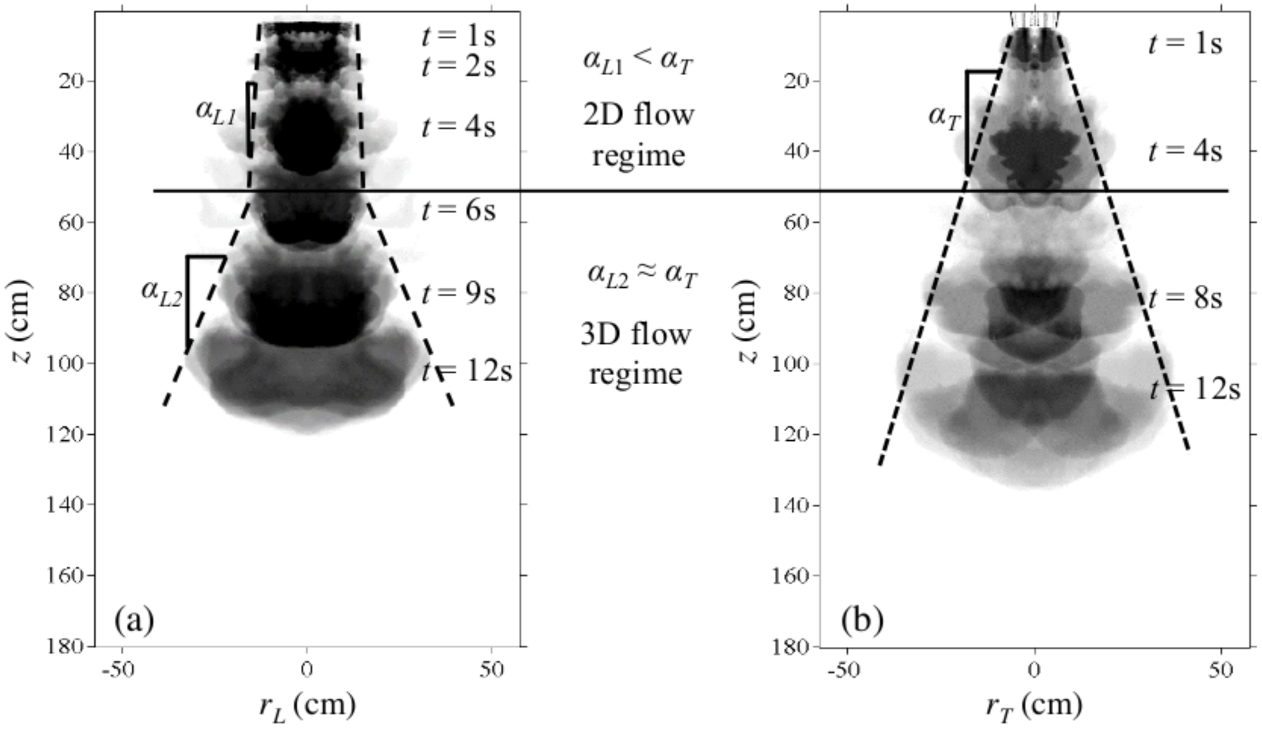

Figure 4.7 The development of the sediment clouds in (a) longitudinal and (b) transverse directions from Experiment A3LW40

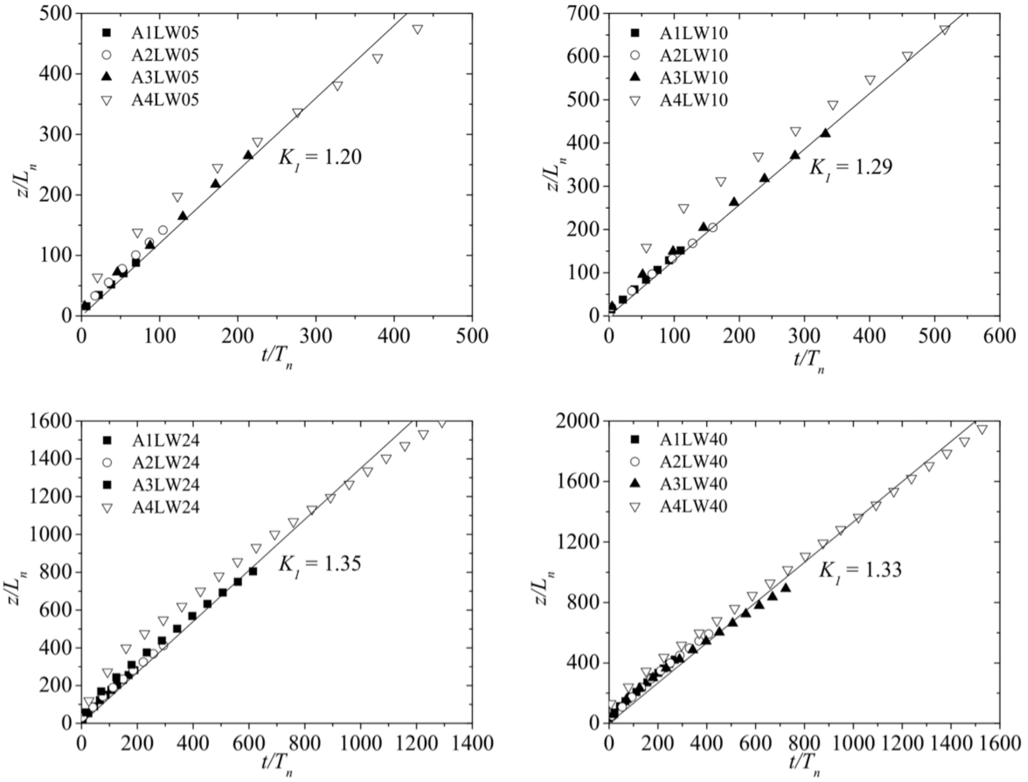

Figure 4.8 Normalized cloud frontal position, z_f/L_n versus time, t/T_n in the two-dimensional starting plume regime

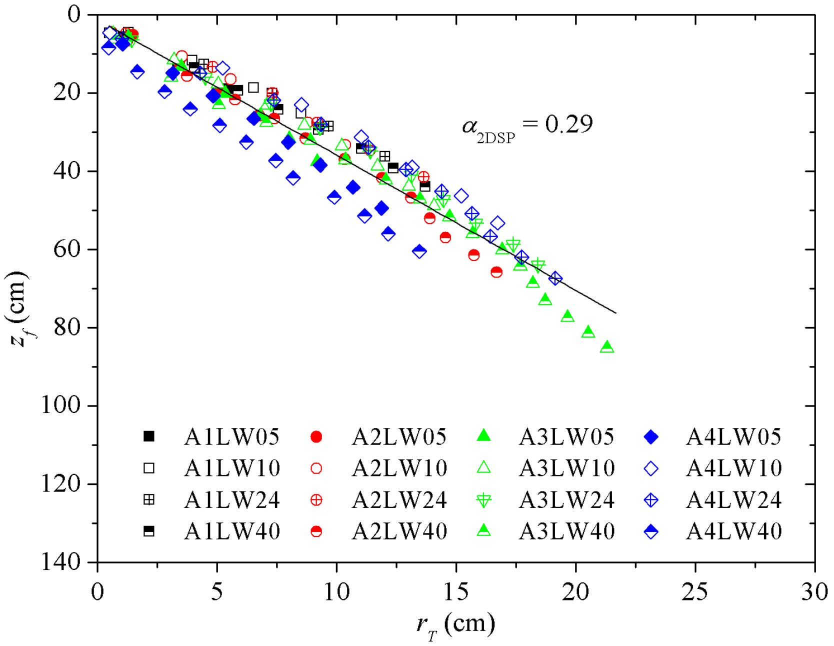

Figure 4.9 Cloud transverse radius, r_T versus frontal position, z_f in the two-dimensional starting plume regime

4.3.2.2 Equations Calibration

In order to determine the functional forms of t_e, z_e and z_t, Equations (4.4), (4.5) and (4.7) were calibrated with t_e, z_e and z_t obtained from the experiments. The variations of dimensionless t_e with $LW/V_o^{2/3}$ are shown in Figure 4.10. The linearity of the logarithmic plotted data illustrates the following relationship:

$$t_e\sqrt{\frac{g'}{V_o^{1/3}}} \sim \left(\frac{LW}{V_o^{2/3}}\right)^a \tag{4.17}$$

with a = -0.55, from the slope of the best-fitted lines. Thus, Equation (4.4) can be expressed as

$$t_e\sqrt{\frac{g'}{V_o^{1/3}}} \Bigg/ \left(\frac{LW}{V_o^{2/3}}\right)^{-0.55} = f_8\left(D^*\right) \tag{4.18}$$

Subsequently, by plotting t_e against D^* as shown in Figure 4.11, we obtain:

$$t_e = C_1\left(D^*\right)^{a_1}\left(\frac{LW}{V_o^{2/3}}\right)^{-0.55}\sqrt{\frac{V_o^{1/3}}{g'}} \tag{4.19}$$

with C_1 = 481 and a_1 = -0.96 from the best-fitted results from Figure 4.11.

The variations of z_e from the experimental results are plotted in Figure 4.12. The following form can be established from the data:

$$z_e = C_2\left(\frac{t_e\sqrt{g'}}{V_o^{1/6}}\right)^{a_2} V_o^{1/3} \tag{4.20}$$

where C_2 and a_2 are found to be 1.0 and 0.61, respectively, based on the best-fitted curves plotted in Figure 4.12.

The relationship between z_t and L/W as well as t_e is presented in Figure 4.13. The x-axis was formulated to fulfill the two following conditions discussed previously (i.e. z_t = 0 when L/W = 1 and z_t increases with L/W). Note that z_t increased with t_e due to the fact that the spreading of starting plumes is less than that of round thermals (i.e. $\alpha_{2DSP} = 0.29 < \alpha_{2DT} = 0.46$) in the 2D regimes. In Figure 4.13, the best-fitted line of the data yields

$$z_t = C_3\left[\left(\frac{t_e\sqrt{g'}}{\sqrt{L}}\right)\log\left(\frac{L}{W}\right)\right]^{a_3} L \qquad (4.21)$$

with C_3 = 0.62 and a_3 = 0.33. In the subsequent analyses, Equations (4.19), (4.20) and (4.21) are employed to compute t_e, z_e and z_t, respectively for the comparisons of flow regimes and gross characteristics.

4.4 Comparison of Model Predictions with Experimental Data

4.4.1 Flow Regime Analysis

Here, a total of four asymptotic cases (2D and 3D starting plumes as well as thermals) and two different cases of dispersive phases are analyzed. The frontal velocity, u_f, and z_f are plotted in logarithmic scale, and the slope, n of the line is compared with the n value of the asymptotic cases as follow:

$$u_f \sim z_f^{\ n} \qquad (4.22)$$

From the literature, the values of n for the four asymptotic cases are summarized in Table 4.4. The data plots from Figures 4.14 to 4.17 are obtained from the experiments. The solid and dash lines in the figures represent z_e and z_t from Equations (4.20) and (4.21), respectively. The values of z_d are marked in the figures with solid lines and crosses at the ends.

The length parameters, z_e, z_t and z_d, divide the plot into different regions. The value of n in each region is stated on the graph and compared with the flow regime predicted by BSDM. The comparison indicates that the experimental results and model predictions are generally in good agreement; the few exceptions are marked in italics.

With L/W = 5, Figure 4.14 shows that the experimental results generally agree with the model predictions, but that results from two regions have some small differences. For Experiments A1LW05 and A2LW05, in the regions between z_t and z_d, the model suggests that the sediment cloud had entered the 3D thermal regime

(C4) while the value of *n* implied otherwise. This can be explained by the fact that the transition of the sediment clouds from the thermal phase to the dispersive phase is gradual and not abrupt as assumed in the present model. However, the differences due to the assumption are small, and the detailed two-phase behaviour can only be described accurately with two-phase approaches such as Lai *et al.* (2013).

In the initial stage of the settling process, the 2D starting plume regime (C1) was generally predicted and observed as discussed in previous section. However, in some cases (i.e. A4LW10, A4LW24, A3LW24 and A3LW40), the values of *n* implied otherwise. This may be due to the existence of a momentum-dominated region that is usually found before the starting plume regime (Tsang 1970). Figures 4.15 to 4.17 suggest that the effect of this region increases when *L/W* increases.

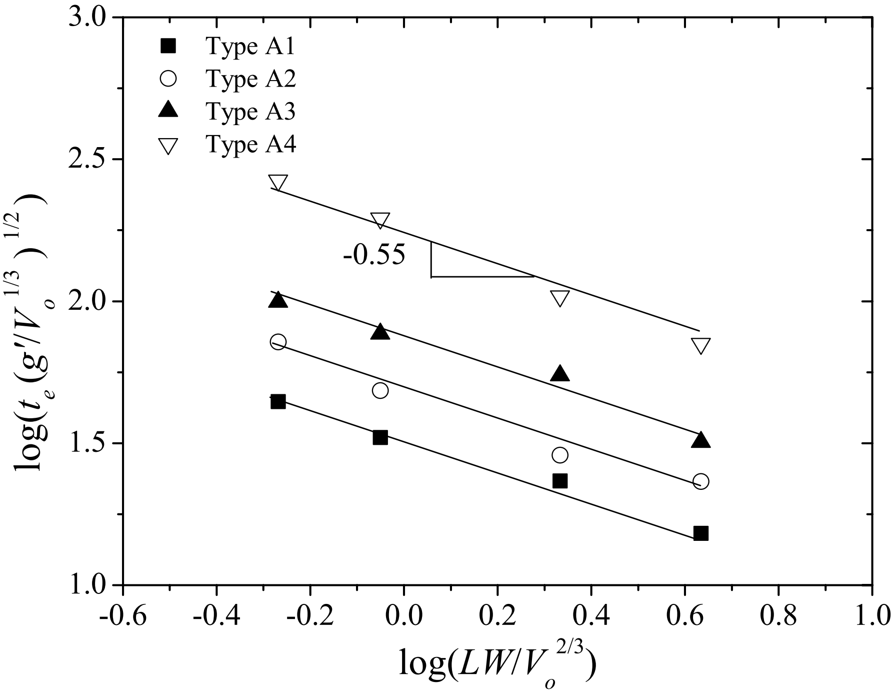

Figure 4.10 Relationship between barge empty time, $t_e(g'/V_o^{1/3})^{1/2}$ and opening area, $LW/V_o^{2/3}$

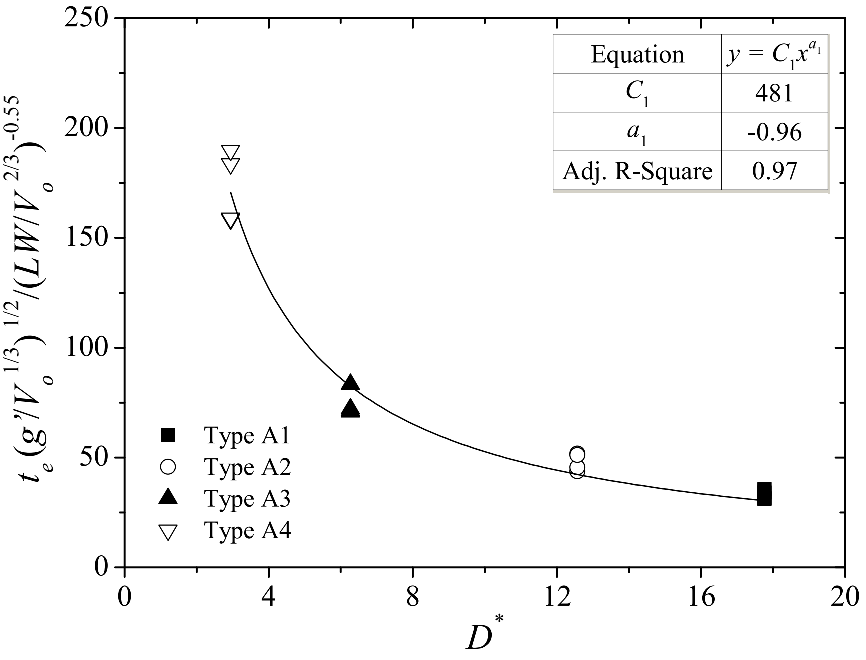

Figure 4.11 Relationship between barge empty time, $t_e(g'/V_o^{1/3})^{1/2}/(LW/V_o^{2/3})^{-0.55}$ and dimensionless particle diameter, D^* (solid line represents the best-fitted line of the data)

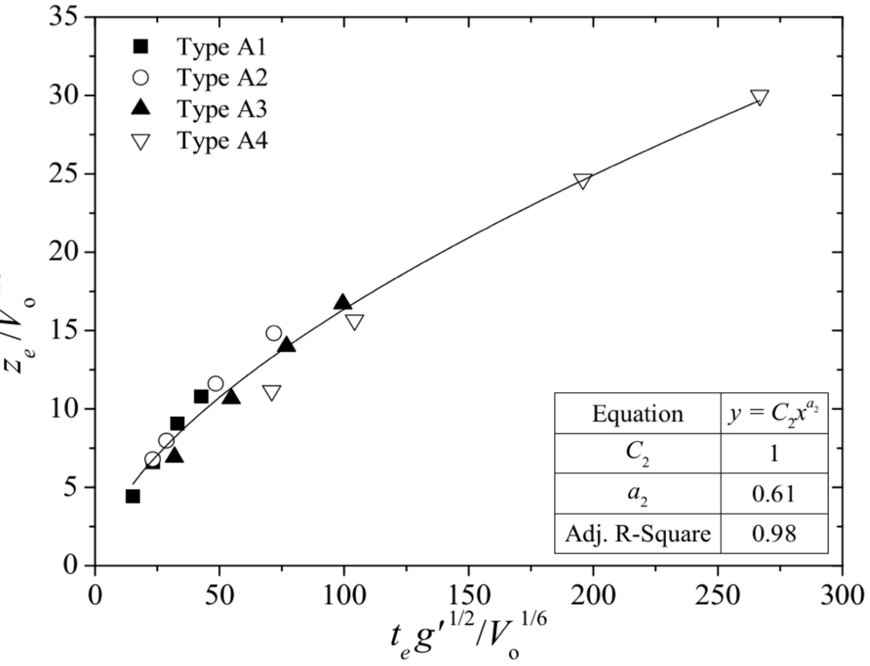

Figure 4.12 Relationship between empty depth, z_e and barge empty time, t_e (solid line represents the best-fitted line of the data)

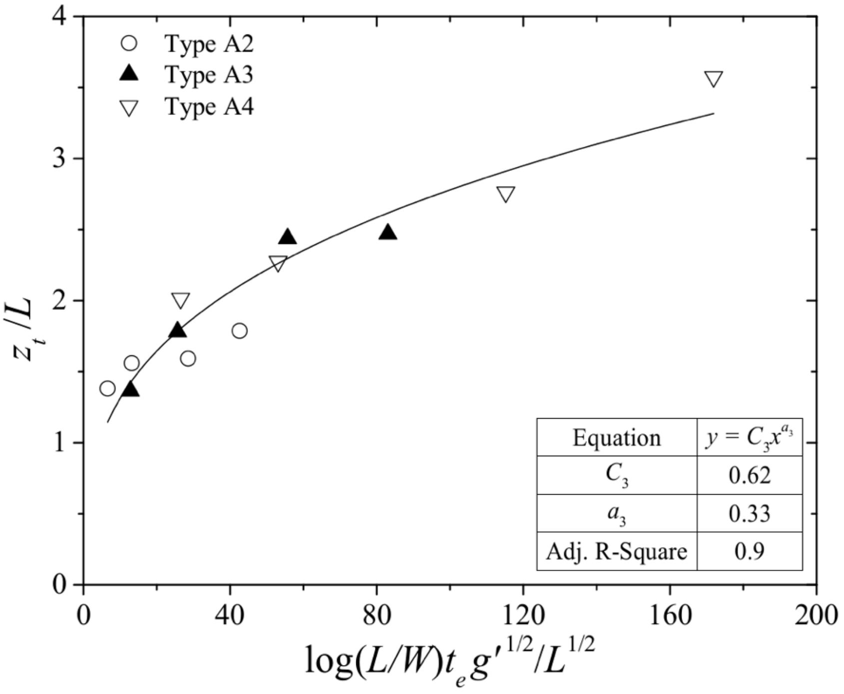

Figure 4.13 Relationship between transition depth, z_t and opening aspect ratio, *L/W* as well as barge empty time, t_e (solid line represents the best-fitted line of the data)

Table 4.4 Values of *n* (Equation (4.22)) for the four asymptotic cases

Category	Starting Plume	Thermal
2D	C1, $n = 0$ (Tsang 1970)	C3, $n = -0.5$ (Noh and Fernando 1993)
3D	C2, $n = -0.51 \sim -0.28$ (Turner 1962)	C4, $n = -1$ (Scorer 1957)

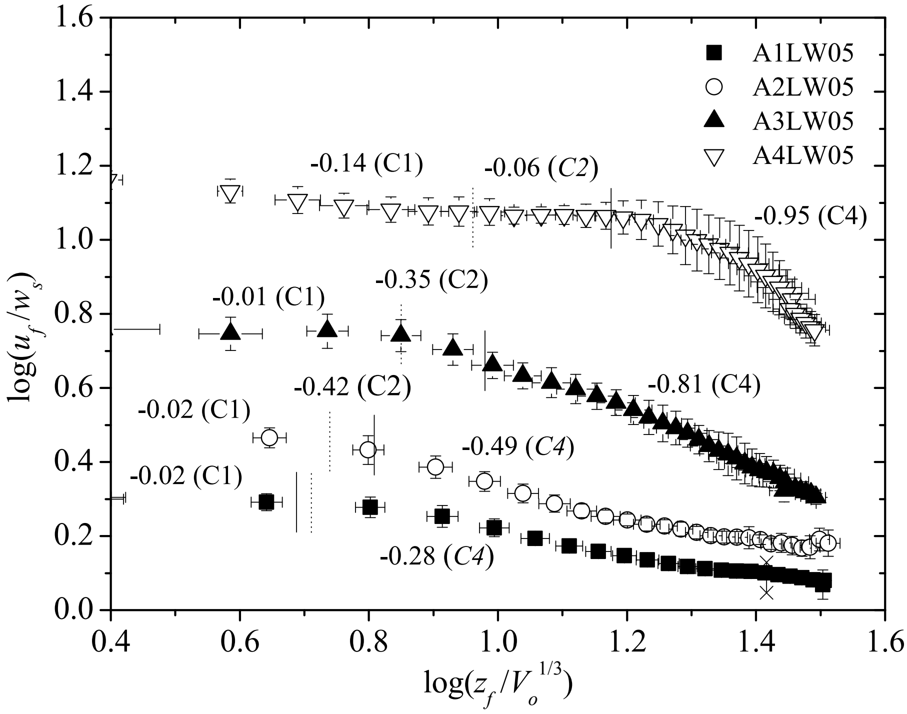

Figure 4.14 Development of frontal velocity, u_f with distance (L/W = 5)

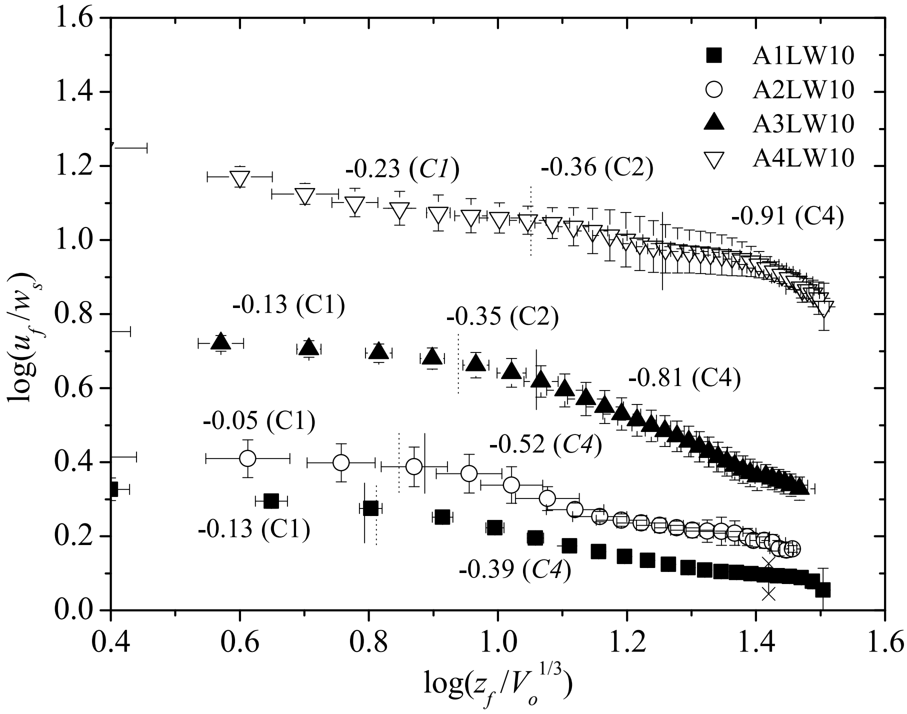

Figure 4.15 Development of frontal velocity, u_f with distance (L/W = 10)

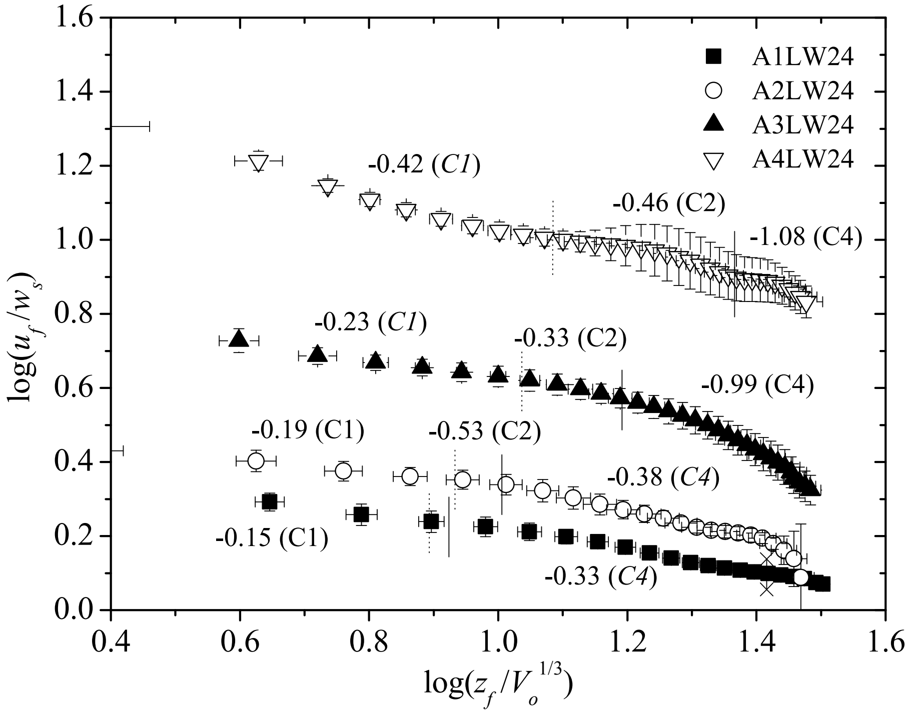

Figure 4.16 Development of frontal velocity, u_f with distance (*L/W* = 24)

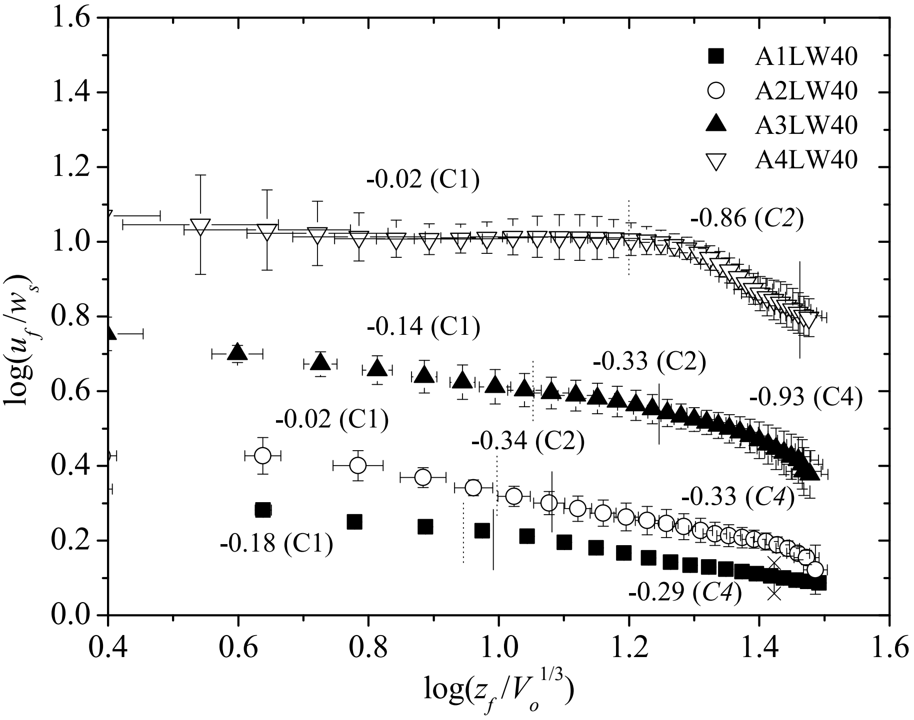

Figure 4.17 Development of frontal velocity, u_f with distance (*L/W* = 40)

4.4.2 Gross Characteristics Comparison

In Figure 4.18, the transient development of the frontal position, z_f with radius, r_T from four experiments (A3LW05, A3LW40, A4LW05 and A4LW40) are compared with model predictions. Note that the length scale ratio between the laboratory and field was calculated to be approximately equal to 230. Hence, the comparison covers the realistic depth of most disposal sites. For Experiment A3LW05, the geometric characteristics of the sediment cloud were well predicted by the present model. For Experiment A3LW40, the present model performed very well as shown in Figures 4.18 c and d. The slight deviation in the penetration depth prediction might be due to the momentum-dominated region, which shifted the virtual origin of the staring plume.

For Experiment A4LW05, the geometric characteristics of the sediment cloud were again well predicted by the present model, despite the under-estimation in r_T at the beginning. In Experiment A4LW40, the penetration depth was under-estimated by ~14%, which might also be due to the momentum-dominated region. The prediction for the cloud size was however very good as shown in Figure 4.18 (h).

Figure 4.18 also includes the simulated results from the earlier K&C and STFATE models. The predictions from K&C's model are the same for every case because the effects of L/W and d_{50} are not considered; and in STFATE, L/W only affects the insertion speed of the sediment layer. Overall, our model has substantially improved the predictions of the gross characteristics of the barge-disposed sediments as shown in the figure.

As stated above, there remain at least two limitations in our model. First, the momentum-dominated region is not considered which might be significant when L/W is large. Second, the transitions between flow regimes in the model are assumed to be abrupt, with sharp transitions between two adjacent regimes, whereas in reality the transitions are more gradual. However, the analysis indicates that the two effects were not overly significant within the experimental range.

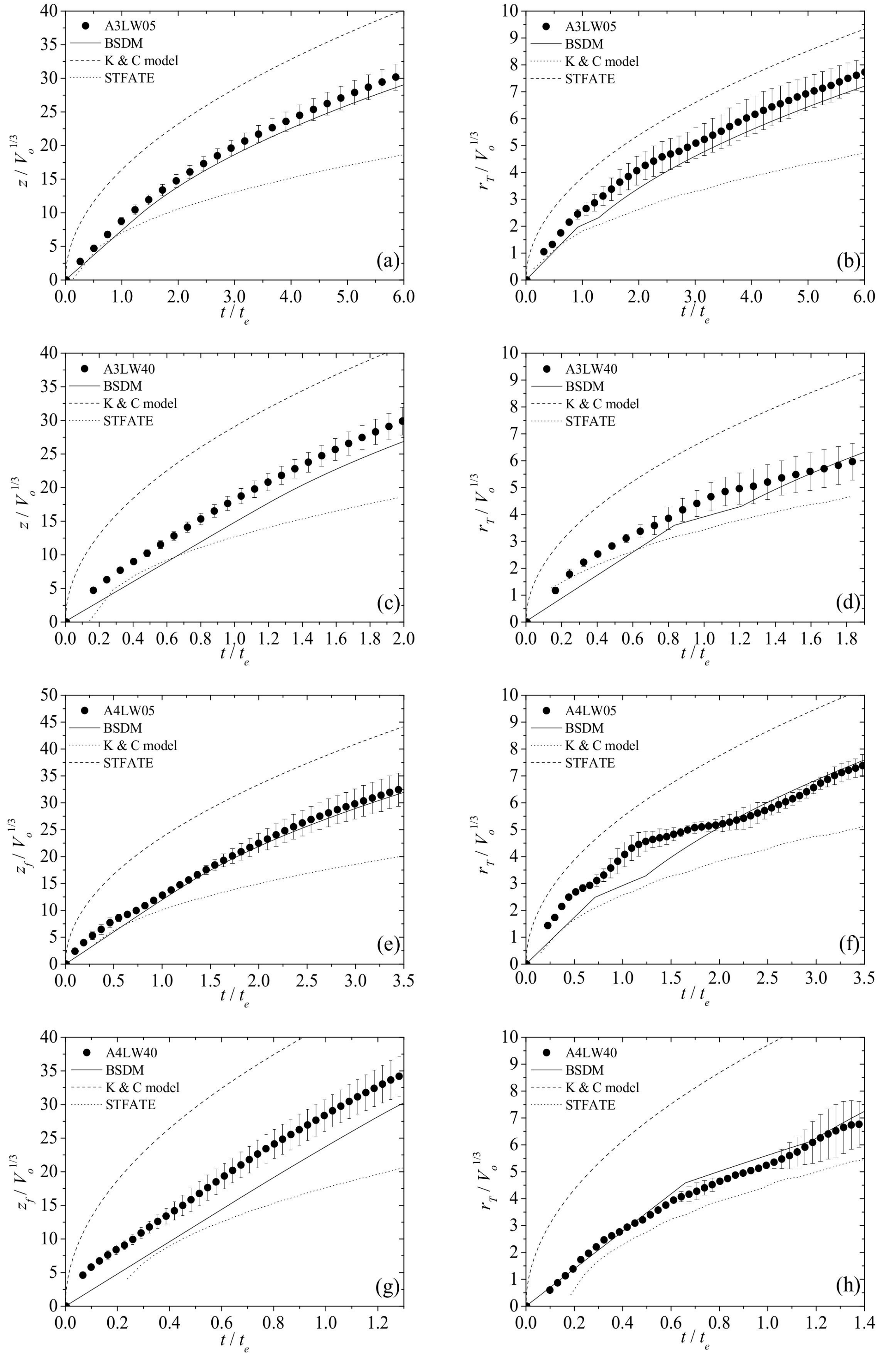

Figure 4.18 Comparison between experimental results and model predictions for the development of normalized frontal position, z_f and radius, r_T versus time

4.5 Comparison of Model Predictions with Field Data

As an application example, we simulated the field disposal operation (Disposal No. 7 at the Lake Ontario in Rochester, NY) recorded in Bokuniewicz *et al.* (1978) with BSDM. Based on the Table 2 in Bokuniewicz *et al.* (1978) (reproduced in Table 4.5) that summarized the operation conditions, 443 m^3 of dredged material was discharged through the U. S. Hopper Dredge Lyman. The discharged material consisted of mainly high water content disposal material with the density of 1.2×10^3 kg/m^3. The descent of the leading edge of the cloud, z_f was recorded with an echo sounder and the result was shown in Figure 10 in Bokuniewicz *et al.* (1978).

The difference between the disposal from a hopper dredge and barge is that the disposed sediments from a single hopper will descend as an individual cloud at the beginning. When the size of the cloud, r_T exceeds half of the spacing between the openings of adjacent hoppers (i.e. $r_T > S/2$, S is the spacing), the sediment clouds will merge and descend as a group (as shown in Figure 1 in Bokuniewicz et al. (1978)). In BSDM simulations, we have taken that the data recorded in Bokuniewicz *et al.* (1978) was the horizontal integration of 4 individual descending clouds (i.e. 4 hoppers were used). Thus, V_o = 111 m^3 (volume carried by a single hopper), t_e = 54 s, $L = W$ = 1.01 m (bottom opening area of a single hopper was 1.03 m^2) and $\rho_s = 1.2 \times 10^3$ kg/m^3. The z_f predicted by BSDM is compared with the field observation in Figure 4.19.

The comparison shows that the present model performed very well, with the time for the sediment cloud to impact the sea bed only differing from data by ~ 20 %. The prediction from STFATE, however, was far off and unavailable when $t <$ 10.5 s. This might be due to the fact that the first layer of sediment was still discharging when $t <$ 10.5 s, and the simulation only began when the first layer was fully discharged. Furthermore, the sediment cloud velocity upon impact on the seabed ($\mathrm{d}z_f/\mathrm{d}t$ at z = 14 m), which might affect the subsequent horizontal spreading of the collapsed cloud, was also well predicted by the present model.

Table 4.5 Properties of dredged material

Site	Mass of Solids [kg]	Mass of Water [kg]	Mass Ratio Solids/Water	Mean Density [kg/m^3]
Rochester	2.1×10^5	6.1×10^5	0.3	1.2×10^3

Note: Data from Bokuniewicz *et al.* (1978)

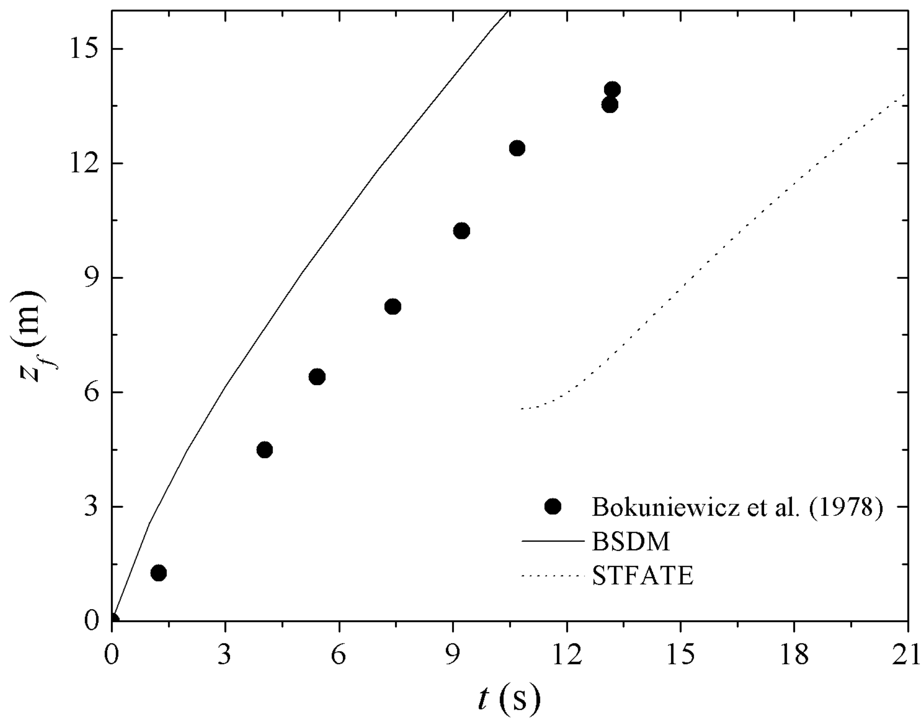

Figure 4.19 Comparison between field observation and model predictions for the development of frontal position, z_f versus time

4.6 Summary and Conclusions

In the present study, a new model (BSDM) is developed for the assessment of the open water disposal of barged sediments based on the classification scheme with six different flow regimes (four asymptotic cases: two- and three-dimensional starting plumes as well as thermals plus two cases of dispersive regimes). Each regime is quantified with equations either from the present experiments or data from past literature. The model provides both qualitative and quantitative predictions of the behavior of barged disposed sediment cloud. An experimental investigation was carried out for the verification. The experimental results showed that the predictions from BSDM are substantially better than the existing models of K&C and STFATE. The predictions of the actual field disposal operation of Bokuniewicz *et al.* (1978) was also in good agreement with the recorded field data.

From engineering perspectives, BSDM can be used to determine the parameters of the disposal operation (i.e. barge geometry with the opening aspect ratio, *L/W*, etc.) to target a specific regime for the convective descent phase in consideration of the size of the sediments being disposed. For example, to reduce the possibility of losing the sediments to ambient currents and waves as turbidity (Gensheimer *et al.* 2012, Zhao *et al.* 2013a), it would be desirable for the sediment cloud to be maintained in the thermal/plume regime before the bottom impact (Johnson *et al.* 2008). The assessment from BSDM is expected to be more accurate compared to STAFTE, which is widely used in the industry at present (Howlett 2003, Bailey *et al.* 2004, EPA 2004, Dong *et al.* 2007). The gross characteristics of the sediment cloud at the bottom impact can also be computed to evaluate the penetration potential of the cloud into the seabed deposit, for consideration in the dumping of sand covers over confined bottom cells for contaminated sediments (Eek *et al.* 2008).

Chapter 5

An Improved Light Attenuation Method for 2D Data Acquisition

5.1 Introduction

In this chapter, we introduced a measurement technique, light attenuation method and our contribution to the improved technique, which will be utilized in the next chapter. Laboratory investigations of sediment deposition and bathymetry changes require the accurate measurements of sediment distribution over the affected area. Previous measurement techniques to achieve this objective had been summarized in details by Munro and Dalziel (2005). They included the ultrasonic depth profiler and stereo-photography which have limited spatial resolution, and also the laser 3D scanner which has high accuracy but is expensive with long acquisition time (Lague *et al.* 2003). Alternatively, Rooij *et al.* (1999) employed an array of electrodes on the bottom of the tank to determine the sediment depth based on the resistance induced through the sediment layer. This method enables real time measurements, but is limited by the range of sediment depths as the voltage signal quickly saturates in a deep sediment layer. In addition, the measurement extent is restricted by the coverage of the electrodes. Munro *et al.* (2004) developed a novel technique by comparing the reference image (image of undisturbed sediment layer) with the new image after the redistribution of sediment particles. Through a pattern-matching algorithm, high-resolution particle redistribution measurements were obtained. However, this technique was found to be impractical in terms of real time

---

Note: The material presented in this chapter has been submitted to Journal of Hydraulics Engineering for the consideration of publication measurements. Subsequently, Munro and Dalziel (2005) proposed instead a light attenuation method (LAM) to resolve the temporal displacement of particles, which we shall review in details in the following.

Light attenuation methods have been successfully applied to a wide range of studies involving single-phase flows. Holford and Dalziel (1996) used this method for the visualization and quantification of baroclinic instability of a two-layer rotating fluid system. Cenedese and Dalziel (1998) and Kikkert *et al.* (2007) applied LAM to measure the depth-averaged concentration of a single-phase buoyant convective flow. Besides single-phase flows, LAM had also been used to investigate two-phase flows (i.e. air-water, solid-water flows), e.g. measuring the void fraction of micro bubbles (Leppinen and Dalziel 2001), gravity currents (Yuan *et al.* 2011), and the particle displacement or deposition in aqueous environments (Munro and Dalziel 2005, Yoshida *et al.* 2012, Sutherland and Dalziel 2014).

The principle of LAM and the derivation of equations had been discussed in Chapter 3. In general, LAM utilizes the relationship between sediment thickness, h_s and the respective attenuated intensity, I/I_{ref}, which can be mathematically expressed as:

$$I/I_{ref} = f_8\,(h_s,\, d_{50}) \tag{5.1}$$

where I and I_{ref} are the attenuated and reference intensities, respectively, d_{50} is the sediment size. Sediment profiles deposited from different sediment sizes are expected to have different attenuation characteristics or calibration curves, as the scattering of light through a sphere is affected by the size of sphere (Jonasz and Fournier 2011).

5.1.1 Previous Calibration

Calibration is required to establish the functional form of Equation (5.1) (i.e. the calibration curve). Munro and Dalziel (2005) used sediment particles with d_{50} = 0.25 mm, and prepared calibration profiles by scraping the sediment to a constant thickness or a linearly slope depth and measuring the attenuated intensity, I, of the profiles. The scraping method worked adequately for sediment thickness $h_s > 2$ mm or $h_s/d_{50} > 8$ if $d_{50} = 0.25$ mm. By plotting the normalized attenuated intensity, I/I_{ref}

with the sediment thickness, h_s/d_{50}, they observed an exponential decay when h_s/d_{50} > 18 as expected from Beer-Lambert's law, and called this region the self-similar regime. An exponential fit of the data was performed in this regime as

$$\frac{I}{I_s} = \exp\left\{\beta\left(\frac{h_s - h_{crit}}{d_{50}}\right)\right\},\ h_s > h_{crit} \tag{5.2}$$

where I_s is the intensity at $h_s = h_{crit}$ and h_{crit} is the critical h_s determined to be $18d_{50}$. The regime with $h_s/d_{50} < 18$ was termed the near-zero limit regime, and the attenuation disobeyed Beer-Lambert's law. In this regime, they performed a least square fit with the following equation chosen for empirical convenience:

$$\frac{I}{I_{ref}} = \exp\left\{\kappa\left(\frac{h_s}{d_{50}}\right)^{\gamma}\right\} \tag{5.3}$$

where κ and γ are the empirical coefficients that fitted with all the data (including the data in self-similar regime) but constrained to $I/I_{ref} = 1$ at $h_s/d_{50} = 0$ and $I/I_{ref} \rightarrow 0$ when $h_s/d_{50} \rightarrow \infty$. Overall, the calibration profiles prepared by Munro and Dalziel (2005) were appropriate for coarse sediments (i.e. large d_{50}) as a wide range of h_s/d_{50} (from near-zero limit to self-similar regimes) could be covered.

Our focus on the further development of the LAM method in this study stemmed from our ongoing interest related to the deposition of sediment clouds occurring during open water barged sediment disposal. Typically, the sediment size used in our laboratory experiments was approximately 0.12 mm (fine to very fine sand) as determined from Froude scaling of field grain sizes (Wang *et al.* 2015), whereby a small value of h_s (< 2 mm) would be expected based on preliminary experimental observations. Hence, although the range of h_s/d_{50} might be similar to that of in Munro's study (from near-zero limit to self-similar regimes), the values of h_s that needed to be determined were shallower (since finer d_{50} was used) and could not be suitably prepared using the scraper method.

In the present study, we established an improved light attenuation method (LAM2D – Light Attenuation Method with 2D Data Acquisition), which utilized different techniques to prepare the calibration curves. For deeper h_s (h_s > 2 mm), the traditional scraping method was used. For shallower h_s (h_s < 2 mm), however, an innovative technique using the deposition profiles produced by a particle plume, which had small and measurable thickness, h_s was used instead. The calibration curves in the two regimes were established solely with data collected in the respective regime. In the following, the experimental setup, particularly the novel calibration technique developed to calibrate the shallow h_s, is first presented. This is followed by the improved calibration results of the current method (LAM2D). Finally, the measurements of deposition profiles from barged sediment disposal with high accuracy are demonstrated.

5.2 Experimental Setup

In the present study, the experiments were conducted in a 2 m (long) × 0.9 m (high) × 0.85 m (wide) glass tank. The bottom of the tank was constructed with transparent glass to facilitate backlighting. Fresh water was used as the ambient fluid with water depth, h = 10 cm. Uniform-size particles (Ballotini Impact beads, Potters Industries, Inc.) with a density, ρ_s of 2.5 g/cm^3 and size, d_{50} of 0.12 mm were used as the sediment particles for most of the experiments.

5.2.1 Light Attenuation System

5.2.1.1 Light Panel

The design of light panel was critical for this technique and should be customized based on the several criteria as discussed in Chapter 3. In the present study, the light panel was fabricated with fourteen 1.5 m (~5 ft.) long T8 fluorescent tubes, arranged equal in distant covering a width of 0.85 m in an aluminum rectangular box with a depth of ~ 15 cm. The panel was placed horizontally under the glass tank facing upward as shown in Figure 5.1.

Before the experiments, the light panel was tested for light uniformity as well as consistency over short (i.e. within an hour) and intermediate (i.e. within weeks) periods of time. The results showed that the light panel was able to produce a uniform light sheet with a low coefficient of variance, C.O.V ≈ 1.6 % over a areal domain of 1.0 × 0.5 m^2, which was sufficient to determine the deposition profiles from barged sediment disposal in the present experiments. Due to the temperature dependence of the fluorescent tube, the light intensity was expected to fluctuate over time as the temperature increased with the test duration. The variation of intensity over time was recorded and plotted in Figure 5.2. From the figure, the intensity was observed to be stable within the first 40 minutes after the panel was switched on, and the temperature maintained the same as the room temperature (~ 20 – 22 °C). We therefore limited the test duration to 40 minutes, while the minimum value of light intensity was chosen based on the lowest intensities that would be observed in the experiments. Note that the dimensions of the lighting area and the intensity consistency over time were dependent on the design and the light source of light panel.

5.2.1.2 Camera

A Nikon D700 DSLR (Digital Single-Lens Reflex) camera with CMOS and color sensor, equipped with a 24-70 mm *f*/2.8L lens was employed in the setup. The camera was mounted on top of the water tank with 1 m apart from the bottom of the tank, facing vertically downward toward the light panel as shown in Figure 5.1. Previous studies typically used a CCD camera with a global shutter for the image capturing. Comparatively a CMOS camera usually operates with a rolling shutter (Konz *et al.* 2009, Njifenju *et al.* 2013). Due to the functional principle of the rolling shutter, the issue of flicker intensity was expected (Yoo *et al.* 2014) and flickering was indeed observed in the current setup. To mitigate this issue, the camera exposure time, t_c was increased to average over the flickering light bands. With the current light panel, $t_c > 1/40$ was found to be sufficient. Besides the exposure time, other parameters such as the *f*-stop (f/n), ISO sensitivity and white balance were adjusted to achieve I_{ref} in a range of 240 ~ 250 (8 bits per pixel, giving integer intensity levels of $0 \leq I \leq 255$). The selection criteria for each parameter are discussed in Table 5.1. The final set of parameters chosen was: $t_c = 1/30$, ISO = 400 and $f/n = f/22$.

With the color sensor, three-color signals (red, green and blue) were recorded and analyzed. From the results, the blue signal attenuated the most and hence yield the best resolution for the calibration curves. In the subsequent analysis, the intensities ($I_{b\,ref}$ for the reference intensity and I_b for the attenuated intensity of the blue signal) were reported and analyzed.

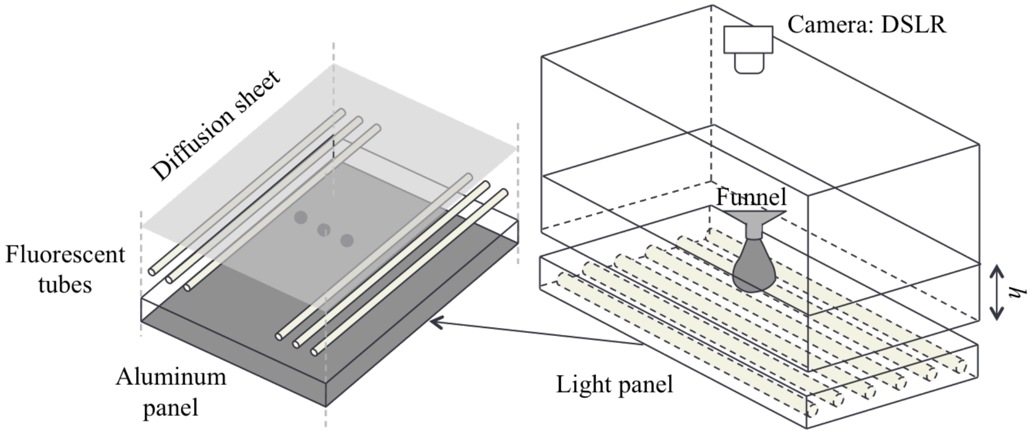

Figure 5.1 Schematic diagram of experimental setup

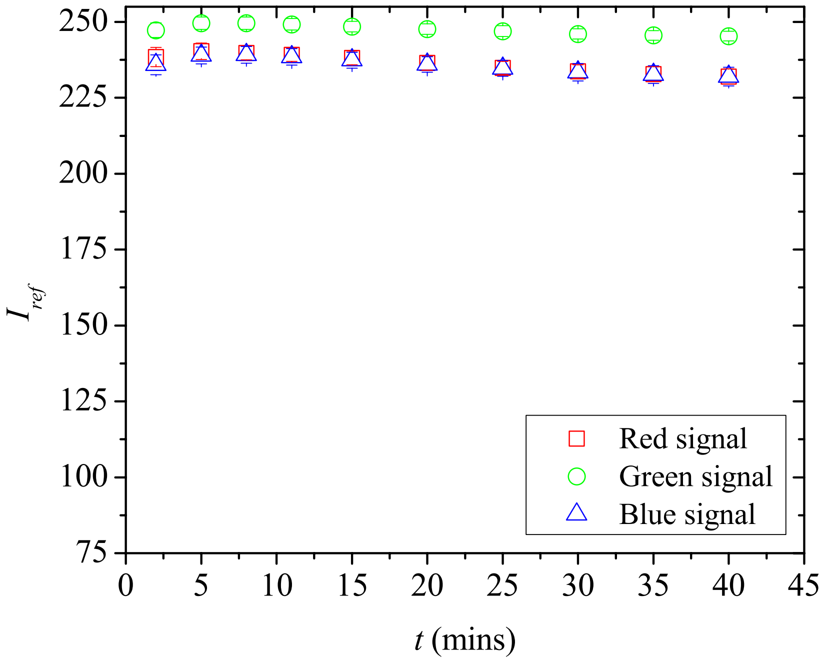

Figure 5.2 Transient variation of light intensity for 3 color signals

Table 5.1 Criteria for the selection of DSLR camera parameters

Parameter	Description & Criteria
Exposure time, t_c	Duration of camera shutter opening to expose the sensor to the light. t_c to be higher than 1/40 to mitigate the flicker issue
ISO Sensitivity	Ability of the sensor to capture light and convert into electrical signals for processing. Lowering the ISO value reduces the noise and hence is preferable for LAM2D
f-stops, f/n	Opening size of the aperture blades, which controls the amount of light entering the camera and affects the depth of field. Large n value is preferable to increase the depth of field
White Balance	Adjustment of the image color to match the real color, so that the color of taken photo matches the color observed visually

5.2.2 Calibration Experiments

The calibration approach established in the new method required two different calibration experiments for the deep and shallow h_s with 2 mm being the critical changeover value. For deep h_s ($h_s > 2$ mm), the traditional scraping technique was used with multiple constant sediment thicknesses. As our water tank was large, scraping the sediments over the entire bottom was impractical. We used instead a set of rings (termed calibration rings) with constant height (2 mm), and scraped the sediment within the rings. Figure 5.3 illustrates the placement of the calibration rings at different locations on the tank floor. Sediment was first poured inside the rings and leveled to a height of 2 mm (= h_s), then the attenuated intensity of $h_s = 2$ mm was taken. Next, the ring height was increased to 4 and 6 mm by stacking up two and three rings, respectively. The attenuated intensities of different h_s were then recorded.

For shallow h_s ($h_s < 2$ mm), the correlation of particle plume deposition profiles from two test types was implemented instead. The two test types were: (i) the depth distribution profile (h_s vs. r_m, where r_m is the radius measured from the center of the profile) obtained from manual collection experiments (Test MCs), and (ii) the attenuated intensity profile (I vs. r_m) measured from the light attenuation experiments (Test LAs). In each case, the deposition profiles were generated by releasing a certain amount of particles from a funnel with a round opening. After the release from the opening, the gravity-driven particle plume descended through the water column and expanded in lateral size due to entrainment. Upon impact on the bottom, the particle plume spread horizontally as a gravity current before depositing. The dynamics of descent and deposition of the particle plumes were similar to the sediment clouds from barge disposal and hence gave an additional motivation for this calibration in our study.

Note that the same sediment profile could not be used for the two test types (i.e. Tests MCs and LAs). This was because Test MCs required grids to be printed on the platform/tank to guide the quantification process, while Test LAs required the sediment to be deposited on a tank clear from marking for better illumination and measurement. Two important criteria were needed for the generated profiles for calibration: (i) consistent and high repeatability, and (ii) axisymmetric, so that the depth distribution can be presented as an azimuthal mean depth profile for analysis to reduce the local variation. Finally, the calibration curve was determined by correlating the results from these two test types.

Four calibration tests with a total 15 replicates were conducted by adopting the same release conditions. Table 5.2 summarizes the test conditions. In Test MCs, the sediments were manually collected, dried and weighted to determine the depth distribution profile. On the other hand, Test LAs measured the attenuated intensity profiles with the light panel. The two replicates from Test LA2 were used to demonstrate the improvement with the current approach. In the following section, the apparatus and test conditions of the particle plume deposition experiments will be discussed in detail.

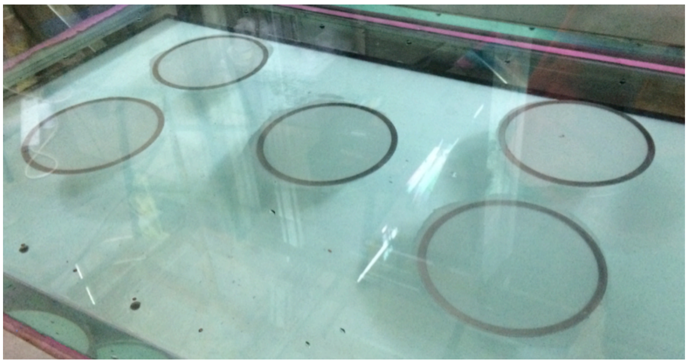

Figure 5.3 Calibration rings

Table 5.2 Experimental conditions for particle plume deposition test

Test	Mass per release [g]	Replicates	Releases	Remarks
MC1	10	3	3	-
MC2	10	5	5	-
LA1	10	5	5	R1 & R2 – day 1 R3 & R4 – day 2 R5 – day 3
LA2	10	2	5	For improvement test

5.2.2.1 Particle Plume Experiments

The particle plumes were generated by continuously releasing a mass of 10 g of sediment from the funnel with a small opening diameter of 10 mm. Each test included the cumulative release of either 3 or 5 times to increase the volume of deposited sediment and hence minimize the local variation. In a preliminary study, several alternative release mechanisms were considered, but they were all found to be inadequate. For example, the quasi-instantaneous release of the same mass (i.e. 10 g) of sediment using a latex-sealed tube (Zhao *et al.* 2014) produced highly inconsistent deposition profiles, possible due to the formation of sediment clumps.

The circular grids used in Test MCs are shown in Figure 5.4 (a). The 10 cm water depth was measured from the platform to the water surface. After 3 or 5 releases, the water was slowly drained out from the tank to keep the deposition profiles undisturbed. The sediment layer was then left over night until the excess water was evaporated. Subsequently, the platform was removed from the glass tank, and the sediment deposited within the same circular grid interval was collected, dried and weighted. The mass distribution (m_s vs. r_m, where m_s is the mass of sediment) was converted to depth distribution (h_s vs. r_m) using the following equation:

$$h_{si} = \frac{V_{si}}{A_i} \text{ with } V_{si} = \frac{m_{si}}{\rho_s(1-n)} \tag{5.4}$$

where the subscript i represents the i-th ring from the center of the circular grid (release point), V_{si} is the volume of sediment, A_i is the area of ring, and n is the void ratio which was assumed to be a constant n = 0.44 based on our previous study (Zhao *et al.* 2012).

In Test LAs, before releasing the sediment, the reference intensity, I_{ref} was measured for each replicate to check for consistency and then used for the normalization of I. Afterward, particle plumes with the same release conditions as Test MCs were released and deposited directly on the bottom of the glass tank. After 5 releases, the attenuated intensity profile using the light panel, I vs. r_m (Figure 5.4 (b)), was determined.

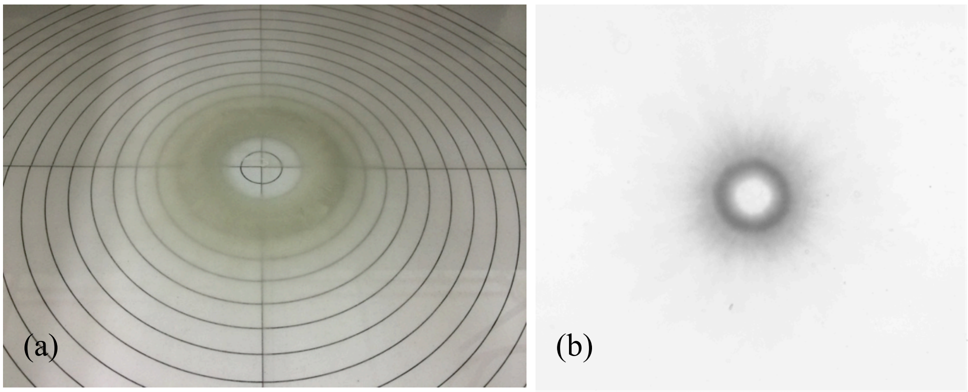

Figure 5.4 Deposition of particle plume from 5 releases (a) on a 10 mm grid space circular grid platform, and (b) in water tank using backlighting with light panel

5.3 Results and Discussions

In this section, the sediment depth distribution and attenuated intensity profiles of the deposition of particle plumes are discussed. The comparative results are then used to establish the calibration curves for both regimes. Improvements compared to the previous approach (using scraper method only) are also shown.

5.3.1 Particle Plume Deposition Profiles

The radial distribution of the mean depth profiles from Test MC2 are plotted in Figure 5.5, with r_m = 0 being the center of the funnel. Only 3 profiles are presented for brevity. When the experiment was initiated, the sediment particles were observed to descend continuously from the opening with a ‘thermal-like’ front head. The particle cloud had a typical tadpole shape, similar to the buoyant starting plume observed by Ai *et al.* (2006). Upon impact with the bottom, the momentum of the ‘thermal-like’ front head and the density difference (buoyancy) drove the collapsed plume to propagate radially as gravity current. The sediment particles then gradually settled out from the gravity current as it propagating away from the release point. With the current test conditions, ~ 35 % of the particle deposited in the area within $r_m < 4$ cm and ~ 60 % deposited outside the ring area with $r_m > 4$ cm. The remaining particle (< 5 %) propagated and settled outside the test region (i.e. $r_m > 18$ cm). By comparing the profiles in Figure 5.5, the variation among the replicates was found to be very small, which was attributed to the careful handling which minimized the human errors during the measurement process and the randomness in releases.

Figure 5.6 illustrates the attenuated intensity profiles from Test LA1 normalized by the reference intensity, $I_{b\ ref}$. In contrast, Munro and Dalziel (2005) normalized I (p,q) by I_{ref} (p,q) recorded at the beginning of each test, where p and q denote the row and column vectors of the pixel matrix. The pixel-by-pixel normalization could be achieved only when the camera and tank were stationary from pre- to post-tests. In the current experimental setup, the camera had to be moved for the installation of the funnel or the model barge. Hence, the pixels were not exactly aligned in the images between pre- and post-tests. In this case, the normalization had to be done with a mean intensity produced by a uniform light sheet. From Figure 5.6, it is noted that the attenuation profile had a similar distribution pattern as the sediment depth profile measured from Test MC2 (Figure 5.5). The variation among the replicates was insignificant as shown from the plotted error bars.

Five cumulative releases were conducted for each replicate in Test LA1 to increase the amount of data for the correlation (see the following section). However, we were concerned that the profiles from 5 cumulative releases might be too high and would collapse or change in shape during the manual collection, which might cause variations in the profiles measured from Tests MC2 and LA1. A preliminary study was therefore performed by conducting tests with 3 and 5 cumulative releases (Tests MC1 and MC2, respectively), and averaging the profiles to a single release (Figure 5.7). Based on the figure, the difference between the two tests was minimal which proved that the profiles from Tests MC2 and LA1 were identical.

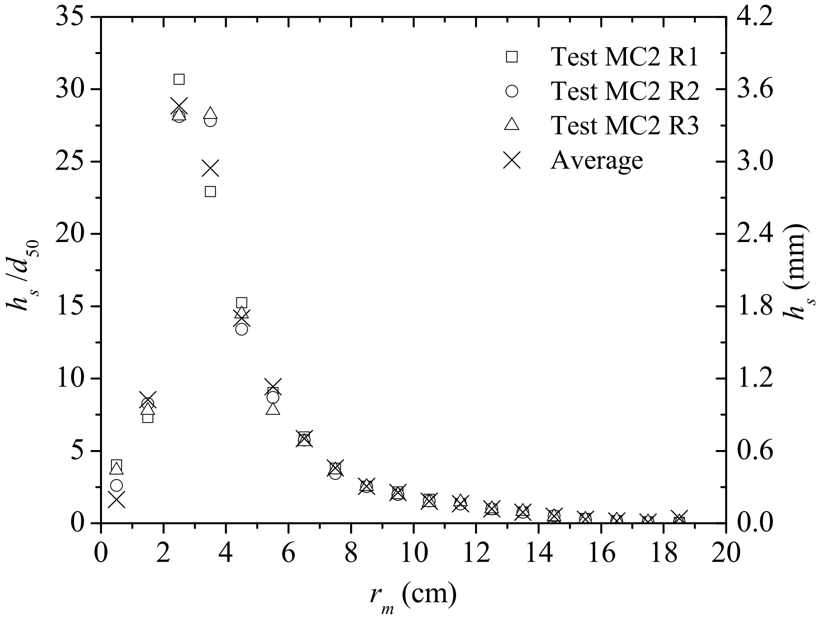

Figure 5.5 Relationship between sediment thickness, h_s/d_{50} and radius, r_m for 3 replicates from Test MC2 (symbols) and averaged value (cross)

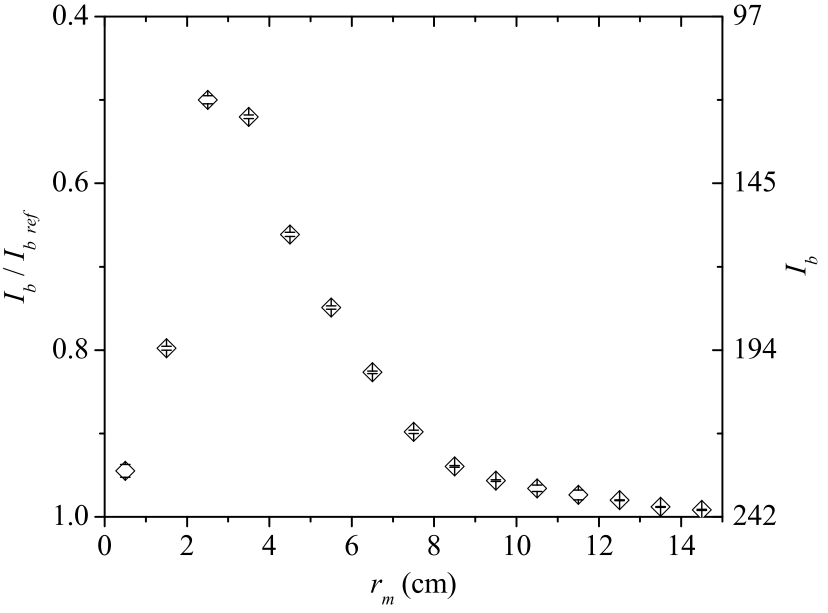

Figure 5.6 Relationship between attenuated intensity, $I_b/I_{b\ ref}$ and radius, r_m

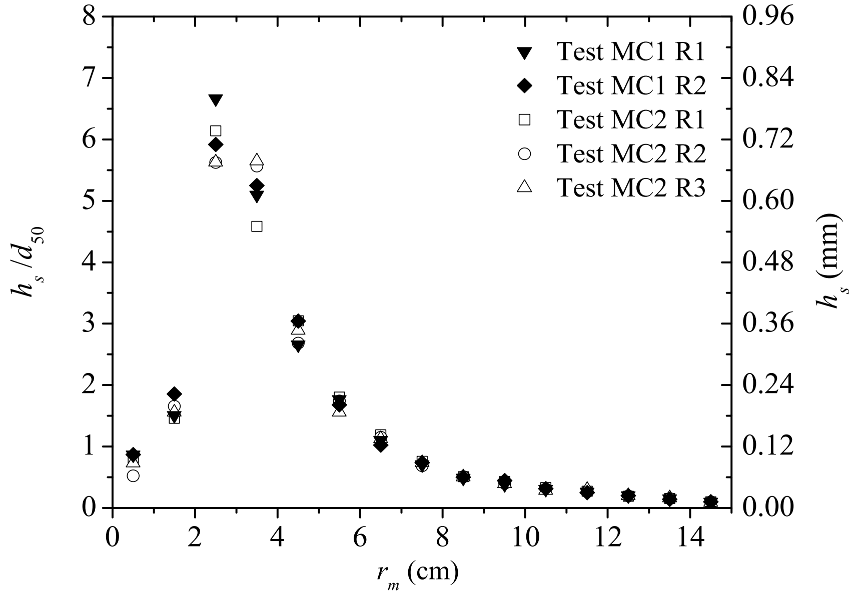

Figure 5.7 Results from Tests MC1 and MC2 after averaged to single release

5.3.2 Calibration Curves

A piece-wise continuous calibration curve was established for the current approach and presented in Figure 5.8, with the solid and dashed lines representing the curve in near-zero limit and self-similar regimes, respectively. A break in the curve at $h_s/d_{50} = 16.7$ can be identified which agrees well with the critical h_s/d_{50} ($h_c/d_{50} = 18$) found by Munro and Dalziel (2005) using the scraper method. It could be argued that the agreement is coincidental because, for our chosen $d_{50} = 0.12$ mm, the break point at $h_s/d_{50} = 16.7$ occurs at a value of $h_s = 2$ mm which is also the dividing line between where we used the scraper method as opposed to the sediment deposition method to prepare profiles. To verify that the critical value of h_s/d_{50} was associated with light attenuation and not the method of profile generation, we carried out several supplemental tests using larger values of $d_{50} = 0.25$ mm (same as Munro and Dalziel, 2005) and 0.51 mm (test conditions summarized in Table 5.3). The results are shown in Figure 5.9 and again the break in calibration curves occurred at $h_s/d_{50} \sim 18$ (vertical dotted line), which was close to the h_c/d_{50} discussed above. Hence, the results strongly suggest that the break in the calibration curve was due to the physics of light transmission rather than the profile generation method.

From Figure 5.8, in the self-similar regime, the data (close markers) were measured from the calibration rings (scraper method) with 3 or 5 replicates. As expected, the attenuation followed the Beer-Lambert's law and experienced an exponential decay with the following equation:

$$\frac{I_b}{I_{b\ ref}} = c\exp\left\{-k_1\left(\frac{h_s}{d_{50}}\right)\right\} \tag{5.5}$$

where c and k_1 are determined to be 0.966 and 0.027, respectively from the least-square fit.

In the near zero limit regime, the data (open markers) were determined by correlating the two profiles discussed in the previous section (i.e. h_s/d_{50} vs. r_m and $I_b/I_{b\ ref}$ vs. r_m → $I_b/I_{b\ ref}$ vs. h_s/d_{50}). Here, we identified two regions in the depth distribution profile (h_s/d_{50} vs. r_m): (i) the region with $h_s < d_{50}$, within which the area was not fully covered by the sediment particles and (ii) $r_m < 4$ cm, where h_s measured from Test MC2 was highly dependent on the size of the ring area, A, and the uncertainty increased for small A. Figure 5.8 suggests that the attenuation is linearly proportional to h_s/d_{50}, and can be expressed as

$$\frac{I_b}{I_{b\ ref}} = a + b\left(\frac{h_s}{d_{50}}\right) \tag{5.6}$$

where a (= 1) is constrained to $I/I_{ref} = 1$ at $h_s/d_{50} = 0$ and b was determined to be -0.023 from the least square fit.

Table 5.3 Experimental conditions for supplemental tests

Test	d_{50} (mm)	h_s (mm)	Range of h_s/d_{50}
ET1	0.25	2, 4, 6, 8, 10, 14, 20	8 – 80
ET2	0.51	2, 4, 6, 8, 10, 14, 20, 26, 40	4 – 78

Note: The number of replicates differed among h_s (varied from 1 to 3), with thicker h_s had lesser replicates as the variation reduced when h_s increased based on experimental observation

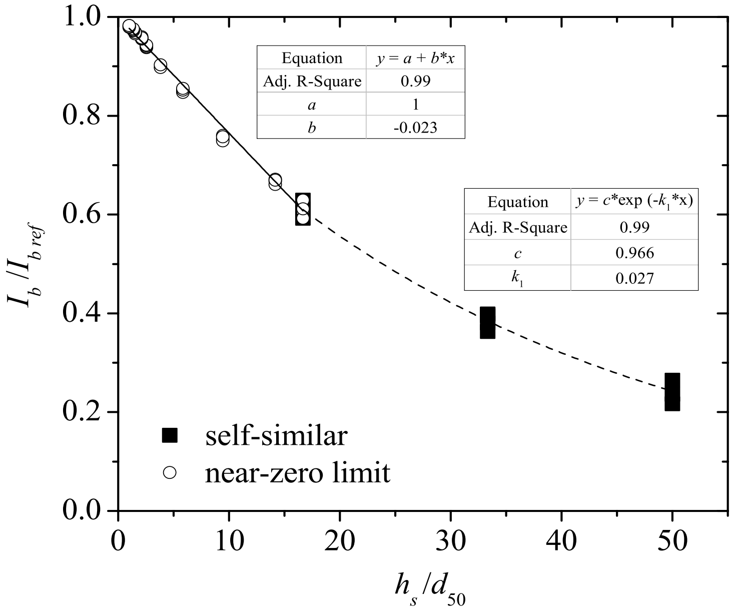

Figure 5.8 Overall calibration curve

5.3.2.1 Improvement over Previous Approach

As discussed earlier, in the previous approach, the curve was established from the scraper method and fitted with

$$\frac{I_b}{I_{b\,ref}} = \exp\left\{ -k_2 \left(\frac{h_s}{d_{50}} \right)^{\gamma} \right\} \tag{5.7}$$

constraining to $I_b/I_{b\,ref} = 1$ at $h_s/d_{50} = 0$ and $I_b/I_{b\,ref} \rightarrow 0$ when $h_s/d_{50} \rightarrow \infty$ (Munro and Dalziel 2005), with $k_2 = 0.029$ and $\gamma = 1$ obtained from the collected data.

Figure 5.10 compares the calibration curves in the near-zero limit regime established from current (solid line) and previous (dashed line) approaches. The improvement in the measurements of h_s/d_{50} with the present approach was primarily within the range of 0 to 1. To illustrate the significance of this difference, the profiles from Test LA2 (Figure 5.11) were computed (inverse-calibrated) with the present and previous approaches (curves in the self-similar regime were identical since they were both derived from the same set of data). Subsequently, the mass conservation error at i^{th} ring, ε_i, which was defined as the integrated mass recovered divided by the mass collected at i^{th} ring (from Test MC2), was examined. The absolute errors, $|\varepsilon_i|$ of the sediment masses computed with current (open) and previous (solid) approaches are illustrated in Figure 5.12. The plus sign (+) on the column represents $\varepsilon_i > 0$, and without sign represents $\varepsilon_i < 0$. It can be seen that the errors from the current approach were generally smaller. The total mass conversation errors, ε_t, which was defined as the integrated mass recovered divided by the total mass released, were – 12% and – 3% with the previous and current approaches, respectively. Note that the deposition profiles here had a total area, A_{total} of only around 530 cm^2, which was very small compared to the deposition profiles from actual barged sediments disposal. The errors are expected to increase with A_{total} and will be discussed in the following section.

5.3.2.2 Validation

The improvement in the present approach is primarily due to the calibration of shallow sediment thicknesses in a more accurate manner. The key is in the generation of the deposition profiles reliably in every replicate with the same test conditions. Validation was thus an important step in this study to ensure the applicability of this technique. In other words, we checked the consistency on the deposited profile in every replicate as well as the attenuated intensity profile.

Validation is essential to judge the quality, reliability and consistency of the developed method (Huber 2010). The evaluation parameters differ among various fields, and a comprehensive list was summarized by Van Zoonen *et al.* (1999) and Huber (2010). The validation of the current approach focused on the parameters listed in Table 5.4. To test the precisions (both repeatability and intermediate precision), 5 replicates were conducted in Test LA1 over different days as noted in Table 5.2. The attenuation profiles of 4 out of 5 replicates from Test LA1 were reported in Figure 5.13. The results showed that no significant deviation was observed in the same day (either day 1 or day 2). By comparing the profiles between R1 and R2 as well as R3 and R4, the consistency and repeatability also remained the same over multiple days.

Besides repeatability, three dispersion characteristics of the calibration curves were also suggested in the literature to be examined (Currie 1999): (i) the critical limit (L_C), (ii) the detection limit (L_D, with the associated detection thickness, h_{sD}/d_{50}), and (iii) the quantification limit (L_Q) as described in Table 5.4. However, in the current study, only the first two were analyzed due to the fact that L_Q had multiple definitions as defined in the literature. We reviewed the definitions and found that L_Q was more important for the chemical measurement process (CMP). Furthermore, in LAM2D, L_C and L_D (h_{sD}/d_{50}) are sufficient to examine the reliability of the calibration curves.

L_C was determined as the $I_b/I_{b\ ref}$ above without sediment particles. The numerical value of L_C can be either calculated from equations or determined from graphs (Currie 1999, Lavagnini and Magno 2007, Shrivastava and Gupta 2011) as illustrated in Figure 5.14. The prediction bounds of the calibration curve are plotted based on $\alpha = 0.5$ (95 % confidence interval), and $L_C = 0.979$ (critical thickness, $h_{sC}/d_{50} = 0.871$) was obtained from the intersection of the lower bound with the y-axis. This value ($L_C = 0.979$) was higher than $I_b/I_{b\ ref} = 0.976$ at $h_s/d_{50} = 1$, which also implied that the condition of $h_s/d_{50} = 0$ when $I_b/I_{b\ ref} > 0.976$ set during the computation (inverse-calibration) was appropriate.

The detection thickness, h_{sD}/d_{50} (= 1.712) was calculated as the abscissa of the intersection of the line $I_b/I_{b\ ref} = L_C$ with the upper bound. This implies that the calibration curve was capable of detecting sediment thicknesses down to ~ 1.7 times the particle size. The above validation of LAM2D has yet to be reported in the literature. We recommended doing so to ensure the quality of the calibration curves prior to actual application.

Table 5.4 Parameters of method validations for the proposed method

Parameter	Description
Precision – Repeatability	The precision under the same conditions over a short interval of time (within a day)
Precision – Intermediate Precision	The precision over different days or with different equipment
Critical Limit – L_C	The attenuated intensity below which a response is reliably attributed to the presence of particles
Detection Thickness – h_{sD}/d_{50}	The lowest sediment thickness that can be detected

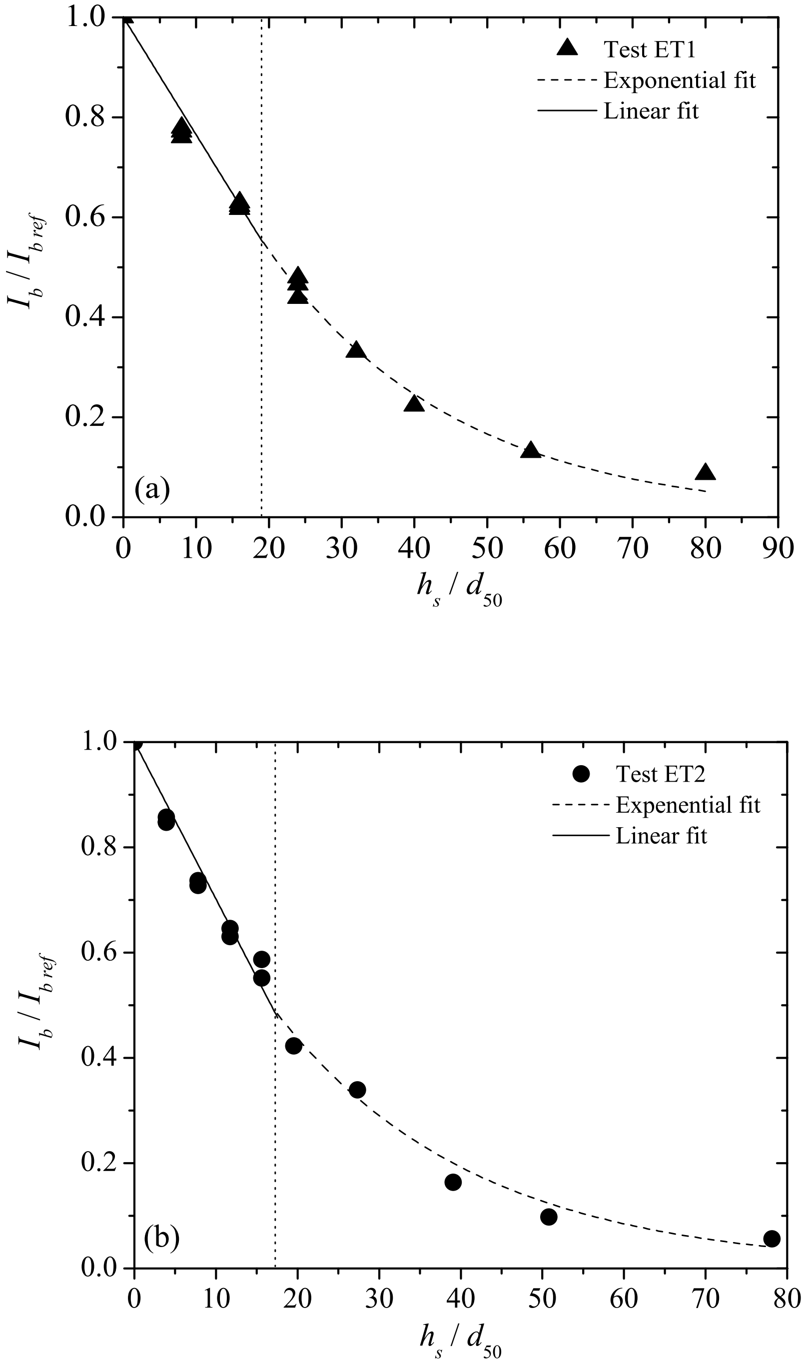

Figure 5.9 Calibration curves from Tests (a) ET1 and (b) ET2. Note that, for smaller values of h_s/d_{50} up to three replicates were conducted in anticipation of greater experimental variability in measurements at small h_s.

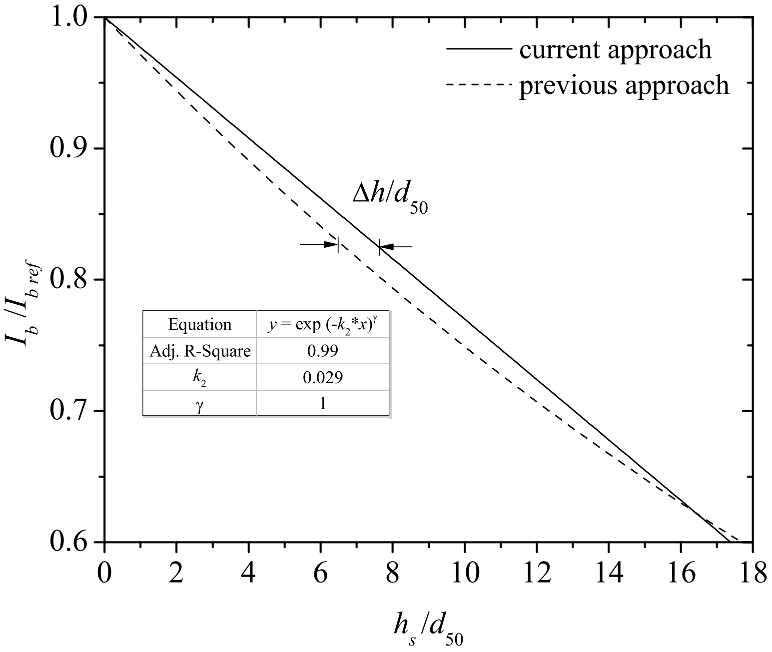

Figure 5.10 Comparison of calibration curves in near-zero limit regime from current and previous approaches

Figure 5.11 Two particle plume deposition profiles from Test LA2

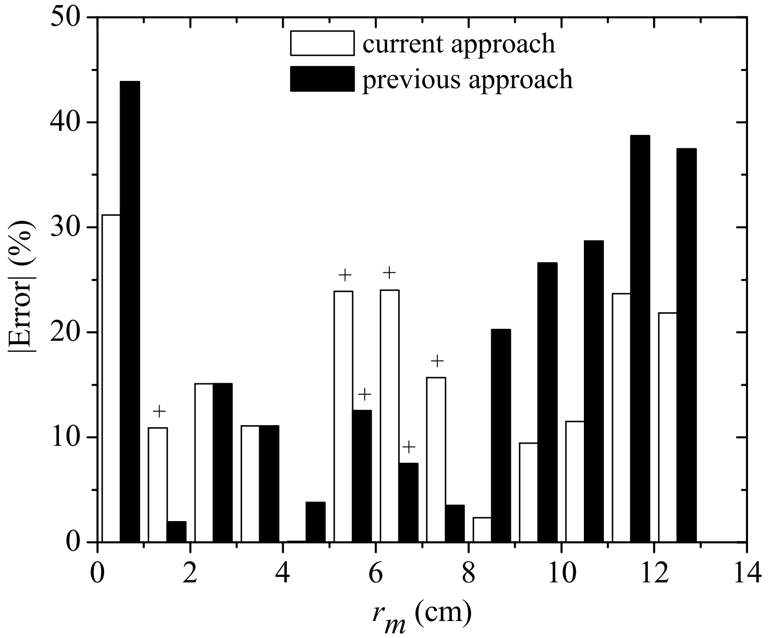

Figure 5.12 Absolute errors of conservation mass, $|\varepsilon_i|$ from current and previous approaches with the measurement from Test MC2. Columns with plus sign '+' represent $\varepsilon_i > 0$ and without sign $\varepsilon_i < 0$

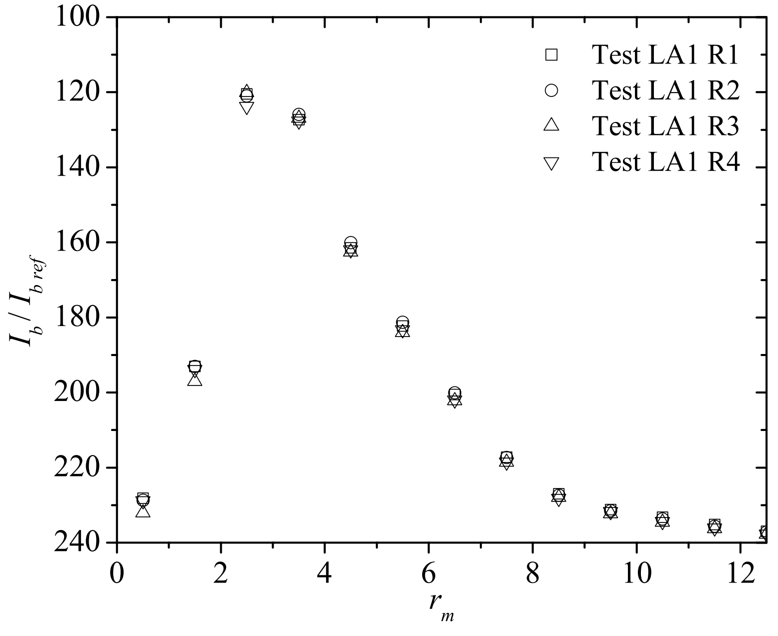

Figure 5.13 Precision tests - comparison of attenuation profiles from particle plume depositions conducted on different days

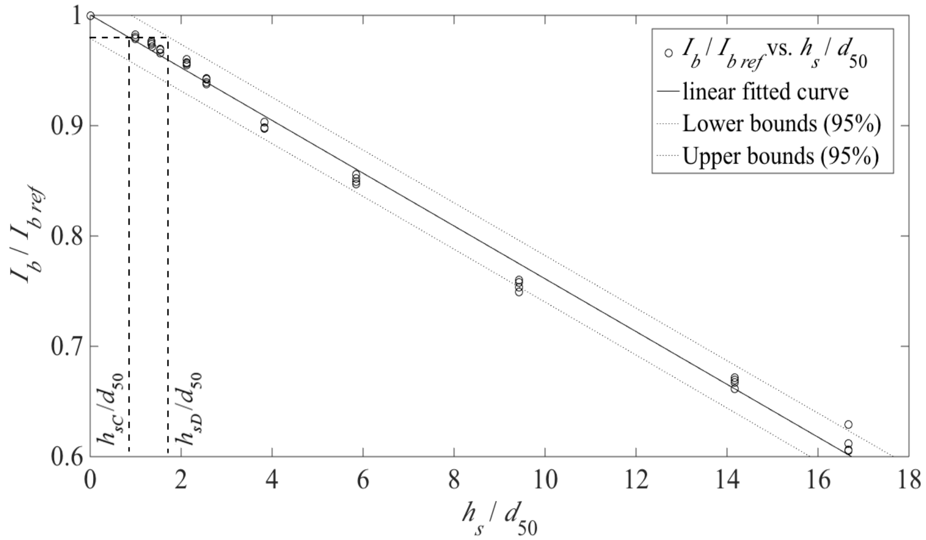

Figure 5.14 Prediction (solid line, bounded by confidence interval, $\alpha = 5\%$) in the near-zero limit regime. The two vertical dashed lines show the critical and detection thicknesses (critical thickness from L_C: $h_{sC}/d_{50} = 0.87$, detection thickness from L_D: $h_{sD}/d_{50} = 1.71$) respectively.

5.4 Application – Deposition of Barged Sediment Disposal

Activities such as dredging (with associated dredged material management) and land reclamation often involve open water sediment disposal. A barge is commonly used to transport and dispose the sediments due to its large carrying capacity. From field observations, Bokuniewicz *et al.* (1978) identified three phases of the sediment transport upon release: (i) convective descent phase, during which the flow behavior is dominated by the disposal conditions and driven by gravity, (ii) dynamic collapse phase, during which the sediments impact the seabed and begin to spread horizontally, and (iii) passive-transport dispersion phase, when the sediments are passively carried by the ambient currents and turbulence.

In the present study, the laboratory investigation of barged sediment disposal was conducted in the same glass tank, and the water depth was also identical (h = 10 cm) to the calibration tests. A model barge (shown in Figure 5.15, made with two rectangular acrylic boxes) was designed from an actual barge scaled down with dimensions of 20 cm (length, L) × 4 cm (width, W_b) × 4 cm (depth, D_b). To initiate an experiment, the two rectangular boxes would rotate in opposite directions with an angular speed, ω, forming an opening (opening width, W) in the middle through which the sediment was released. The attenuated intensity profiles of the deposited sediment thicknesses from each release of a defined mass of 112 g of sediment particles (Ballotini Impact beads, d_{50} = 0.12 mm) were then taken after every release, up to a maximum of 5 releases.

Upon release, the sediment cloud would descend through the water column and grow in lateral size due to entrainment. Upon impact with the bottom, gravity currents would be initiated by the cloud buoyancy to propagate horizontally. In contrast to the deposition from a funnel with an axisymmetric round opening, the rectangular opening of the model barge created a different deposition pattern. Based on the BSDM calculations with the present release parameters, the flow regime of the sediment cloud before impact was predicted to be in the two-dimensional starting plume regime, with transverse entrainment dominating the growth of the sediment cloud. Hence, the deposition profiles grew mainly in the transverse direction as an ellipse with the major axis parallel to the transverse axis (Figure 5.16).

Figure 5.16 illustrates the contour plots of sediment thicknesses determined from current and previous approaches for the accumulation of 5 releases, through an opening width, W of 4 cm. In the figure, the rectangular boxes in the center represent the location of the model barge, and the numerical values on the contour denote h_s (in mm). The results showed that both approaches were able to capture the deposition pattern with high accuracy. However, the total mass conservation error, ε_t, with the current approach ($\varepsilon_{t\,cur} = -$ 12.5 %) was significantly less than that of the previous approach ($\varepsilon_{t\ pre} = -$ 20.0 %). We note that, in general, the mass conservation error would be negative because some particles inevitably fell outside the domain. The reduction in error can be directly attributed to the improved calibration curves in the near zero-limit regime as illustrated in Figure 5.10.

The reasons for multiple releases instead of a single release were to reduce the local variation and increase the value of h_s in the self-similar regime. However, in some experiments, for example the sedimentation of particles from buoyant plumes in a stratified ambient (Wang and Adams 2015), multiple releases are not feasible. Nevertheless, we noted that the current approach significantly improved the measurements even with a single release profile, as the mass conservation error of single released profile with $L/W = 24$ reduced from $\varepsilon_{t\,pre} = -17.4$ % to $\varepsilon_{t\,cur} = -1.9$ % (not shown) compared to the previous approach.

5.5 Summary and Conclusions

An improved LAM2D method was developed in this study using a CMOS camera and analyzed with the blue signal. The approach method used different calibration techniques for the two range of deep and shallow sediment thicknesses, with the traditional scraper method and the correlation of particle plume deposition profiles (depth distribution and attenuated intensity profiles), respectively. The calibration curve for each was established with data only in the respective range to better represent the attenuation behavior. Verification experiments showed that the improved method produced high repeatability and consistency in the determination of sediment depth profiles, and reduced the mass conservation error significantly compared with the previous approach with calibration based only on the scraper method.

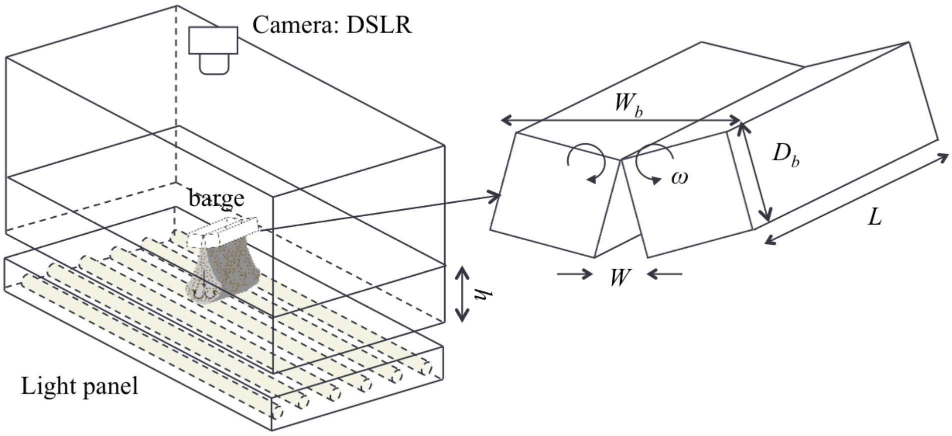

Figure 5.15 Schematic diagram of model barge

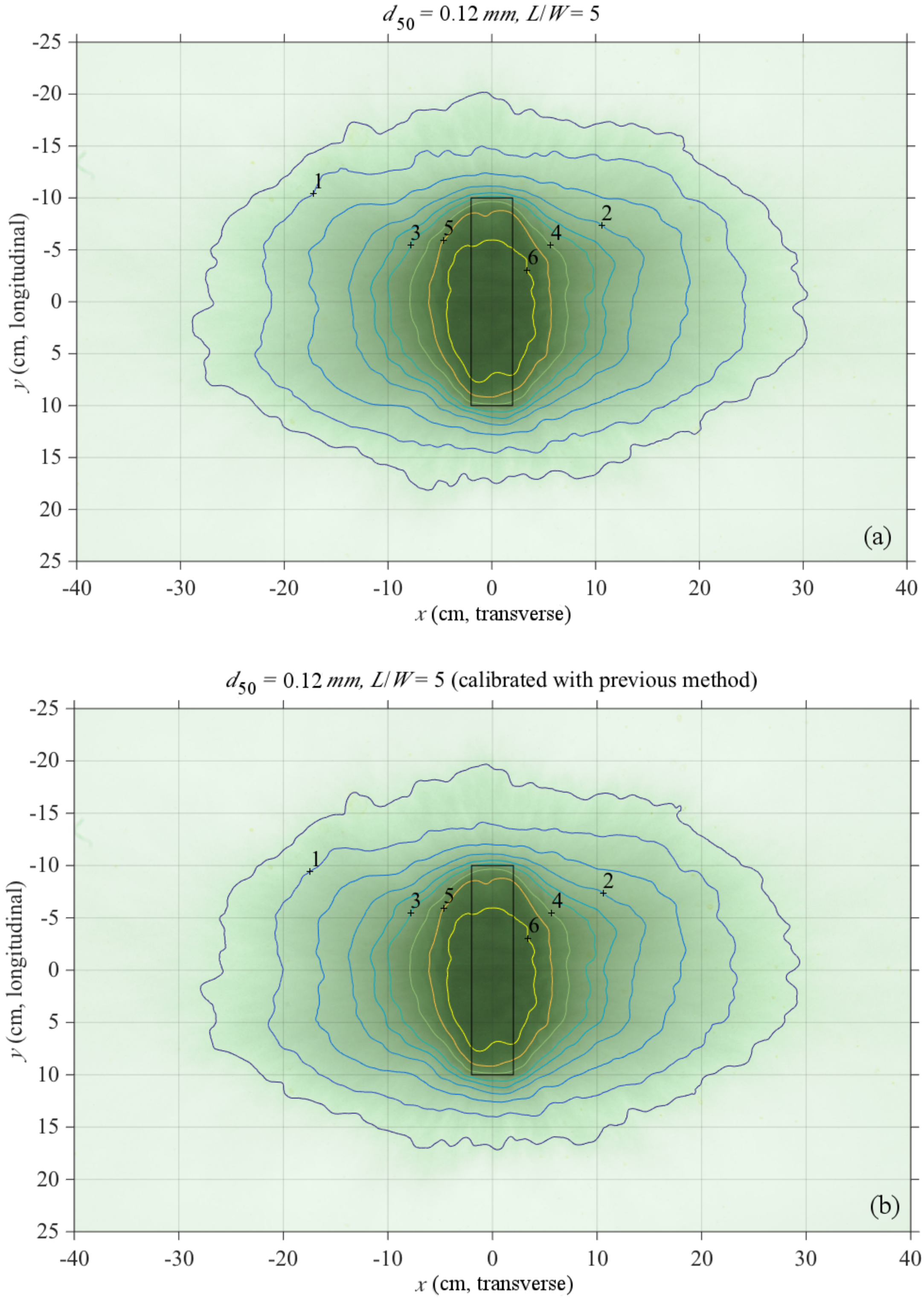

Figure 5.16 Deposition profiles from barged sediment disposal (d_{50} = 0.12mm, L/W =5): (a) current and (b) previous approaches

Chapter 6

Gravity Currents due to Barged Sediment Disposal

6.1 Introduction

So far, the behavior of sediment clouds due to barge disposal in the convective descent phase has been discussed. The current chapter further examines the dynamics of barge-disposed sediments in the bottom collapse phase, which upon impact the momentum and buoyancy of the sediment cloud drive the collapsed cloud to propagate along the seabed as a gravity current. Practically, the bottom collapse phase poses greater threat to the environment, as the spreading of gravity current governs the zone of sediment deposits and may promote the dispersion of contaminants.

In the literature, STFATE (Johnson and Fong 1995) modeled the collapsed cloud as a half-ellipsoid, with the a_c, b_c, and c_c represent the size of the collapsed cloud in x, y, and z directions, respectively as illustrated in Figure 6.1. The evolution of the collapsed cloud is computed from the concept of energy conservation, which can be expressed as:

$$\Delta E_K + \Delta E_P = E_W \tag{6.1}$$

where E_K and E_P represent the kinetic and potential energy carried by the collapsed cloud, respectively. E_W is the work done by the collapsed cloud (or loss of energy) to overcome the bottom friction, bottom drag and production of internal turbulence.

Note: The material presented in this chapter has been prepared to be submitted for the consideration of publication

The equations for these three components are given in Johnson and Fong (1995).

In the model, the potential energy, E_P due to the mass of cloud and its centroid position (at level above seabed) is the force that drives the collapsed cloud to spread horizontally. The expression for E_P can be written as:

$$E_P = \iiint_{A_c h} \rho_a g z dV_T + \Delta\rho g \iiint_{A_c c} z dV_c \tag{6.2}$$

where A_c is the area of seabed, V_T is the total volume of the ambient water, A_c and V_c are the bottom cross-sectional area and volume of the collapsed cloud, respectively. The first term on the right hand side represents the hydrostatic pressure induced by the ambient water, and equals to constant for stagnant water surface. The last term illustrates the hydrodynamic pressure of the collapsed cloud, which may vary with time due to the conversion to E_K and E_W, in order to spread the collapsed cloud horizontally and also overcome the frictions. By integrating Equation (6.2), the change of E_P can be expressed as:

$$\Delta E_P = \Delta\left(\frac{3}{8}\Delta\rho g V_c c\right) \tag{6.3}$$

Subsequently, the evolution of the collapsed cloud can be evaluated by using the general equation of an ellipsoid and the kinetic energy of the collapsing cloud:

$$E_K = \iiint_{V_c} \frac{1}{2}\rho\left(u_c^{\ 2} + v_c^{\ 2} + w_c^{\ 2}\right) dV_c \tag{6.4}$$

where u_c, v_c and w_c are the propagation speeds in x, y and z directions, respectively. In the model, the spreading of the collapsed cloud can be determined by solving Equation (6.4) numerically together with Equations (6.1) and (6.3). The integration and computation steps were presented in Johnson and Fong (1995).

The development of collapsed cloud in STFATE was modeled in the manner of an individual cloud without constant supply of sediments, and release from a point source. However, this simplification may not be accurate in the event of shallow water and large volume disposal. Based on the classification scheme in BSDM, the sediment cloud may experience starting plume regimes upon impact, and the collapsed cloud is being supplied with constant sediment flux when propagating downstream (away from source) until the sediments are fully discharged from the barge. In the present study, the dynamics of the collapsed clouds are modeled as particle-laden gravity currents, with the motion is mainly driven by the buoyancy force due to the density difference between currents and ambient fluid.

The investigation on particle-laden gravity currents had drawn much attention as they commonly occurred in natural phenomena, such as snow avalanches, lava flows, dust storm and so on. Unlike homogeneous (single-phase) gravity currents, the particles will settle out as the currents propagate downstream, hence reducing their buoyancy force. In terms of the development process, particle-laden gravity currents only experience slumping and inertial phases (Bonnecaze *et al.* 1993, Dade and Huppert 1995), as the particles are fully settled before they enter the viscous phase. In the following, 'particle-laden gravity current' is stated as 'gravity current' or 'current' for simplification.

For the analysis of gravity currents, Shallow-Water equations and Box-Models are the two most common approaches. Shallow-Water equations are capable of modeling the variation of parameters (e.g. particle concentration, density field) within the current and also simulating multi-layer fluids. Box-Models was first introduced by Huppert and Simpson (1980), by assuming the currents evolved as a series of equal-area rectangles (two-dimensional current) or equal-volume cylinders (axis-symmetric current), as illustrated in Figure 6.2. Despite their simplicity and the issues raised by Ungarish and Zemach (2005), Box-Models are still widely used, especially for quick prediction or when dealing with non-axisymmetric gravity currents (Gladstone and Woods 2000, Zgheib *et al.* 2015).

The studies of gravity currents were generally carried out in either a fixed volume or constant flux (continuous release of buoyant fluids) manner. However, due to the large and finite amount of sediment involved during barge disposal, the sediments are continuously released as a sediment plume (constant flux) before transiting to a discrete sediment thermal after being fully discharged (fixed volume). This transition significantly affects the dynamics of gravity current, which has not been addressed so far. The objective of this study is to develop a modified Box-Model that includes this transition, to better represent the realistic condition.

Besides, barges typically have a rectangular bottom opening instead of the usual canonical configurations (i.e. planar or circular). The volume discretization approach proposed by Zgheib (2015) is utilized to capture the dependence on the barge opening shape (non-canonical shape). The model predictions are then verified with an experimental study. In the following, the modified Box-Model is first presented. The model predictions are then compared to the experimental results for assessment.

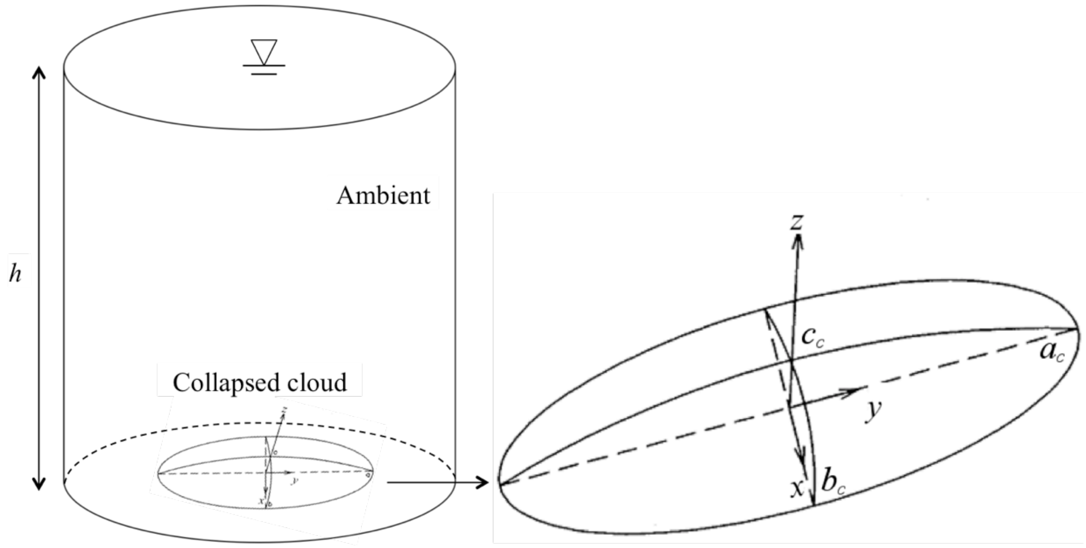

Figure 6.1 Simulation of collapsed cloud in STFATE

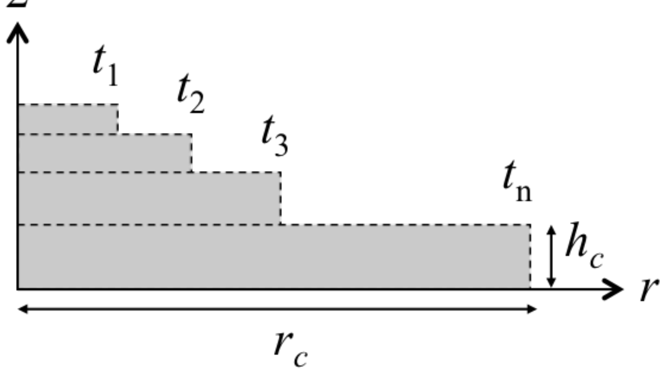

Figure 6.2 Schematic description of three-dimensional Box-Model at different time instances (t_1, t_2, t_3, … t_n)

6.2 Modified Box-Model

The Box-Model for three-dimensional gravity currents consists of three main equations, which are presented below as Equations (6.5): the conservation of volume, (6.6): a Froude number condition at the current head, and (6.7): the law of sedimentation.

$$V_c = \pi r_o^2 h_\mathrm{o} = \pi r_c^2 h_c \tag{6.5}$$

$$u_c = \mathrm{d}r_c/\mathrm{d}t = \mathrm{Fr}\ (g'\varphi h_c)^{1/2} \tag{6.6}$$

$$\frac{\mathrm{d}V_c\varphi}{\mathrm{d}t} = -\ w_s\varphi\pi\ r_c{}^2 \tag{6.7}$$

where V_c is the volume of gravity current, h_o and r_o are the initial height and radius of the current, g' is the reduced gravitational acceleration, h_c is the current height, φ is the particle volume fraction and w_s is the particle settling velocity.

To account for the constant flux due to the sediment plume, Equations (6.5) and (6.7) have to be modified respectively:

$$\frac{\mathrm{d}V_\mathrm{c}}{\mathrm{d}t} = u_p r_o L \tag{6.8}$$

$$\frac{\mathrm{d}V_c\varphi}{\mathrm{d}t} = -\ w_s\varphi\pi\ r_c{}^2 + q \tag{6.9}$$

where the right hand side of Equation (6.8) is the volume flux from the plume, u_p and r_o are the plume downward velocity and radius, q is the sediment flux. We normalized the lengths, time, velocities and particle volume fraction by h_o (= 0.72 r_o), $(h_o/g_o')^{1/2}$, $(h_o g_o')^{1/2}$ and φ_o, where φ_o is the initial volume fraction. Note that, h_o, g_o', φ_o, r_o, u_p, and q are computed from BSDM discussed in Chapter 4. Using uppercase symbols or current symbols with a subscript '*m*' to represent the dimensionless variables (e.g. $V_n = V_c/h_o^3$), the normalized governing equations can be expressed as:

$$\frac{\mathrm{d}V_m}{\mathrm{d}T} = U_p R_o L_m \tag{6.10}$$

$$\frac{\mathrm{d}\Phi}{\mathrm{d}T} = -\frac{\beta\Phi}{H_c} + \frac{Q}{V_m} - \frac{\Phi U_p R_o L_m}{V_m} \tag{6.11}$$

$$U_c = \frac{\mathrm{d}R_c}{\mathrm{d}T} = \mathrm{Fr}\, H_c^{1/2}\Phi^{1/2} \tag{6.12}$$

where β [$= w_s/(g_o{'}h_o)^{1/2}$] is the settling number or normalized particle settling velocity, L_m ($= L/h_o$) is the normalized disposal bin length and Φ ($= \phi/\phi_o$) is the normalized volume fraction.

Equation (6.11) explains the elements that affect the sediment concentration in the gravity current. The first term on the right hand side represents the instantaneous loss of sediment through deposition onto the seabed within the current length. The final deposition profile can be computed from this term, by summing up the amount of sediments, V_s deposited at each time step. The detailed description will be discussed in the subsequent sub-section. The second and third terms show the impacts of the sediment plume, with the former denoting the increment in sediments due to the sediment flux and the latter denoting that the sediment plume also increases the total area of the gravity current and hence dilutes the sediment concentration at the same time.

Equation (6.12) is an empirical law established by Huppert and Simpson (1980) to account for the complicated three-dimensional dynamics in the current head. Fr is dependent on h_c/h, where h is the water depth, in the following manner: (i) Fr = 1.19 when $h_c/h < 0.075$, and (ii) $\mathrm{Fr} = C_1\,(h_c/h)^{-1/3}$ when $0.075 \leq h_c/h < 1$. The present study is in this latter region. The value of C_1 was found to vary between 0.50 and 0.67 based on different studies (Dade and Huppert 1995, Gladstone and Woods 2000). Here, we noticed that the value of C_1 was affected by the release mechanism of that the buoyant fluids. We calibrated C_1 with the experimental data from Hallworth *et al.* (1998) and Nguyen *et al.* (2012), which had a similar setup as the present study, and found a value of 1.2. The calibration details are presented in Appendix D. The higher C_1 value might be due to the additional initial momentum induced by the sediment cloud upon impact, which was negligible in the 'lock-exchange' release configuration (Huppert and Simpson 1980, Dade and Huppert 1995, Zgheib *et al.* 2015).

To account for the transition from constant flux to constant volume, an extra condition is needed: when $t > t_e$ (t_e is the time for sediments fully discharged from barge), $Q = 0$ and $U_p = 0$. The above equations can be solved using an explicit scheme with small time steps, and with the initial conditions (i.e. h_o, g_o', φ_o, r_o, u_p, and q) determined from BSDM.

6.2.1 Computation of Sediment Deposition

In the literature, there were three main studies that utilized the Box-Model to analyze the propagation of particle-laden gravity currents and the resulting deposition profiles (Hogg *et al.* 2000). Bonnecaze *et al.* (1995) and Dade and Huppert (1995) mathematically solved the law of sedimentation (or conservation of sediment mass) to determine the profile of sediment thickness (i.e. h_s vs. r). On the other hand, Hallworth *et al.* (1998) adopted a more straightforward approach by computing the amount of sediments deposited in every time step and assumed uniform distribution along the current. The final deposition profile was then determined by summing up the profile from each time step.

In the present study, a direct integration of Equation (6.9) was not applicable due to the transition of flow regimes. Hence, the approach presented by Hallworth *et al.* (1998) was used. The sedimentation from gravity current can be computed from the second term of Equation (6.11), which accounts for the sediments that settled out from the current and deposited on the seabed at each time within the current. The volume of the deposited sediments at each time step, Δt can be calculated as:

$$V_s = -\frac{\beta\Phi}{H_c}\left(\varphi_o\sqrt{\frac{g_o'}{h_o}}\right)\cdot\left(\Delta t V_c\right) \tag{6.13}$$

The distribution of sediments along the current is important and depends on the method of releasing the gravity currents. We had tried the assumption of uniform distribution, however the results under-estimated the thickness of sediments near the source, and over-estimated h_s in the downstream regions. Here, we assume that the sediments settle in an exponentially decay manner along the currents and the distribution of sediment at sub-volume, *j* and any time can be expressed as

$$h_s(r,t) = h_{so}\exp(-C_2 r) \tag{6.14}$$

where h_{so} is the sediment thickness at $r = 0$ (source) and C_2 is a coefficient that determined by iteration to ensure the sediment mass is conserved. The rationale of utilizing an exponential distribution was inspired and supported by the experimental observation. After the sediment clouds reached the bottom and formed the gravity currents, the sediments that subsequently released from the barge increasingly tended to settle near the source as time progressed. This might be due to the released sediments especially near t_e, having insufficient momentum to contribute to the gravity currents and thus more likely to settle near the barge. The amount of sediments settled near the source increased with *L/W* (or inversely proportional to barge opening). Hence, h_{so} could then be assumed to behave as:

$$h_{so} = \exp\left(C_3\beta\right) \tag{6.15}$$

where C_3 is a coefficient and can be determined by simulating Bonnecaze *et al.* (1993)'s results. The simulation is presented in Appendix D. The value of C_3 was found to be 8.

6.2.2 Volume Discretization Approach

A direct application of Box-Model to solve the gravity currents with non-canonical shape was attempted by Zgheib (2015) but shown to be unsuccessful. This was due to the Box-Model treating the current as a whole and homogenizing the current properties (i.e. same r_c and h_c throughout the current), hence neglecting any spatial variations. For non-canonical gravity currents, the current properties must be allowed to vary along the edge. With the volume discretization approach discussed in Zgheib (2015), the kinematic relation of each sub-volume can be written as:

$$\frac{\partial x_c}{\partial t} = u_c \frac{-\partial y_c/\partial s}{\sqrt{\left(\partial x_c/\partial s\right)^2 + \left(\partial y_c/\partial s\right)^2}} \tag{6.16}$$

$$\frac{\partial y_c}{\partial t} = u_c \frac{\partial x_c / \partial s}{\sqrt{\left(\partial x_c / \partial s\right)^2 + \left(\partial y_c / \partial s\right)^2}} \tag{6.17}$$

$$\frac{\partial \sigma}{\partial t} = u_c \tag{6.18}$$

The above equations described the evolution of a gravity current front in the x-y plane, where $[x_c\,(s,\,t), y_c\,(s,\,t)]$ denotes the current front (nose) location of each sub-volume, and t and s are independent variables that represent the time since the gravity current formed and distance measured along the circumference of the front, respectively. An additional variable, the area per arc length $[\sigma\,(s,\,t)]$ represents the characteristic length of a sub-volume, and can be calculated by dividing the surface of sub-volume by the corresponding front segment length.

The first step of this approach was to discretize the gravity current (after the sediment cloud fully collapses and ready to propagate downstream) into several equidistant sub-volumes. In the present study, the gravity currents on the both side of the barge were symmetric due to the stagnant ambient, and hence we only discretized and modeled one side in the subsequent analysis. Here, we considered a rounded rectangular shape that best represented the geometry of a barge-disposed sediment cloud as shown in Figure 6.3, and discretized the front using a set of equidistant points with space Δs. Each point had its own coordinate (x_c, y_c) representing location of current front of the respective partitioned sub-volume, within which the flow properties (u_c and h_c) were homogenized.

This approach involved some approximations: (i) the height of current of each sub-volume may vary depending on the local current characteristics; (ii) the velocity of propagation is normal to the front; and (iii) the Fr condition introduced by Huppert and Simpson (1980) can be used to express the front condition. These assumptions were examined with Direct Numerical Simulation (DNS) and found to be acceptable as discussed in Zgheib (2015).

6.2.3 Computational Steps

The computation at each time step consisted of two stages. The first (intermediate) stage involved the Box-Model as expressed in Equations (6.10) to (6.12) being integrated in every sub-volume. At the end of this stage, because of the azimuthal variations, the equidistant points were no longer equaled in distance. The second (remapping) stage involved the re-organization of the points to arrange them in equidistant along the current front. During this stage, the flow properties of the new sub-volume were determined based on the values in the first stage. This is schematically explained in Figure 6.4, with the intermediate stage denoted by an asterisk (*) and t_1 is the initialization of the computation.

At any sub-volume (j), the characteristics of current can be represented as [h_{cj}, σ_j, ϕ_j, V_j] at $t = t_1$, and the propagation is simulated with Equations (6.10) to (6.12) that lead to the intermediate stage.

$$[h_{cj},\sigma_j,\phi_j,V_j]_{\,t=t_1} \xrightarrow{\text{Equations (6.10) - (6.12)}} [u_{cj},h_{cj},\sigma_j,\phi_j,V_j]^*_{\,t=t_1*} \tag{6.19}$$

With the latest u_{cj}^*, the coordinate of the equidistant points in x-y plane can be updated. As mentioned above, the new set of points, $[x_{cj}, y_{cj}]^*$ may not necessarily be equidistant along the current front. To render $[x_{cj}, y_{cj}]^*$ equidistance, we first determined the perimeter of the front by connecting the new points with straight segments. From the ratio of the perimeter to the spacing (Δs), we computed the required number of points at the new time step, t_2. Then, a point was randomly chosen (usually at $x = 0$ and $y > 0$, i.e. the top section of the current) and the subsequent points were marked along the current front with spacing Δs. This set of points formed the new equidistant points at $t = t_2$.

Once the equidistant points were remapped, the new sub-volume corresponded to each point can be determined, bounded by the midpoints between two neighboring equidistant points (Figure 6.5). The second step in the remapping stage was to homogenize the current characteristics within the newly partitioned sub-volumes. As illustrated in Figure 6.5, the discretized gravity current in the present analysis can always be categorized into three sections, the upper and lower curves as well as the middle rectangle sections. To reduce the computational time, we assumed the current characteristics at $t = t_2$ in each section to be the mean value from the intermediate stage ($t = t_1^*$) of the respective section. This simplification had negligible impact on the simulation results as shown in the subsequent section.

6.3 Experiments

The laboratory investigation was carried out in a glass tank with dimensions of 2 m (long) × 0.9 m (high) × 0.85 m (wide). Fresh water was used as the ambient fluid with water depth, h = 10 cm. A model barge (Figure 6.6, made with two rectangular acrylic boxes) was designed from an actual barge scaled down through volumetric scaling with dimensions of 20 cm (length, L) × 4 cm (width, W_b) × 4 cm (depth, D_b). A finite amount (112 g) of uniformed-size particles (Ballotini Impact beads, Potters Industries, Inc.) with a density ρ_s of 2.5 g/cm^3 was used as the sediments for all tests. Once the experiment was initiated, the two rectangular boxes would rotate in opposite directions with an angular speed, ω (= 1.5 rad/s), forming an opening (opening width, W) in the middle through which the sediments were released. The experimental conditions for each test are listed in Table 6.1, where L/W is the opening aspect ratio and d_{50} is the particle size.

The present study involved two measurements. The gravity currents were illuminated by a spotlight, and their motion were recorded with a video camera (Sony HDR-CX900E), with a resolution of 1920 × 1080 pixels at 25 frames per second. The extraction of gross characteristics (current front: x_c and current height: h_c) from recorded videos was achieved through image analysis using a customized MATLAB program. Each test was repeated five times to ensure repeatability. The average results with the error bars showing the scattering are reported in the subsequent analyses. On the other hand, the final deposition profiles were measured with LAM2D. To minimize the local variations, each profile was taken after three to five cumulative releases and normalized to single release in the subsequent analyses.

In this chapter, instead of using all the four particles that were discussed in Chapter 4, we used only the smallest size particle: particle AE. This was because after scaling with Nc, the particles A, B and D would correspond to gravels in the field, which may not be commonly found during the land reclamation and dredging activities. For particle AE, the corresponded particle size in field was ~ 1 mm (sand), which was closer to the size of sediments expected during the real operations.

Table 6.1 Test conditions

Test notation	W (cm)	L/W	d_{50} (mm)	t_e (s)[#]
AE-LW05	4	5	0.120	3.5
AE-LW10	2	10	0.120	5.1
AE-LW24	0.8	24	0.120	8.2
AE-LW40	0.5	40	0.120	10.8

[#] t_e are estimated from BSDM, and close to the value recorded from experiments

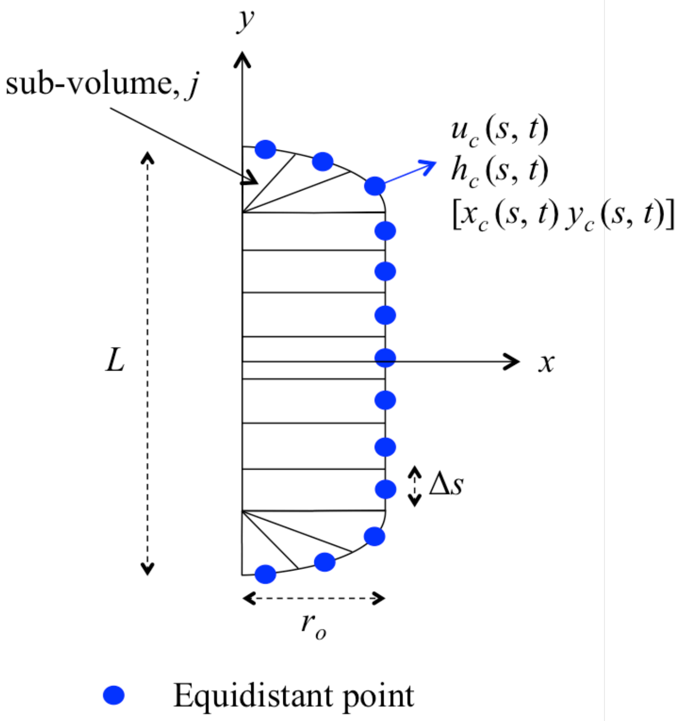

Figure 6.3 Discretization of gravity current at $t = 0$ s

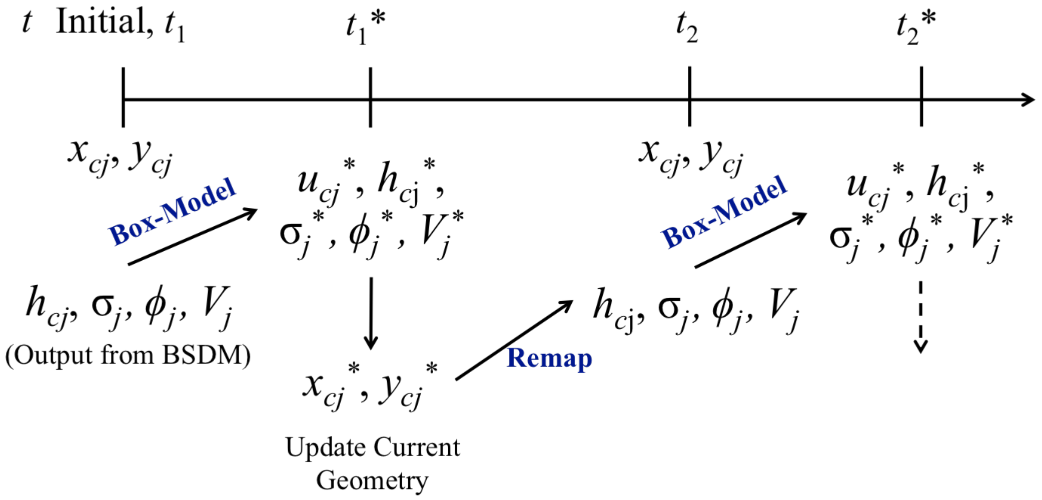

Figure 6.4 Computational step (intermediate stage and remapping stage)

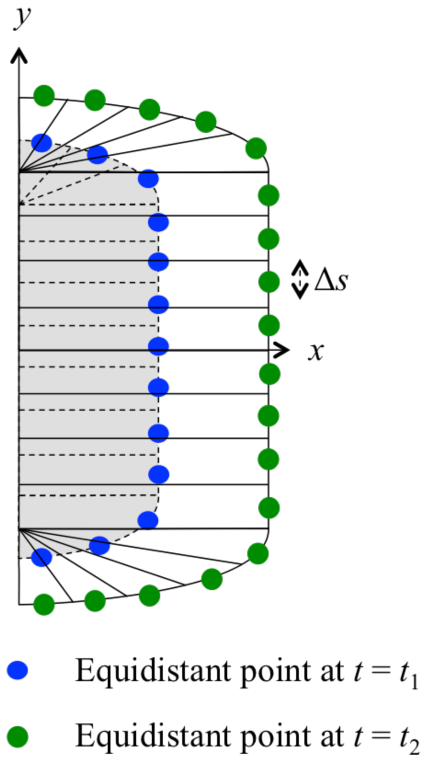

Figure 6.5 Assignment of new equidistant points and sub-volume (not drawn to scale)

6.4 Comparison of Model Predictions with Experimental Data

6.4.1 Gravity Currents Comparison

Once the sediment cloud front impacted the seabed, the sediment cloud transformed into gravity currents and propagated away from the barge (source) along two directions (+*x* and –*x*). Both currents were nearly identical and the averaged values were used in the subsequent analyses. The duration of transformation was rather short (less then 0.2 s, ~ 4 – 5 frames), and hence was not considered in the model. Figure 6.7 illustrates the dynamic motion of the gravity currents from Experiments AE-LW05 and AE-LW40, with $t = 0$ denoting the initiation of the experiments. At the beginning of the spreading, x_c grew linearly with time as a signature of the slumping phase. Subsequently, x_c increased slowly due to the transition to the inertial phase and the deposition of particles from the gravity currents, which reduced the buoyancy force. In the experiments with smaller openings (i.e. larger *L/W*), the initial buoyancy forces were less than the experiments with larger openings, as observed and also predicted from BSDM. Hence, the growth of gravity currents was weaker.

The predictions from the modified Box-Model (M. BM) are included in Figure 6.7 as solid or dashed lines for comparison. Based on the preliminary experiments, the gravity currents along the centerline ($y = 0$, at the center of barge) had the greatest propagation rate. Hence, the recorded x_c were assumed to be the centerline value. On the other hand, the recorded h_c might be from any cross-section where the current (or sub-volume) was the highest. So, the h_c from M. BM in the figure was from the highest h_c out of all the sub-volumes. The simulation terminated when 99% of the sediments settled onto the seabed.

For Experiment AE-LW05, the horizontal propagation of the currents was well predicted by the model. However, the predicted h_c posed slight fluctuation when the currents propagating along the seabed. This might be due to the fact that h_c was taken from different sub-volumes during the simulation. For Experiment AE-LW40,

x_c was well predicted at the beginning until $t = 10$ s. After that, the propagation rate of the currents reduced and the model over-predicted the growth of x_c. This might be due to the model assumption that all the released sediments would enter the currents, increased the density difference (buoyancy force) and contributed to the spreading motion. However, in reality, especially when t approached t_e, the released sediments might not gain enough momentum to travel into the currents and would only settle near the source. This discrepancy might be significant when L/W was large or t_e was long.

In addition, Figure 6.7 also shows the simulated results for x_c from STFATE. In STFATE, the opening would affect the insertion speed of the layer and the simulation started only when the first layer of sediments reached the bottom. Overall, our model substantially improved the predictions of the gross characteristics of the gravity currents due to barged sediment disposal. Despite the slight discrepancy in x_c when L/W increased, the maximum horizontal extents of the gravity currents agreed well with the experimental data. During practical engineering assessment, the horizontal spreading of the gravity currents is more important than the current height, as it indicates the zone influenced by the disposal event. Hence, the minor deviation in h_c estimated by M. BM is acceptable.

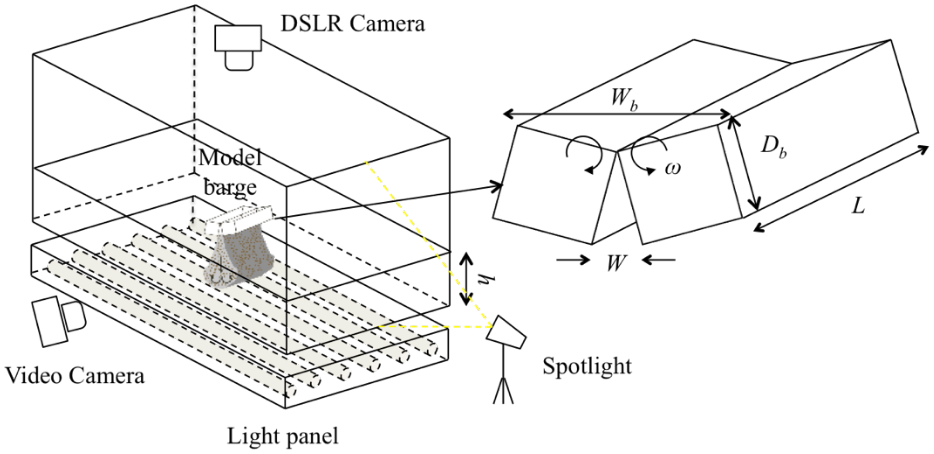

Figure 6.6 Experimental setup

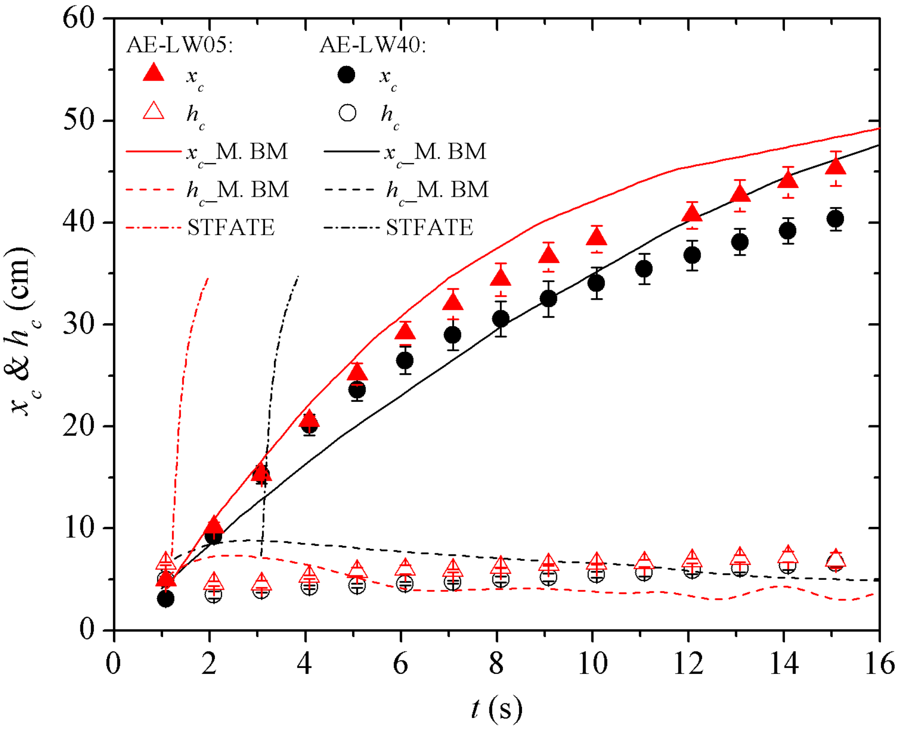

Figure 6.7 Comparison between experimental results and model prediction (M. BM) for the development of current front (x_c) and current height (h_c)

6.4.2 Deposition Profiles Comparison

In Figures 6.8 to 6.11, the sediment deposition profiles (h_s vs. x, where h_s is the sediment thickness) for all four experiments at different cross-sections (y = 0, 5, 10 cm) are presented. These three cross-sections are selected for comparison and discussion because y = 0 and 10 cm represented the profiles at the center and edge of the barge, respectively, and y = 5 cm was the middle of the above two cross-sections. The initial expectation on the distribution of deposition profile was a more uniform profile, as the extra momentum created by the impact might flush the sediments to propagate further downstream and spread evenly. However, a large portion of sediments settled near the source region and induced a greater sediment thickness. Based on the figures, the amount of sediments deposited near the source region increased as *L/W* increased (reduction in opening size).

By comparing the profiles at $y = 0$ and 5 cm, only slight differences could be identified with the sediment thickness at $y = 5$ cm usually lower than that at $y = 0$ cm. At the edge of the barge ($y = 10$ cm), a huge drop in sediment thickness was observed and expected. This was due to the fact that the gravity currents also spread longitudinally at the edges of the barge. Thus, resulting the deposition contour had an ellipse-like shape with the major axis laid on the x-axis (or transverse direction) as illustrated in Figures 6.12 and 6.13. It should be noted that under the stagnant ambient condition, the deposition contour had four quadrants and each quadrant was the mirror images of the neighboring quadrants.

For Experiments AE-LW05 and AE-LW10, h_s were well predicted by the model. However, as L/W increased, the discrepancy between experimental results and model predictions became larger, especially in the regions near the source and at the cross-section of $y = 10$ cm. The same argument that previously made on explaining the over-prediction in x_c could also be used in this deviation. As t approached t_e, the disposed sediments did not have sufficient momentum as the sediments that first impacted on the bottom, hence these sediments only increased the bulk current density and the buoyancy force of the gravity currents, but settled near the source. The same phenomenon was also observed by Nguyen *et al.* (2012) when comparing their experimental study and CFD simulations with two-phase models.

Figures 6.12 and 6.13 illustrate the deposition contours for Experiments AE-LW05 and AE-LW40, respectively. The white dashed lines (ellipse) marked the maximum extent (in both x- and y-axes) of the deposition profiles based on the experimental results. For Experiment AE-LW05, the maximum extent and the sediment thickness were well predicted. The predicted contour had a greater amount of sediments settled within the region of $-10 \text{ cm} < y < 10 \text{ cm}$ than outside, while the experiments indicated a more gradual change in slope between these two regions. For Experiment AE-LW40, the longitudinal spreading was over-estimated, despite the prediction within the region of $-10 \text{ cm} < y < 10 \text{ cm}$ being fairly good. By analyzing the sediment mass in the predicted contour, more than 90 % of the sediments deposited within the white ellipse, which implied that only less than 10 % of the sediments were estimated to be deposited out of the actual deposition zone.

In general, the deposition profiles and contours were well predicted by the model. The inclusion of sediments from the sediment plume stem over-predicted the motion of the gravity currents and the subsequent deposition profiles. However, the same problem was also observed by Nguyen *et al.* (2012) when simulating with their CFD model. For the purpose of engineering assessment, a short computational time is always preferred without sacrificing much accuracy. During the simulation, mass conservation error was the main parameter to be checked to ensure the model performed correctly, and the absolute error was less than 5 % for all cases.

6.5 Summary and Conclusions

In the present study, a modified Box-Model was developed for the assessment of the gravity currents due to open water disposal of barged sediments. The model takes into account the transition from constant flux to constant volume release, and the transformation of current geometry with the volume discretization approach. An experimental study was carried out for the verification. The comparisons of the results from the dynamic motion of gravity currents showed that the predictions from the modified Box-Model were substantially better than the previous engineering model, STFATE. The deposition profiles were also well predicted by the model. The only remaining limitation is the inclusion of sediments from the sediment plume when t approaches t_e, while in reality the sediments just settle near the source region without propagating with the gravity currents. From an engineering perspective, this model is coupled with BSDM to determine the transport and deposition of barge-disposed sediment after it collapses on the seabed. The present coupling assumes the formation of gravity current happens immediately after the sediment cloud hits the seabed and under a stagnant ambient condition. In reality, the duration of forming the gravity current after the impact may be affected by the ambient conditions (e.g. water depth, wave or turbulence). An experimental study shall be conducted to determine the effect of source and ambient conditions on the time required to generate the gravity current upon impact.

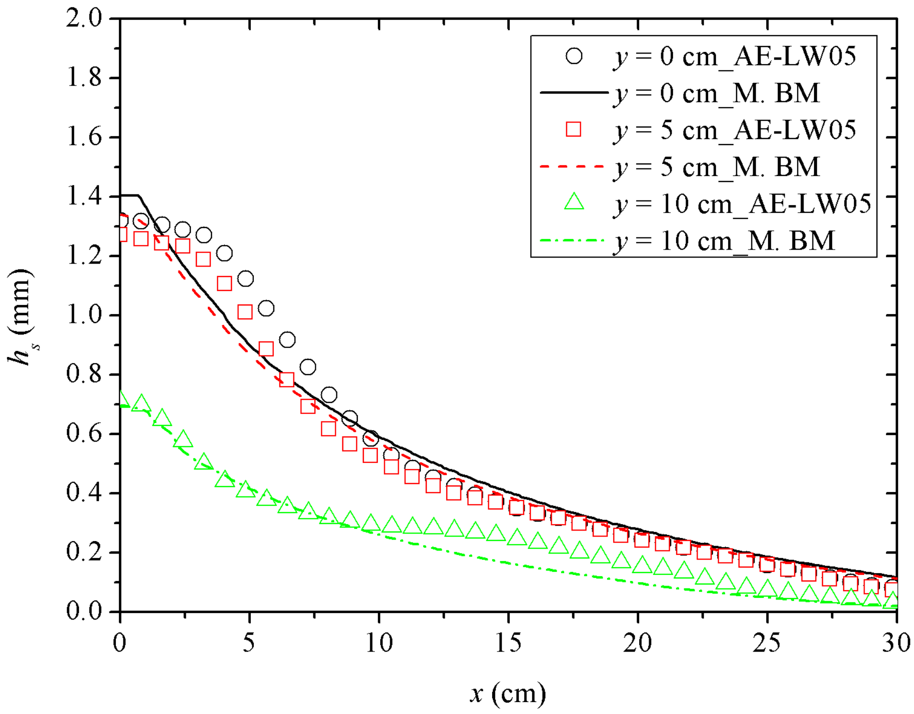

Figure 6.8 Comparison of Experiment AE-LW05 and model prediction (M. BM) for the sediment deposition profile at y = 0, 5 and 10 cm

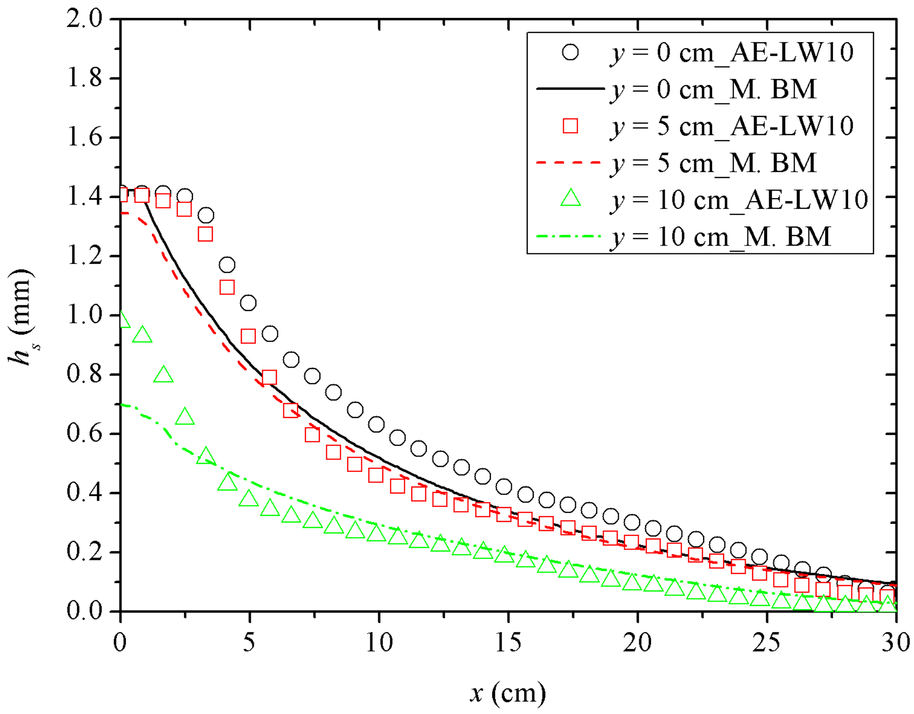

Figure 6.9 Comparison of Experiment AE-LW10 and model prediction (M. BM) for the sediment deposition profile at y = 0, 5 and 10 cm

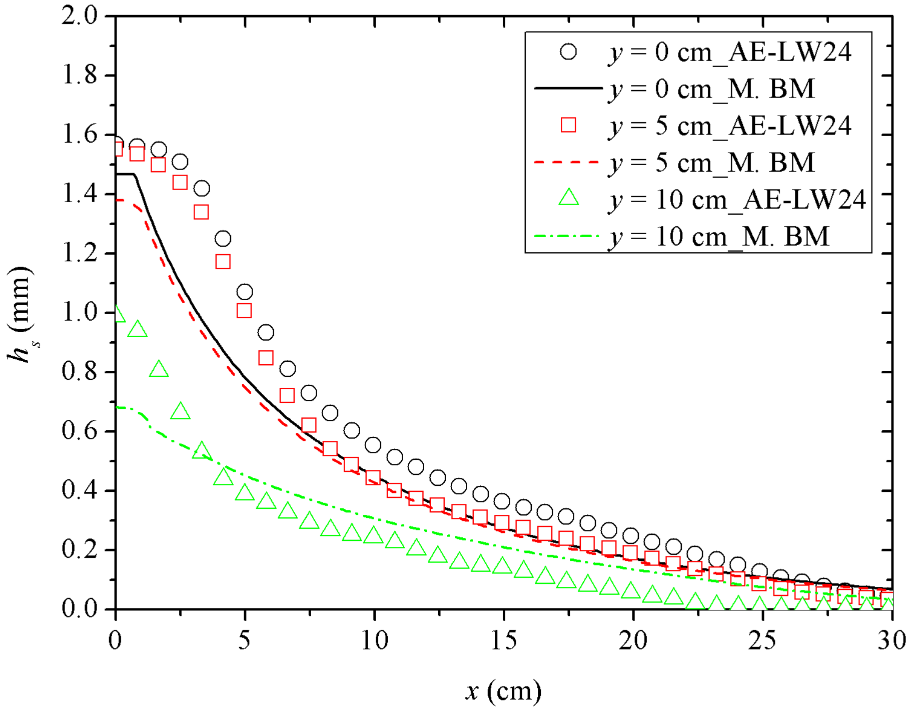

Figure 6.10 Comparison of Experiment AE-LW24 and model prediction (M. BM) for the thickness of sediment deposition profile at y = 0, 5 and 10 cm

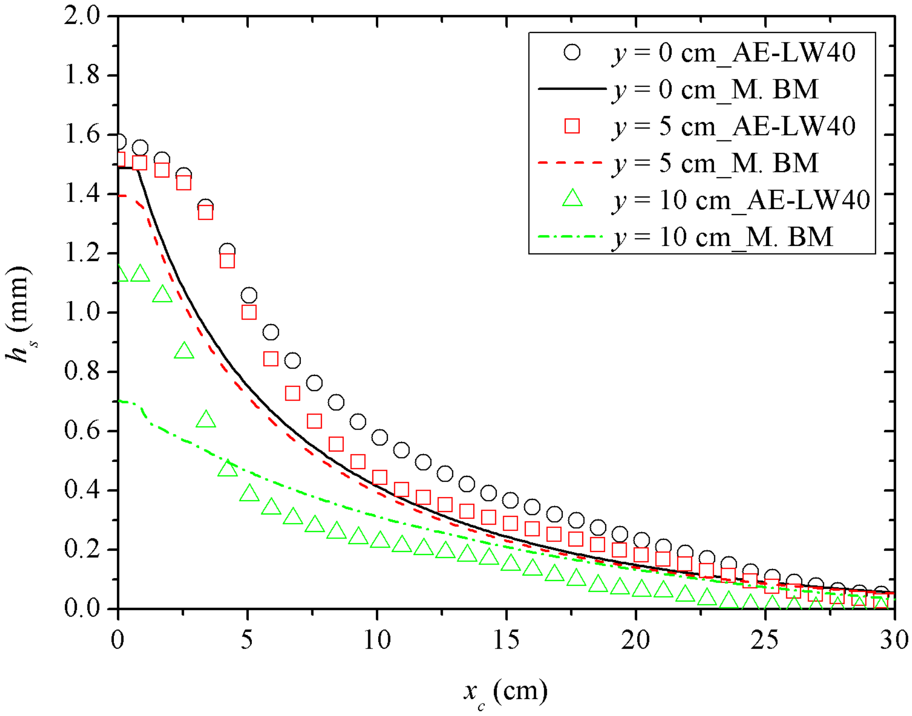

Figure 6.11 Comparison of Experiment AE-LW40 and model prediction (M. BM) for the thickness of sediment deposition profile at y = 0, 5 and 10 cm

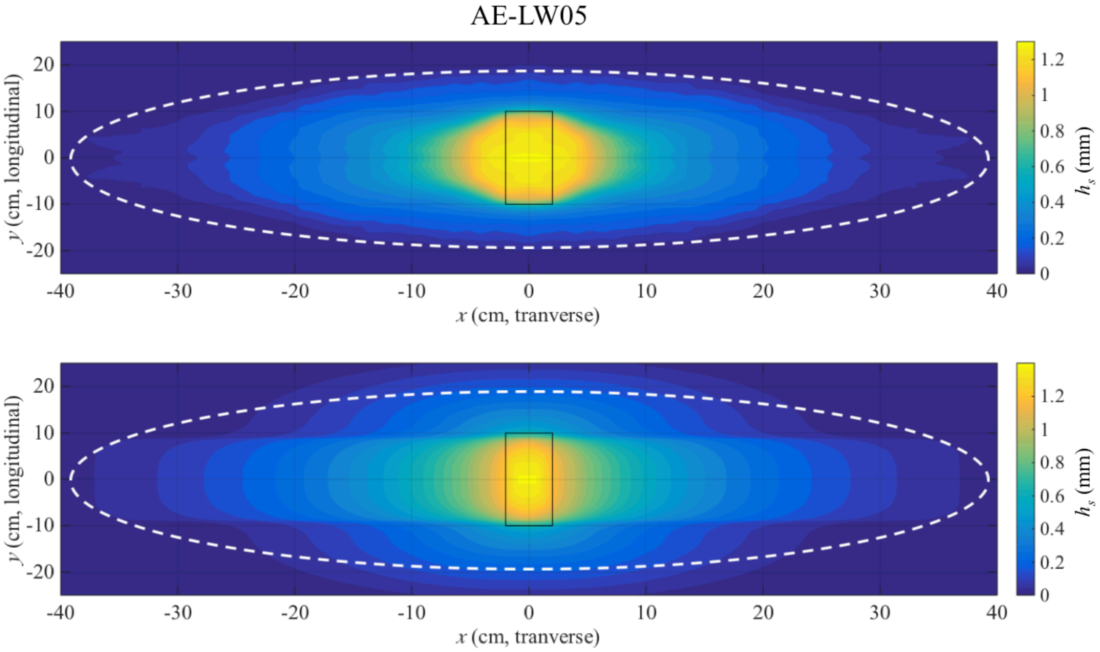

Figure 6.12 Sediment deposition contours for Experiment AE-LW05 (above) and model prediction (below)

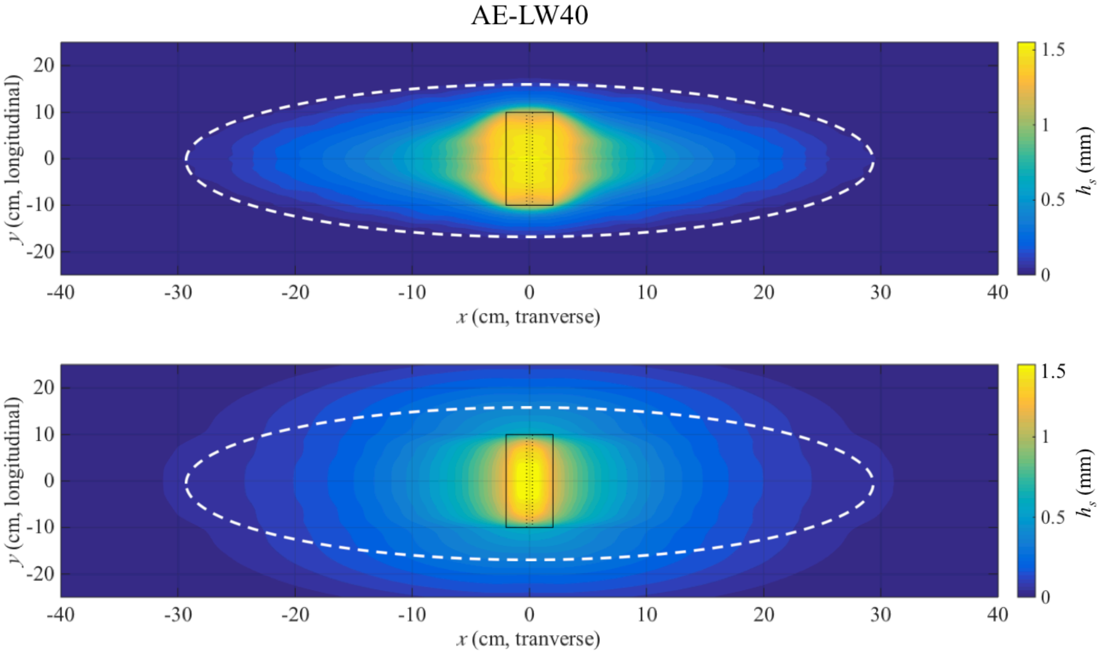

Figure 6.13 Sediment deposition contours for Experiment AE-LW05 (above) and model prediction (below)

Chapter 7

Formation Process of Composite Sediment Clouds

7.1 Introduction

Sediments generated from environmental and navigational dredging operations are commonly disposed at designated open water disposal sites (Eisma 2006). Due to the substantial quantities involved, environmental issues such as turbidity formation need to be assessed carefully. Previous research has been devoted to understanding the fate and transport of disposed sediments due to various sources and ambient conditions. Koh and Chang (1973) developed a mathematical model based on a self-preserving miscible thermal to analyze the motion of a sediment cloud. Subsequently, modified versions of Koh and Chang (1973)'s model have been proposed to account for the effects of particle size and initial water content (Ruggaber 2000), ambient stratification (Bush *et al.* 2003), air release height for above water releases (Zhao *et al.* 2012), and passive advection by ambient currents and waves(Gensheimer *et al.* 2012, Zhao *et al.* 2013a). In addition, a recent analysis by Lai *et al.* (2013) combined an integral model with particle tracking equations to simulate the distinct two phase solid-fluid characteristics. For engineering assessment and applications, Johnson and Fong (1995) developed the software STFATE based on Koh and Chang (1973)'s model, to assess the short-term fate of disposed sediments. STFATE remains one of the most popular tools to date.

Note: The material presented in this chapter has been prepared to be submitted to Journal of Fluid Mechanics, Rapids for the consideration of publication

7.1.1 Formation Processes

Sediments can be discharged through various disposal facilities (e.g. pipelines, split barges and backhoes) based on their properties and quantities. Depending on the discharge duration, the disposal process can be classified as instantaneous or quasi-continuous. Here, the focus is on instantaneous release from split barges or backhoes, during which the time to fully discharge the sediments is relatively short compared to the time for the sediments to experience its initial acceleration regime (P1 and P2 processes in Figure 1.4).

In general, instantaneously released sediments have been conceptualized to descend as a group and form a thermal-like particle cloud, whose behavior is governed by the total buoyancy excess (Bush *et al.* 2003, Zhao *et al.* 2013b). The descent can be broken into three regimes: acceleration, self-preserving and dispersive regime (Rahimipour and Wilkinson 1992). During the self-preserving regime, the particle cloud is characterized by a coherent vortex and behaves similarly to a single-phase miscible thermal. However, Wen and Nacamuli (1996) and Zhao *et al.* (2014) observed a new regime with the formation of clumps, which are characterized by a fast-moving, particle-rich core that continuously sheds particles into the wake (tail region). This flow behavior, which is referred to as `wake-like' or clump regime here, has significant environmental implications but has not been taken into account in assessments so far. The distinct features of thermal- and wake-like formations are illustrated in Figure 2.3. The sediment cloud experiences the thermal-like formation has high entrainment velocity at the rear of the sediment vortex, which hold the solid particles together to descend as a group with very little loss to the tail region. Therefore, the sediment appears only as a narrow dark band in the horizontally integrated image (Figure 3 (a) of Zhao *et al.* (2014)). However, once the formation process is within the wake-like formation, a significant amount of particles is left behind the leading clumps, and thus becomes more susceptible to be carried away by ambient flows. The wake-like formation is reflected in the horizontally integrated image as a wide and blurry dark band (Figure 3 (c) of Zhao *et al.* (2014)).

In addition to this observation, Zhao *et al.* (2014) further found that the formation process of sediment clouds with uniform grain size was governed by a source cloud number, *Nc*, defined as the ratio of the settling velocity (w_s) of individual particles to the characteristic circulation velocity (w_t) within the sediment cloud:

$$Nc = \frac{w_s}{w_t} = \frac{w_s}{\sqrt{B_o / r_o}} \propto \frac{w_s}{\sqrt{r_o \Delta g}} \tag{7.1}$$

where $w_t = \sqrt{B_o / r_o}$; $r_o = [(3V_o)/(4\ (1 - e)\ \pi)]^{1/3}$ is the initial equivalent radius of a sphere with the same bulk volume (V_o) as the sediments; $B_o = V_o \Delta g$ is the total buoyancy excess; *e* is the void ratio, assumed constant for particles initially at settled state; $\Delta = (\rho_s - \rho_a)/\rho_a$ is the normalized density difference; and *g* is the gravitational acceleration. The motion of quasi-instantaneously released sediments is governed by the total excess buoyancy (B_o). Characteristics scales, defined as

$$L_n = B_o^{1/3} g^{-1/3},\ T_n = B_o^{1/6} g^{-2/3},\ U_n = B_o^{1/6} g^{1/3} \tag{7.2}$$

can be used for analysis under different conditions. Through analogy with flow passing through a porous sphere, Zhao *et al.* (2014) also showed theoretically that *Nc* represents the resistance for water to flow through and disintegrate the sediment clumps. As the source *Nc* increases/decreases, the resistance becomes lower/higher and the sediment cloud tends to behave more thermal-/wake-like (i.e. tends to experience P1/P2 process). They also obtained a critical *Nc* value of 3.2×10^{-2} that distinguishes the formation of these two processes.

7.1.2 Composite Sediment Clouds

In practical dredging operations, disposed sediment typically consist of multiple grain sizes (Okada *et al.* 2009). The formation process of polydispersed sediment clouds should be investigated because *Nc* depends on w_s, which is mainly governed by the grain size (d_{50}). We can expect that coarser sediments tend to have thermal-like behavior, while finer sediments tend to form sediment clumps with wake-like behavior.

We conducted 27 laboratory experiments by releasing sediment mixtures of five difference sizes with various proportions. The formation process was analyzed using the composite cloud number, *Ncc*, defined subsequently, which was expected to include both thermal- and wake-like formation. In the following, the experiments are introduced in Section 7.2; observation on the formation process are described and gross characteristics are analyzed in Section 7.3, then a summary of findings is presented in Section 7.4.

7.2 Experiments

Experiments were conducted in the glass tank of 2.85 m (long) × 0.85 m (wide) × 0.95 m (tall). Dry sediment was initially held inside a latex-sealed cylindrical tube with inner diameter of 1.8 cm. A motor driven needle was placed along the centerline of the tube with its tip touching the membrane. Once the experiment was initiated, the needle would make a 0.5 cm downward displacement and pierce the latex seal, resulting in an instantaneous axisymmetric release. The motion of the sediments underwater was illuminated by a spotlight and recorded using a video camera (SONY HDR-XR550E) with resolution of 1080 × 1920 pixels at 25 frames/s. Each test was conducted five times to ensure repeatability.

Glass beads (Ballotini Impact beads, Potters Industries, Inc.) with density of $\rho_s = 2.5\ \mathrm{g/cm^3}$ were adopted to mimic real sediments. Following the manufacturer's standards, five sizes labeled as A (median diameter of $d_{50} = 0.725$ mm), B ($d_{50} = 0.513$ mm), D ($d_{50} = 0.256$ mm), AE ($d_{50} = 0.120$ mm) and AH ($d_{50} = 0.068$ mm) were utilized, resulting in a maximum diameter ratio (diameters of the coarsest to finest sediments) of 10.7. Table 7.1 lists the proportion of each size in the 27 tests, where m is the mass of particles and subscripts represent grain sizes. Tests with uniform grain size (Test N1_AH and N1_D), which had been reported in Zhao *et al.* (2014), were included for comparison. Subsequently, Tests N2 released mixtures of the same particles (i.e. D and AH) with different mass proportions. From Tests N3 onwards, the total mass of particles was 11 g, and various mass distributions were adopted (evenly distributed, skewed toward coarser or skewed toward finer sediments). The sediments were uniformly mixed and carefully prepared to avoid clumping before release.

For the analysis of composite sediment clouds with mixed grain sizes, Lai *et al.*

(2016) defined a composite cloud number, *Ncc* based on the buoyancy weighted settling velocity (w_{se}), which can be expressed as:

$$Ncc = \frac{w_{se}}{w_t},\ w_{se} = \frac{\sum_{i=1}^{n} w_{si} B_i}{B_o} \tag{7.3}$$

where B_i and w_{si} are the buoyancy excess and settling velocity of particles of size *i*. The concept behind this definition is that the influence of a particular sediment size is proportional to the buoyancy carried by the particular sediment mass. In the present experiments, the maximum number of particle groups (*n*) was equal to 5 and *Ncc* ranged from 6.0×10^{-3} to 6.7×10^{-2}, which was expected to cover the transition from wake- to thermal-like formation process.

7.3 Results and Discussions

The development of 6 representative sediment clouds is illustrated in Figure 7.1 using both instantaneous and integrated images. As total sediment mass differed among tests, the length and time scales are non-dimensionalized by characteristic scales defined in Equation (7.2). The key observation here is the gradual transition from wake- to thermal-like as *Ncc* increases. For monodispersed clouds, Zhao *et al.* (2014) showed that the wake-like formation ($Nc < 3.2 \times 10^{-2}$) features an elongated shape (i.e. large length-to- width ratio) caused by the fast-moving leading clump(s) and the continuous shedding of sediments along its path. By contrast, the thermal-like formation ($Nc > 3.2 \times 10^{-2}$) features a flattened elliptical shape (i.e. small length-to-width ratio) similar to a single-phase miscible thermal, due to the formation of sediment vortices. From top to bottom in Figure 7.1, the degree of thermal-like behavior becomes more apparent as *Ncc* increases. This can be observed from the narrowing trend of the dark bands in horizontally integrated images (i.e. the panels in the first column) and the decreasing trend of length-to-width ratios in the instantaneous images.

In tests with high *Ncc*, the development process is complicated even though the bulk sediment clouds behave thermal-like. Upon water entry, the finer sediments form some localized-clumps that are small in size and usually found at the edge of the main cloud (Figure 7.1, Test N2_D2AH1 at $t/T_n = 50$). The localized-clumps are fundamentally different from the sediment clumps that formed in the wake-like or clump regime, and disintegrate over a short period of time, without leaving a great amount of particles in the tail region. It may be argued that the faster disintegration of localized-clumps is due to lesser amounts of finer sediments being released. By comparing Tests N2_E1 and N2_D2AH1, with the same amount of finer sediment ($m_{\mathrm{AH}} = 2.75$ g), the former behaves wake-like with an elongated shape while the latter behaves thermal-like even though more localized-clumps are found. The impact of localized-clumps is only observed during the initial stage of composite sediment cloud development with high *Ncc*, which will be discussed in the subsequent subsection.

In general, as the bulk sediment cloud descends and the circulation velocities of the sediment cloud decrease, the coarser sediments with higher settling velocities are the first to enter the dispersive regime. This process is analogous to the phase separation of sediment clouds with uniform grain size shown in Lai *et al.* (2013). By releasing a sediment-dye mixture, they found that after the sediments entered the dispersive regime, the fluid phase was left behind and would continue to travel downward with the residual momentum as a puff. When sediments with mixed grain sizes are released, the sediments separate from the main cloud sequentially according to their settling velocities (i.e. grain sizes) in a bowl-shape cloud, as illustrated in Figure 7.1 (Test N4_E1 at $t/T_n = 100$). The separation can also be identified by the bifurcation of dark bands at later times in the horizontally integrated images of Tests N2_D2AH1 and N4_E1 in Figure 7.1. After the separation, the vortical structure built up by the coarser sediments holds the finer sediments together so they descend in an integrated manner, thus helping to reduce turbidity and subsequent sediment loss in the ambient waters.

Overall, the coarser sediments were observed to make two major contributions towards the formation process of composite sediment clouds. First, the larger pore size associated with the coarser sediments makes it easier for the ambient water to flow through the sediment mixtures and disintegrate the clumps. This is reflected quantitatively by the higher *Ncc*. Second, the coarser sediments stabilize the vortical flow circulation through the formation of coherent vortex. Practically, the addition of the coarser sediments effectively increases *Ncc*. However, the distance for coarser sediments to separate from the main cloud is inversely proportional to the respective settling velocity (Bush *et al.* 2003). Hence, the diameter ratio should not be too large as the separation may occur too soon before the coarser sediments affect the formation process. As discussed previously, the maximum diameter ratio was 10.7 and the effects of coarser sediments on the formation process were distinct.

Table 7.1 Experimental parameters

Test	m_A (g)	m_B (g)	m_D (g)	m_{AE} (g)	m_{AH} (g)	*Ncc*
N1_AH	0	0	0	0	5.5	6.0×10^{-3}
N1_D	0	0	5.5	0	0	5.0×10^{-2}
N2_E1	0	0	2.75	0	2.75	2.8×10^{-2}
N2_E2	0	0	5.5	0	5.5	2.5×10^{-2}
N2_D1AH5	0	0	1.1	0	5.5	1.3×10^{-2}
N2_D1AH3	0	0	1.38	0	4.13	1.7×10^{-2}
N2_D1AH2	0	0	2.75	0	5.5	1.9×10^{-2}
N2_D2AH1	0	0	5.5	0	2.75	3.3×10^{-2}
N2_D3AH1	0	0	4.13	0	1.38	3.9×10^{-2}
N2_D5AH1	0	0	5.5	0	1.1	4.2×10^{-2}
N3_E1	0	3.67	3.67	0	3.67	5.3×10^{-2}
N3_B1AH5	0	1.57	1.57	0	7.86	2.6×10^{-2}
N3_D2AH1	0	0	5.50	2.75	2.75	2.7×10^{-2}
N3_D3AH1	0	0	6.60	2.20	2.20	3.1×10^{-2}
N3_B1AH3	0	2.20	2.20	0	6.60	3.4×10^{-2}
N3_D5AH1	0	0	7.86	1.57	1.57	3.5×10^{-2}
N4_E1	0	2.75	2.75	2.75	2.75	4.3×10^{-2}
N4_B1AH5	0	1.10	1.10	3.30	5.50	2.2×10^{-2}
N4_B1AE3	0	0.92	2.75	4.58	2.75	2.8×10^{-2}
N4_A1AE5	1.10	1.10	3.30	5.50	0	4.8×10^{-2}
N4_B3AH1	0	2.75	4.58	2.75	0.92	5.0×10^{-2}
N4_A1AE3	0.92	2.75	4.58	2.75	0	6.3×10^{-2}
N5_E1	2.20	2.20	2.20	2.20	2.20	6.7×10^{-2}
N5_A1AH7	0.65	0.65	1.94	3.24	4.53	3.0×10^{-2}
N5_A1AH5	1.00	1.00	1.00	3.00	5.00	3.5×10^{-2}
N5_A1AH3	0.85	0.85	2.54	4.23	2.54	3.8×10^{-2}
N5_A1AH1	0.85	2.54	4.23	2.54	0.85	5.9×10^{-2}

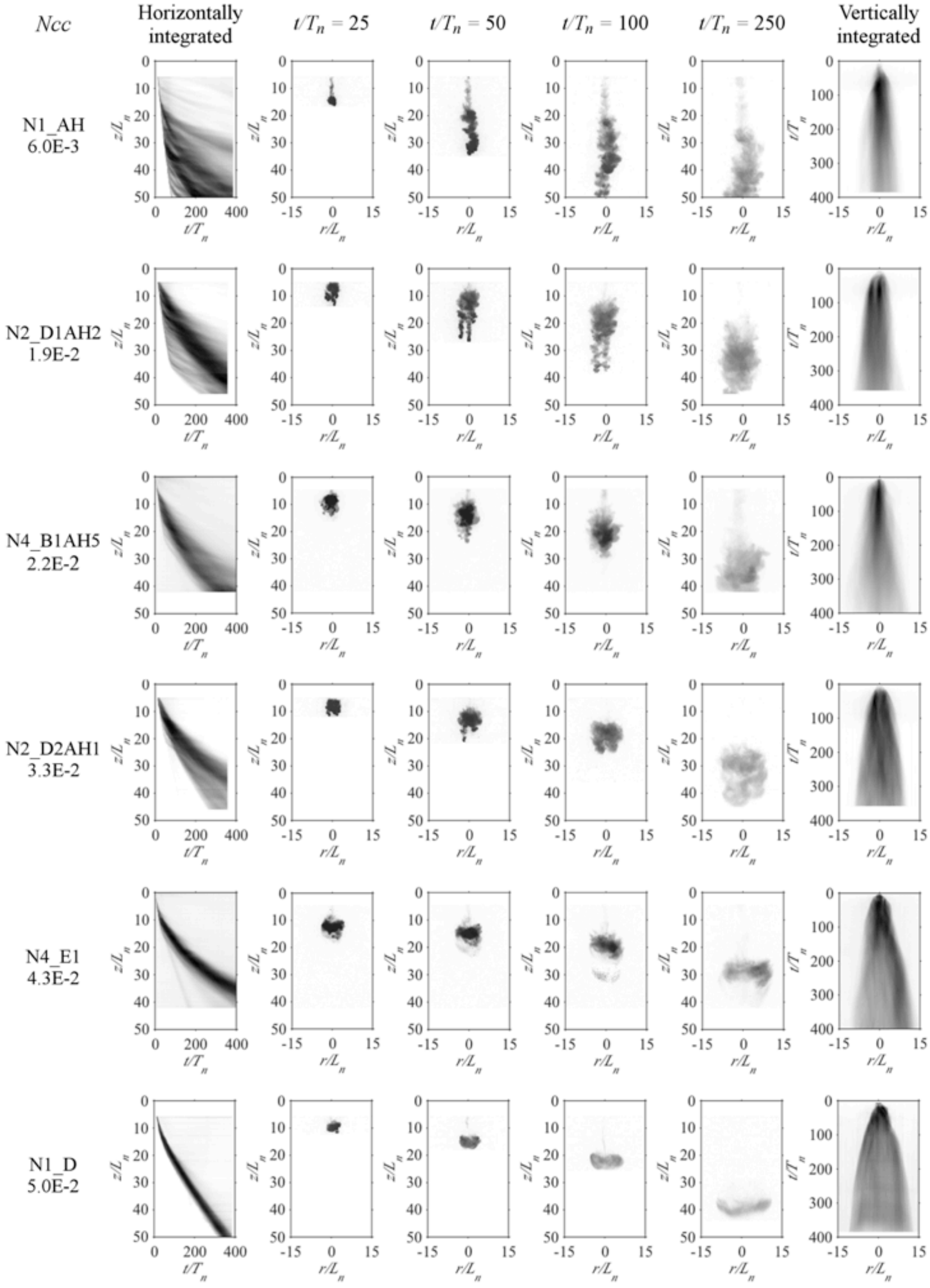

Figure 7.1 A comparison of the formation processes of composite sediment clouds under various source conditions

7.3.1 Aspect Ratio

To assess the degree of thermal- and wake-like behavior quantitatively, Figure 7.3 plots the transient development of the sediment cloud aspect ratio, $l_c / 2r_{max} = (z_f - z_b)/2r_{max}$, where r_{max} is the lateral spread based on the maximum cloud radius, z_f and z_b are the front and tail positions of the sediment clouds, respectively as illustrated in Figure 7.2. The legend symbols are arranged in ascending order according to their *Ncc*, i.e. Tests N1_AH (upper left) and N5_E1 (lower right) had the lowest and greatest *Ncc*, respectively. Each curve ends at the point where either z_f reaches the bottom of the sampling area or phase separation is observed. The typical $l_c / 2r_{max}$ for axisymmetric miscible and sediment thermals is 0.72 (Bush *et al.* 2003), which is indicated by a solid horizontal line in the figure. Upon release, $l_c / 2r_{max}$ increased as a signature of the acceleration regime when the released sediment mass penetrated the water in a bulk manner. Subsequently, $l_c / 2r_{max}$ decreased due to growth in the lateral direction (increase in r_{max}) and the incorporation of finer sediments from the tail region into the main cloud (increase in z_b). $l_c / 2r_{max}$ generally decreased monotonically with increasing *Ncc*. Exceptions are for $t/T_n < 50$ where Tests N4_B3AH1, N3_E1 and N5_E1 had larger $l_c / 2r_{max}$ than Test N1_D even though their *Ncc* were higher. This was due to the localized-clumps, which caused some of the finer sediments were left in the tail region. These localized-clumps disintegrated over a short period of time and $l_c / 2r_{max}$ continued to approach the value of 0.72.

The effect of *Ncc* on $l_c / 2r_{max}$ is further illustrated in Figure 7.4. The graph plots the aspect ratios for all 27 tests at $t/T_n = 75$ as $l_c / 2r_{max}$ approaches fixed values and before z_f reaches the bottom of the sampling area. The critical *Nc* (3.2×10^{-2}) to distinguish wake- and thermal-like formation for sediment clouds of uniform grain size is indicated by a dashed vertical line. Again, a strong decrease in $l_c / 2r_{max}$ with increasing *Ncc* is observed. Also note that the 27 tests include a number of pairs of tests with similar *Ncc* but substantially different composition. For the most part these tests show similar results supporting the definition of *Ncc* based on Equation (7.3). Slight variation in $l_c / 2r_{max}$ is observed with *Ncc* ranging from 2.5×10^{-2} to 3.5×10^{-2}. This might be due to the transitional formation process suggested by

Zhao *et al.* (2014), within which the sediment cloud of uniform grain size behaves wake-like upon release then transits to thermal. However, this phenomenon is hard to quantify in composite sediment clouds due to the localized-clumps was found upon release, and also the more gradual separation of coarser sediments from the main cloud.

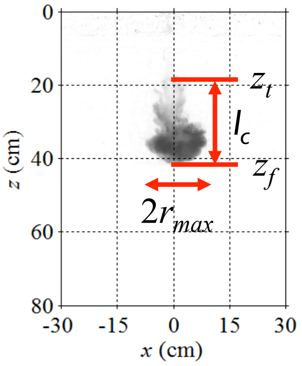

Figure 7.2 Illustration for z_t, z_f, l_c and r_{max}

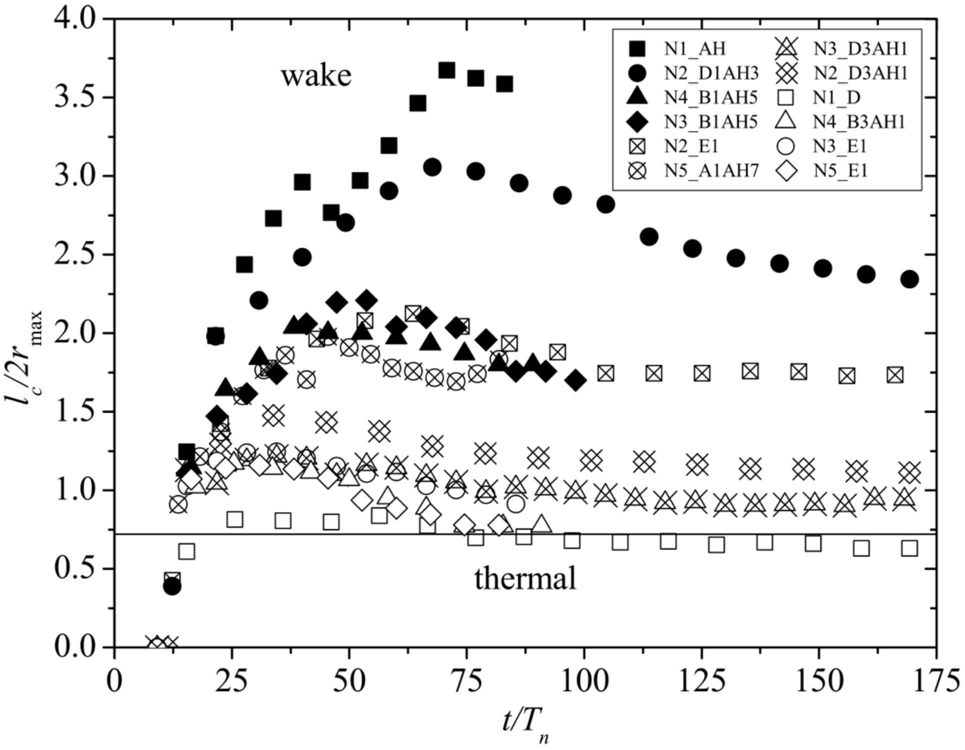

Figure 7.3 Transient development of aspect ratio

7.3.2 Critical Composite Cloud Number

The formation process has been shown to depend on *Ncc*. Here, the critical *Ncc* distinguishing wake- and thermal-like formation processes is identified by comparing the behavior of sediment clouds with the asymptotic solutions of single-phase miscible thermals. Note that, due to the nature of composite sediment clouds as discussed in the previous section, the transitional formation process is hard to identify. Hence, here we characterize the formation process by only two distinct formations (P1 and P2), distinguished by a critical *Ncc*.

We present the behavior of sediment clouds by two characteristics: z_f and r_{max}, and plot in Figures 7.4 and 7.5, respectively. The asymptotic solutions of single-phase miscible thermals, i.e. $z_f \sim t^{0.5}$ and $r_{max} \sim t^{0.5}$ are also plotted with solid lines. In tests with $Ncc \leq 3.0 \times 10^{-2}$, z_f initially increased at fast rate with limited lateral spreading. This was due to the formation of clumps and the higher resistance to clump disintegration at the beginning of the descent. After the clumps disintegrated, slope breaks could be observed (arrows in Figure 7.5) and the subsequent descent velocity dropped significantly. On the other hand, for tests with $Ncc > 3.0 \times 10^{-2}$, the experimental results tended to collapse into a single curve, suggesting that the flows were dominated by the total buoyancy excess. The comparisons between the collapsed curves and asymptotic solutions indicated that the flow regime in these tests was thermal-like (P1). The critical value of $Ncc = 3.0 \times 10^{-2}$ was nearly identical to the critical *Nc* (3.2×10^{-2}) of uniform grain size found by Zhao *et al.* (2014). This is physically expected as the critical criteria for the formation of mixed grain size sediment clouds should include the asymptotic case when the sediments have uniform grain size.

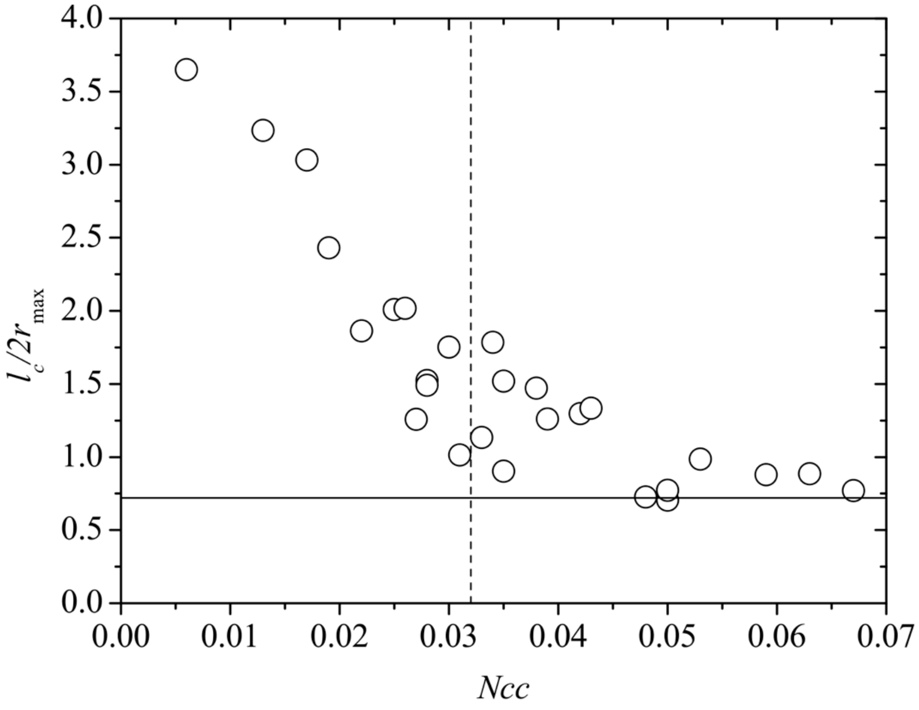

Figure 7.4 Aspect ratio of the composite sediment clouds vs. *Ncc* at $t/T_n = 75$

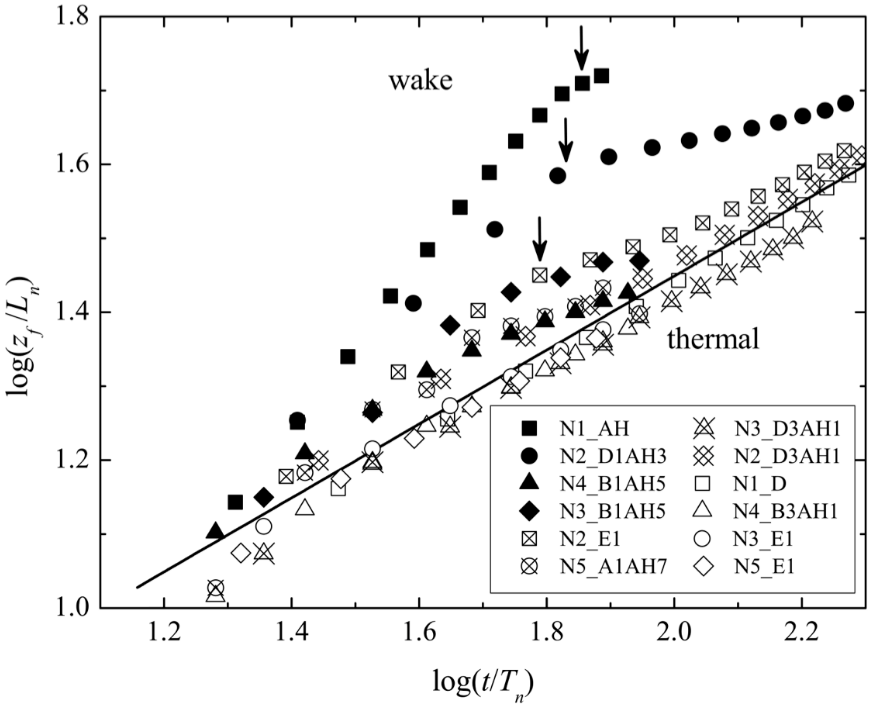

Figure 7.5 Non-dimensionalized frontal position vs. time. The solid line indicates the asymptotic solution of the single-phase miscible thermals, $z_f \sim t^{0.5}$

7.4 Summary and Conclusions

The present study examines, for the first time, the formation process of composite sediment clouds with mixed grain sizes, including both thermal- and wake-like. The development processes of the composite sediment clouds were investigated through a total of 27 laboratory experiments. The composite cloud number (*Ncc*) from Lai *et al.* (2016) was adopted for analysis. By varying the percentages of particles with five different sizes, the experimental conditions achieved a wide range of *Ncc* from 6.0×10^{-3} to 6.7×10^{-2}, which covered the transition from wake- to thermal-like formations. Results showed that wake- and thermal-like formation can be distinguished by a critical *Ncc* (3.0×10^{-2}), which can be used directly for future engineering assessment of sediment disposal operations. At this point, only bulk characteristics of the formation process have been quantified through image-based indicators with five relatively discrete sediment sizes. Since field sediments typically display a wide and continuous distribution in size, more extensive field investigation towards generalization of the *Ncc* will be considered in the future.

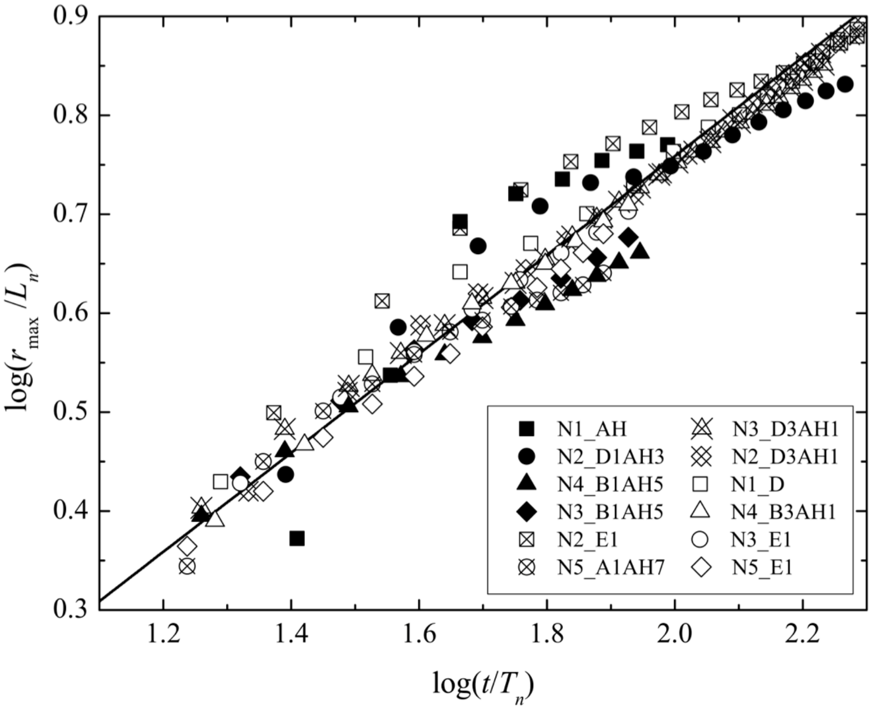

Figure 7.6 Non-dimensionalized cloud radius vs. time. The solid line indicates the asymptotic solution of the single-phase miscible thermals, $r_{max} \sim t^{0.5}$

Chapter 8

Conclusion and Recommendation

The major conclusions of the work are outlined in this chapter followed by a list of recommended areas for future work.

8.1 Conclusions

8.1.1 Sediment Clouds and Gravity Currents due to Barged Sediment Disposal

Two engineering models, Barged Sediment Disposal Model (BSDM) and Modified Box-Model (M. BM) were established for the assessment of the open water disposal of barged sediments in both convective descent and bottom collapse phase, respectively. Experimental studies were conducted for the models verification. The major outcomes and contributions are summarized below:

- The models took into account the realistic physical condition in which the disposed sediments, due to the large and finite amount of sediments typically carried by the barge, would initially descend as a sediment plume and then transited into a discrete sediment cloud after the barged sediments were fully discharged. This transition had also significantly affected the dynamic motion of the gravity currents (from constant flux to constant volume) that formed after the impact.
- The models also included the geometrical factors of the barge, which is due to the rectangular bottom opening with specific aspect ratio, the sediments

would initially descend as a two-dimensional sediment plume and then transited into a bowl-shape sediment cloud. The gravity currents generated by a two-dimensional sediment cloud would have greater spreading in the transverse direction and caused the deposition profile to have a switch in major axis.

- The comparison with experimental data showed the predictions from BSDM were substantially better than the existing models (K&C model and STFATE). The analyses were conducted in two ways, on examining the flow regimes and the transient development of the gross characteristics. The initial starting plume regime with constant velocity was well computed by the model, followed by the transition to other flow regimes. The prediction of actual field disposal operation of Bokuniewicz *et al.* (1978) was also in good agreement.
- The dynamic motion of gravity currents and the final deposition profiles were well predicted by M. BM. The only remaining limitation was the incorporation of sediments from the sediment plume when $t \approx t_e$, which caused an over-prediction in the spreading of the gravity currents.

8.1.2 Formation Process of Composite Sediment Clouds

The formation process of composite sediment clouds with mixed grain sized was investigated through a set of laboratory experiments. The composite cloud number, *Ncc* proposed by Lai *et al.* (2016) was adopted for analysis. The major outcomes and contributions are summarized below:

- The formation process was justified by the degree of thermal-like behavior of the disposed sediments, which could be quantitatively determined by the sediment cloud aspect ratio. A gradual transition from wake- to thermal-like behavior was observed when the *Ncc* of the disposed sediments increased.
- A critical *Ncc* (= 3.0×10^{-2}) was determined through the comparison between the transient development of gross characteristics and the asymptotic solution of thermal regime. This value was closed to the critical *Nc* for the case of uniform grain size.

8.1.3 An Improved Light Attenuation Method for 2D Data Acquisition

The light attenuation method (LAM) was developed for quantifying the sediment deposition profiles with high spatial and temporal resolutions. The improved LAM2D had an advantage on measuring the profiles with shallow sediment depth (< 2 mm) over the previous LAM. The major outcomes and contributions are summarized below:

- An unified calibration techniques was utilized in LAM2D:
    - The deep sediment depth (> 2 mm) was calibrated with the traditional scraper method by preparing multiple sediment layers with known depths. However, this method had difficulty in preparing sediment profiles with less than 2 mm in thickness.
    - The shallow sediment depth (< 2 mm) was calibrated with the correlation of particle plume deposition profiles (distribution of sediment thickness and attenuated intensity profiles). The generated profiles must be highly consistent between each batch of experiment.
- The calibration curve for each region was established with data only in the respective region.
- Verification experiments showed that the LAM2D reduced the mass conservation error significantly compared with the previous approach with calibration based only on the scraper method.

8.2 Recommendations

Based on the experience gained through the present study, a few topics are recommended here for future research.

- A software program with GUI (Graphical User Interface) will be designed for BSDM and B. MB model. The program allows the users to input the parameters such as sediment properties, release and ambient conditions to carry out the assessment. The output of the program can be served as the input for the far field model and the coupling between these two models will be investigated in future.

- The effect of waves and tidal currents on the barge-disposed sediments will be carried out in future with numerical and experimental studies. The findings will be included in the above-mentioned program to enhance its robustness.
- The behavior of clump regime in the P2 process is still rather unknown, despite this formation process poses a great threat to the environment due to significant amount of suspended sediments generated. Looking forward, an experimental study to quantify the behavior of sediment clump, sediment loss and the deposition profiles generated by the sediment clumps will be conducted.

References

Aguirre-Pe J., Olivero M. L. and Moncada A. T. (2003) "Particle densimetric Froude number for estimating sediment transport", Journal of Hydraulic Engineering, 129 (6): 428-437.

Ai J. J., Law A. W. K. and Yu S. C. M. (2006) "On Boussinesq and non-Boussinesq starting forced plumes", Journal of Fluid Mechanics, 558: 357-386.

Bailey S. E., Schroeder P. and Ruiz C. (2004). Design of CAD pits in San José Lagoon, San Juan, Puerto Rico. Second LACCEI International Latin American and Caribbean Conference for Engineering and Technology (LACCEI'2004), Challenges and Opportunities for Engineering Education, Research and Development.

Barnett J. (1991) "The dynamics of buoyant releases in confined spaces". Ph.D. Thesis, Emmanuel College, University of Cambridge.

Bever A. J., MacWilliams M. L., Wu F., Andes L. and Conner C. S. (2014). Numerical modeling of sediment dispersal following dredge material placements to examine possible augmentation of the sediment supply to marshes and mudflats, San Francisco bay, USA. 33rd PIANC World Congress, San Francisco.

Bokuniewicz H. J., Gebert J., Gordon R. B., Higgins J. L. and Kaminsky P. (1978). Field Study of the Mechanics of the Placement of Dredged Material at Open-Water Disposal Sites. U.S. Army Engineer Waterways Experiment Station, Vicksburg, Miss.

Bonnecaze R. T., Hallworth M. A., Huppert H. E. and Lister J. R. (1995) "Axisymmetric particle-driven gravity currents", Journal of Fluid Mechanics, 294: 93-121.

Bonnecaze R. T., Huppert H. E. and Lister J. R. (1993) "Particle-driven gravity currents", Journal of Fluid Mechanics, 250: 339-369.

Brandsma M. G. and Divoky D. J. (1976). Development of models for prediction of short-term fate of dredged material discharged in the estuarine environment, Contract Report D-76-5, U.S. Army Engineer Waterways Experiments Station, Vicksburg, Miss.

Buhler J. and Papantoniou D. A. (1991) Swarms of coarse particles falling through a fluid. Rotterdam, Balkema.

Bühler J. and Papantoniou D. A. (2001) "On the motion of suspension thermals and particle swarms", Journal of Hydraulic Research, 39 (6): 643-653.

Burridge H. and Hunt G. (2012) "The rise heights of low-and high-Froude-number turbulent axisymmetric fountains", Journal of Fluid Mechanics, 691: 392-416.

Bush J. W. M., Thurber B. A. and Blanchette F. (2003) "Particle clouds in homogeneous and stratified environments", Journal of Fluid Mechanics, 489: 29-54.

Cenedese C. and Dalziel S. (1998). Concentration and depth fields determined by the light transmitted through a dyed solution. 8th International Symposium on flow visualisation, Sorrento, Italy.

Ching C. Y., Fernando H. J. S. and Noh Y. (1993) "Interaction of a negatively buoyant line plume with a density interface", Dynamics of Atmospheres and Oceans, 19 (1): 367-388.

Currie L. A. (1999) "Detection and quantification limits: origins and historical overview", Analytica Chimica Acta, 391 (2): 127-134.

Dade W. B. and Huppert H. E. (1995) "A box model for non‐entraining, suspension‐driven gravity surges on horizontal surfaces", Sedimentology, 42 (3): 453-470.

Dietrich W. E. (1982) "Settling velocity of natural particles", Water Resources Research, 18 (6): 1615-1626.

Diez F. J., Sangras R., Faeth G. M. and Kwon O. C. (2003) "Self-preserving properties of unsteady round buoyant turbulent plumes and thermals in still fluids", Journal of Heat Transfer, 125 (5): 821-830.

Dong C. D., Chen C. W., Chen C. F. and Kao C. M. (2007) "Mathematical modeling and simulation of ocean disposal of harbor dredged materials", Practice Periodical of Hazardous, Toxic, and Radioactive Waste Management, 11 (3): 207-213.

Eek E., Cornelissen G., Kibsgaard A. and Breedveld G. D. (2008) "Diffusion of PAH and PCB from contaminated sediments with and without mineral capping; measurement and modelling", Chemosphere, 71 (9): 1629-1638.

Eisma D. (2006) Dredging in coastal waters, Balkema: Proceedings and Monographs in Engineering, Water and Earth Sciences, Taylor & Francis Group.

EPA (2004). Evaluation of dredged material proposed for disposal in New England waters. E. R. 1. EPA Region 1, New England.

Fay J. A. (1969). The Spread of Oil Slicks on a Calm Sea. Oil on the Sea, Springer: 53-63.

Gensheimer R. J., Adams E. E. and Law A. W. K. (2012) "Dynamics of particle clouds in ambient currents with application to open-water sediment disposal", Journal of Hydraulic Engineering, 139 (2): 114-123.

Gladstone C. and Woods A. W. (2000) "On the application of box models to particle-driven gravity currents", Journal of Fluid Mechanics, 416: 187-195.

Gu J. and Li C. (2004) "Modeling instantaneous discharge of unsorted particle cloud in ambient water by an Eulerian-Lagrangian method", Journal of Hydraulic Research, 42 (4): 399-405.

Hallworth M. A., Hogg A. J. and Huppert H. E. (1998) "Effects of external flow on compositional and particle gravity currents", Journal of Fluid Mechanics, 359 (1): 109-142.

Harada E., Tsuruta N. and Gotoh H. (2013) "Two-phase flow LES of the sedimentation process of a particle cloud", Journal of Hydraulic Research, 51 (2): 186-194.

Ho S. and Rajabifard A. (2016) "Towards 3D-enabled urban land administration: Strategic lessons from the BIM initiative in Singapore", Land Use Policy, 57: 1-10.

Hogg A. J., Hallworth M. A. and Huppert H. E. (2005) "On gravity currents driven by constant fluxes of saline and particle-laden fluid in the presence of a uniform flow", Journal of Fluid Mechanics, 539: 349-385.

Hogg A. J., Ungarish M. and Huppert H. E. (2000) "Particle-driven gravity currents: asymptotic and box model solutions", European Journal of Mechanics - B/Fluids, 19 (1): 139-165.

Holford J. and Dalziel S. (1996) "Measurements of layer depth during baroclinic instability in a two-layer flow", Applied Scientific Research, 56 (2-3): 191-207.

Hoult D. P. (1972) "Oil Spreading on the Sea", Annual Review of Fluid Mechanics, 4 (1): 341-368.

Howlett E. (2003) "GIS-based tools in support of Dredging Operations", Sea Technology, 44 (3): 42-44.

Huber L. (2010). Validation of Analytical Methods.

Huppert H. E. (2006) "Gravity currents: a personal perspective", Journal of Fluid Mechanics, 554: 299-322.

Huppert H. E. and Simpson J. E. (1980) "The slumping of gravity currents", Journal of Fluid Mechanics, 99 (04): 785-799.

Janda A., Zuriguel I., Garcimartín A., Pugnaloni L. A. and Maza D. (2008) "Jamming and critical outlet size in the discharge of a two-dimensional silo", Europhysics Letters, 84 (4): 44002.

Johnson B. H. (1990). User's guide for models of dredged material disposal in open water, Technical Report D-90-5, U.S. Army Engineer Waterways Experiment Station, Vicksburg, Miss.

Johnson B. H. and Fong M. T. (1995). Development and Verification of Numerical Models for Predicting the Initial Fate of Dredged Material Disposed in Open Water. Report 2. Theoretical Developments and Verification Results, Tech. rep., DRP-93-1, U. S. Army Engineer Waterways Experiment Station, Vicksburg, MS.

Johnson B. H., Trawle M. J. and Adamec Jr S. A. (1988) "Dredged material disposal modeling in Puget Sound", Journal of Waterway, Port, Coastal, and Ocean Engineering, 114 (6): 700-713.

Johnson M. R., Boelke C., Chiarella L. A., Colosi P. D., Greene K., Lellis-Dibble K., Ludemann H., Ludwig M., McDermott S., Ortiz J., Rusanowsky D., Scott1 M. and Smith J. (2008) Impacts to marine fisheries habitat from nonfishing activities in the Northeastern United States. NOAA Tech Memo NMFS-NE-209, 322 p.

Jonasz M. and Fournier G. (2011) Light scattering by particles in water: theoretical and experimental foundations, Academic Press.

Kikkert G., Davidson M. and Nokes R. (2007) "Inclined Negatively Buoyant Discharges", Journal of Hydraulic Engineering, 133 (5): 545-554.

Kikkert G. A. (2006) "Buoyant jets with two and three-dimensional trajectories". Ph.D. Thesis, Civil Engineering, University of Canterbury.

Koh R. C. Y. and Chang Y. C. (1973) Mathematical model for barged ocean disposal of wastes, Tech. rep., U.S. Army Engineer Waterways Experiment Station, Vicksburg, Miss.

Konz M., Ackerer P., Huggenberger P. and Veit C. (2009) "Comparison of light transmission and reflection techniques to determine concentrations in flow tank experiments", Experiments in Fluids, 47 (1): 85-93.

Krishnappan B. G. (1975) Dispersion of granular material dumped in deep water. Burlington (Ont.) : Canada Centre for Inland Waters, Inland Waters Directorate.

Lackey T. and MacDonald N. (2007). The Particle Tracking Model Description and Processes. Proceedings XVIII World Dredging Congress 2007, Lake Buena Vista, Florida.

Lague D., Crave A. and Davy P. (2003) "Laboratory experiments simulating the geomorphic response to tectonic uplift", Journal of Geophysical Research: Solid Earth, 108 (B1): ETG 3-1-ETG 3-20.

Lai A. C. H., Wang R. Q., Law A. W. K. and Adams E. E. (2016) "Modeling and experiments of polydisperse particle clouds", Environmental Fluid Mechanics, 16 (4): 857-898.

Lai A. C. H., Zhao B., Law A. W. K. and Adams E. E. (2013) "Two-phase modeling of sediment clouds", Environmental Fluid Mechanics, 13 (5): 435-463.

Lavagnini I. and Magno F. (2007) "A statistical overview on univariate calibration, inverse regression, and detection limits: Application to gas chromatography/mass spectrometry technique", Mass spectrometry reviews, 26 (1): 1-18.

Lee J. H. W. and Chu V. H. (2003) Turbulent jets and plumes: a Lagrangian approach, Springer.

Leppinen D. and Dalziel S. (2001) "A light attenuation technique for void fraction measurement of microbubbles", Experiments in Fluids, 30 (2): 214-220.

Li C. (1997) "Convection of particle thermals", Journal of Hydraulic Research, 35 (3): 363-376.

Linden P. F. and Simpson J. E. (1990) "Continous two-dimensional releases from an elevated source", Journal of loss prevention in the process industries, 3 (1): 82-87.

Luketina D. and Wilkinson D. (1998). The transition to the swarm phase for a particle cloud. 13th Australasian Fluid Mechanics Conference, Melbourne, Australia.

Mankoc C., Janda A., Arevalo R., Pastor J., Zuriguel I., Garcimartín A. and Maza D. (2007) "The flow rate of granular materials through an orifice", Granular Matter, 9 (6): 407-414.

Middleton J. H. (1975) "The asymptotic behavior of a starting plume", Journal of Fluid Mechanics, 72: 753-771.

Miyamoto M., Tanaka S., Mitsuse M., Murata K. and Masui Y. (1993). Split barge, European Patent No. EP0362447 B1.

Morton B. R., Taylor G. and Turner J. S. (1956) "Turbulent gravitational convection from maintained and instantaneous sources", Proceedings of the Royal Society of London. Series A. Mathematical and Physical Sciences, 234 (1196): 1-23.

Munro R. and Dalziel S. (2005) "Attenuation technique for measuring sediment displacement levels", Experiments in Fluids, 39 (3): 602-613.

Munro R., Dalziel S. and Jehan H. (2004) "A pattern matching technique for measuring sediment displacement levels", Experiments in Fluids, 37 (3): 399-408.

Nguyen D. H., Levy F., Pham D. V. B., Guillou S., Nguyen K. D. and Chauchat J. (2012) "Simulation of dredged sediment releases into homogeneous water using a two-phase model", Advances in Water Resources, 48: 102-112.

Njifenju A. K., Bico J., Andrès E., Jenffer P. and Fermigier M. (2013) "Experimental investigation of liquid films in gravity-driven flows with a simple visualization technique", Experiments in Fluids, 54 (5): 1-9.

Noh Y. and Fernando H. J. S. (1993) "The transition in the sedimentation pattern of a particle cloud", Physics of Fluids A: Fluid Dynamics, 5 (12): 3049-3055.

Okada T., Larcombe P. and Mason C. (2009) "Estimating the spatial distribution of dredged material disposed of at sea using particle-size distributions and metal concentrations", Marine Pollution Bulletin, 58 (8): 1164-1177.

Papantoniou D., Bühler H. and Dracos T. (1990). On the internal structure of thermals and momentum puffs. International Conference on Physical Modelling of Transport and Dispersion, MIT.

Rahimipour H. (1994) "Studies into the motion of particle clouds". Ph.D. Thesis, Department of Water Engineering, University of New South Wales, Australia.

Rahimipour H. and Wilkinson D. (1992). Dynamic behaviour of particle clouds. Eleventh Australasian Fluid Mechanics Conference, Vols 1 and 2, University of Tasmania, Hobart, Australia, 743-746.

Rooij F. d., Dalziel S. B. and Linden P. F. (1999) "Electrical measurement of sediment layer thickness under suspension flows", Experiments in Fluids, 26 (5): 470-474.

Rottman J. W. and Simpson J. E. (1983) "Gravity currents produced by instantaneous releases of a heavy fluid in a rectangular channel", Journal of Fluid Mechanics, 135: 95-110.

Ruggaber G. J. (2000) "Dynamics of particle clouds related to open-water sediment disposal". Ph.D. Thesis, Department of Civil and Environmental Engineering, Massachusetts Institute of Technology, Cambridge MA.

Scorer R. S. (1957) "Experiments on convection of isolated masses of buoyant fluid", Journal of Fluid Mechanics, 2 (6): 583-594.

Shrivastava A. and Gupta V. B. (2011) "Methods for the determination of limit of detection and limit of quantitation of the analytical methods", Chronicles of Young Scientists, 2 (1): 21.

Sutherland B. R. and Dalziel S. (2014) "Bedload transport by a vertical jet impinging upon sediments", Physics of Fluids, 26 (3): 035103.

Taylor G. I. (1946) Dynamics of a mass of hot gas rising in air. Oak Ridge, Tenn., Technical Information Division, Oak Ridge Operations.

Tsang G. (1970) "Laboratory study of two-dimensional starting plumes", Atmospheric Environment (1967), 4 (5): 519-544.

Turner J. S. (1962) "The ‘starting plume’ in neutral surroundings", Journal of Fluid Mechanics, 13 (3): 356-368.

Turner J. S. (1973) Buoyancy Effects in Fluids, Cambridge University Press.

Ungarish M. and Zemach T. (2005) "On the slumping of high Reynolds number gravity currents in two-dimensional and axisymmetric configurations", European Journal of Mechanics-B/Fluids, 24 (1): 71-90.

USEPA/USACE (1991). Evaluation of Dredged Material Proposed for Ocean Disposal - Testing Manual. (The Green Book).

USEPA/USACE (1998). Dredged Material Proposed for Discharge in Waters of the U.S. (Inland Testing Manual).

Van Zoonen P., Van'T Klooster H., Hoogerbrugge R., Gort S. M. and Van De Wiel H. J. (1999) "Validation of analytical methods and laboratory procedures for chemical measurements", Arhiv za higijenu rada i toksikologiju, 49 (4): 355-370.

Wang D. Y. and Adams E. E. (2015) "Intrusion dynamics of small oil droplets from a deep ocean blowout in a weak current", Journal of Geophysical Research, accepted for publication.

Wang R. Q., Adams E. E., Law A. W. K. and Lai A. C. H. (2015) "Scaling Particle Cloud Dynamics: From Lab to Field", Journal of Hydraulic Engineering, 141 (7): 06015006.

Wang R. Q., Law A. W. K. and Adams E. E. (2014) "Large-Eddy Simulation (LES) of settling particle cloud dynamics", International Journal of Multiphase Flow, 67: 65-75.

Wen F. and Nacamuli A. (1996) "The effect of the Rayleigh number on a particle cloud", Hydrodynamics: 1275-1280.

White F. M. (1999) Fluid Mechanics. McGraw-Hill, New York.

Yoo Y., Im J. and Paik J. (2014) "Flicker removal for CMOS wide dynamic range imaging based on alternating current component analysis", Consumer Electronics, IEEE Transactions on, 60 (3): 294-301.

Yoshida J., Masuda N., Ito B., Furuya T. and Sano O. (2012) "Collision of a vortex ring on granular material. Part II. Erosion of the granular layer", Fluid Dynamics Research, 44 (1): 015502.

Yuan Y., Avener M. E. and Horner-Devine A. R. (2011) "A two-color optical method for determining layer thickness in two interacting buoyant plumes", Experiments in Fluids, 50 (5): 1235-1245.

Zgheib N. (2015) "Gravity currents from non-axisymmetric releases". Ph.D. Thesis, Institut National Polytechnique de Toulouse.

Zgheib N., Bonometti T. and Balachandar S. (2015) "Propagation and deposition of non-circular finite release particle-laden currents", Physics of Fluids, 27 (8): 086604.

Zhao B. (2014) "Sediment Disposal in Coastal Waters". Ph.D. Thesis, School of Civil and Environmental Engineering, Nanyang Technological University.

Zhao B., Law A. W. K., Adams E. E. and Er J. W. (2014) "Formation of particle clouds", Journal of Fluid Mechanics, 746: 193-213.

Zhao B., Law A. W. K., Adams E. E., Shao D. D. and Huang Z. H. (2012) "Effect of air release height on the formation of sediment thermals in water", Journal of Hydraulic Research, 50 (5): 532-540.

Zhao B., Law A. W. K., Huang Z. H., Adams E. E. and Lai A. C. H. (2013a) "Behavior of Sediment Clouds in Waves", Journal of Waterway, Port, Coastal, and Ocean Engineering, 139 (1): 24-33.

Zhao B., Law A. W. K., Lai A. C. H. and Adams E. E. (2013b) "On the internal vorticity and density structures of miscible thermals", Journal of Fluid Mechanics, 722: R5.

Appendix A

A. Examination of Classification Scheme

The development of sediment clouds due to open water sediment disposal is classified into three processes (P1 – P3) as illustrated in Figure 1.4. In Chapter 4, the P3 process is further distinguished into six different regimes (C1 – C6) as presented in Figure 4.2. To better understand and illustrate the relationship between P1 – P3 (process) and C1 – C6 (flow regime), Figure A.1 shows the development of sediment clouds disposed from round/point source (three-dimensional), which experience the three different development processes with the flow regimes (C1 – C6) marked respectively. In the following, the classification scheme will be discussed.

In the classification, the first step is to determine the type of release (instantaneous or continuous release) by comparing the z_{a-t} and z_e. z_{a-t} is the length of acceleration regime, which can be used to represent the influence of instantaneous release; and z_e is the empty depth, which represents the influence of continuous release. If the sediments are fully discharged before the sediment cloud front reaches the z_{a-t} ($z_{a-t} > z_e$), the sediment clouds will behave as instantaneous releases and experience P1 or P2 process, depending on the source cloud number, *Nc*. Otherwise, the sediment clouds will behave as a starting plume and descend with P3 process.

The formula of z_{a-t} can be derived from the length scale of acceleration regime, l_{a-t} proposed by Luketina and Wilkinson (1998):

$$l_{a-t} \sim (m_o / \rho_a)^{1/3} \tag{A.1}$$

where m_o is the mass of disposed sediment and ρ_a is the density of ambient fluid. The physical length of acceleration regime can generally be expressed as:

$$z_{a-t} = C_{a-t} l_{a-t} \qquad \text{(A.2)}$$

where the value of C_{a-t} is to be determined from the previous experimental studies with z_{a-t} is at the depth when the growth of sediment clouds starts to follow the asymptotic solutions. Table A.1 summarizes the value of C_{a-t} from four different studies, and is found to vary from 2.5 to 10.7. This significant variation can be attributed directly to the different source conditions of the disposed sediments. Here, a median value of 6.6 is used for the analysis. Note that z_e can be calculated from Equation (4.20).

Tables A.2 and A.3 examine the classification scheme by using the observations or results reported in the previous and present studies, respectively. The classification scheme is capable to classify most of the cases accurately with few exceptions, i.e. in Table A.3, Experiments A1LW05 and A2LW05 were predicted to experience the P1 process, yet starting plume regime was discovered at the beginning of the descent process. This might be due to the C_{a-t} under these source conditions having a lower value. In general, $C_{a-t} = 6.6$ can precisely classify most of the cases.

The application of classification scheme on the field conditions is exhibited in Table A.4. For the disposal with backhoe bucket, the amount of sediment involved is usually in the order of 1 m^3, depending on the bucket size. In the real operation, the sediments are usually lifted to mid-air before released, and the sediment discharge time can be estimated from the Beverloo equation. By discharging fine sand (close to slit), the disposed sediments are expected to descend as sediment clumps (P2 process). On the other hand, due to large amount of sediments involved (in the order of 1000 m^3) during the barge disposal, the disposed sediments shall descend as starting plumes first before transiting to discrete sediment thermals when the sediments are fully discharged (P3 process).

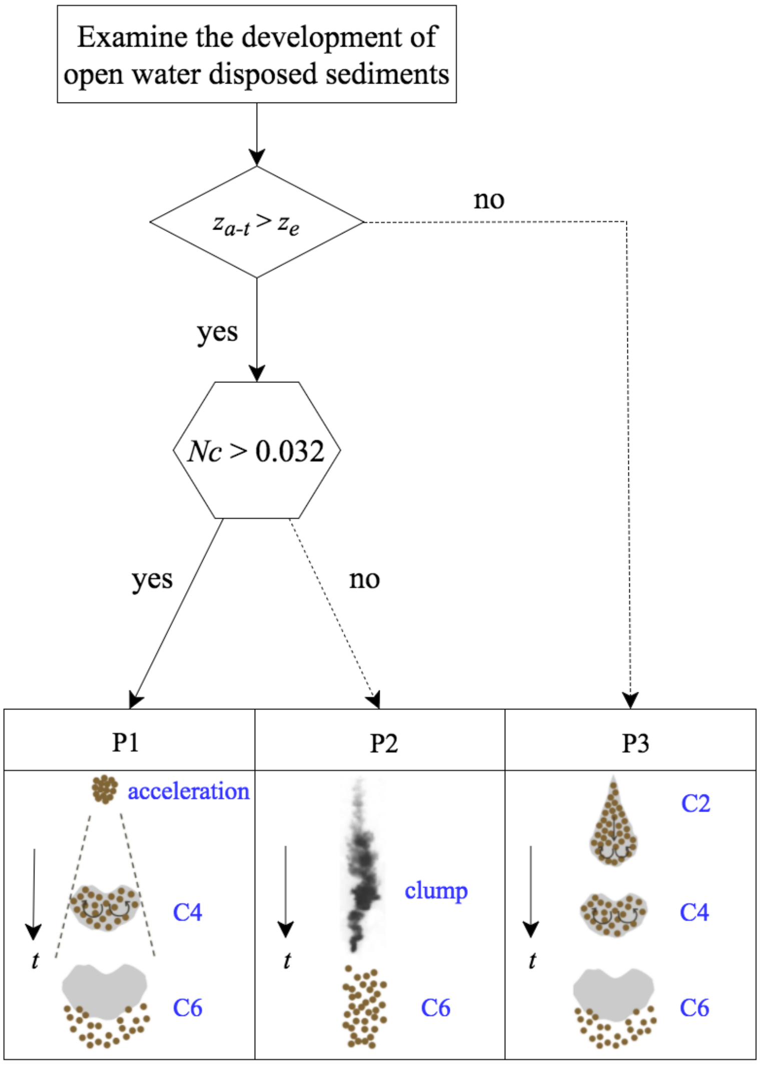

Figure A.1 Sediment cloud development processes in three-dimensional regimes

Table A.1 Summary of C_{a-t} from previous studies

Previous Studies	C_{a-t}
Luketina and Wilkinson (1998)	4.1
Gu and Li (2004)	10.7
Wang *et al.* (2014)	6.9 – 10.4
Zhao *et al.* (2012)	2.5 – 5.9

Table A.2 Examination of classification scheme with previous studies

m_o (g)	ρ_s g/cm3	d_{50} (mm)	w_s (cm/s)	Nc	z_{a-t} (cm)	z_e (cm)	Predicted Process	Verify (T/F)$^{\#}$
Rahimipour and Wilkinson (1992)								
5.5	2.65	0.2	2.1	3.4×10^{-2}	11.64	3.12	P1	T
12.2	2.65	0.33	5.1	8.3×10^{-2}	15.18	5.61	P1	T
Wen and Nacamuli (1996)								
199.8	1.39	1.25	4.4	7.2×10^{-2}	38.58	4.47	P1	T
83.5	2.65	0.11	1.3	1.3×10^{-2}	28.85	9.99	P2	T
Bühler and Papantoniou (2001)								
86.1	2.6	1.95	18.8	3.9×10^{-1}	29.14	4.76	P1	T
44.7	2.6	1.95	18.8	2.2×10^{-1}	23.42	4.01	P1	T
21.5	2.6	1.95	18.8	2.5×10^{-1}	18.35	3.34	P1	T
Gu and Li (2004)								
7.8	2.6	0.89	14	2.2×10^{-1}	13.09	2.74	P1	T
7.8	2.6	0.45	6.3	9.7×10^{-2}	13.09	3.37	P1	T
Zhao *et al.* (2012)								
8.4	2.5	0.513	7.13	1.1×10^{-1}	13.42	2.98	P1	T
Zhao *et al.* (2014)								
5.5	2.5	0.256	2.92	5.0×10^{-2}	11.65	2.88	P1	T
5.5	2.5	0.12	0.93	1.6×10^{-2}	11.65	3.59	P2	T
5.5	2.5	0.068	0.35	6.0×10^{-3}	11.65	4.36	P2	T
448	2.5	0.256	2.92	2.4×10^{-3}	50.50	12.63	P2	T

Note: For the sediments disposed from air, the discharged time (t_e) is calculated from the Beverloo equation (Mankoc *et al.* 2007)

$^{\#}$ T: same development process reported in the study; F: different process reported

Table A.3 Examination of classification scheme with present experiments

Test notation[##]	Nc or Ncc	z_{a-t} (cm)	z_e (cm)	Predicted Process	Verify (T/F)
Chapter 4					
A1LW05	1.1×10^{-1}	31.81	18.50	P1	F
A1LW40	1.1×10^{-1}	31.81	36.74	P3	T
A2LW05	7.4×10^{-2}	31.81	22.58	P1	F
A2LW40	7.4×10^{-2}	31.81	44.84	P3	T
A3LW05	3.0×10^{-2}	31.81	33.69	P3	T
A3LW40	3.0×10^{-2}	31.81	66.92	P3	T
A4LW05	9.7×10^{-3}	31.81	52.13	P3	T
A4LW40	9.7×10^{-3}	31.81	103.5	P3	T
Chapter 5					
MC1/MC2/LA1/LA2	1.4×10^{-2}	11.85	16.71	P3	T
Chapter 7					
N2_D1AH5	1.3×10^{-2}	10.32	2.08	P2	T
N2_D5AH1	4.2×10^{-2}	10.32	2.08	P1	T
N3_B1AH5	2.6×10^{-2}	12.23	3.19	P2	T
N3_D5AH1	3.5×10^{-2}	12.23	3.19	P1	T
N4_B1AH5	2.2×10^{-2}	12.23	3.19	P2	T
N4_A1AE3	6.3×10^{-2}	12.23	2.61	P1	T
N5_A1AH7	3.0×10^{-2}	12.23	3.19	P2	T
N5_E1	6.7×10^{-2}	12.23	3.19	P1	T

Note: t_e (z_e) for the experiments from Chapter 7 are computed based on the smallest sediment used in the respective experiments, which is also the maximum t_e (z_e)

[##] For the purpose of demonstration, only certain tests are shown here

Table A.4 Application of classification scheme on field conditions

m_o (g/kg/ton)	ρ_s g/cm^3	d_{50} (mm)	w_s (cm/s)	Nc	$z_{a\text{-}t}$ (cm)	z_e (cm)	Predicted Process
Laboratory experiments							
10 g	2.5	0.256	2.92	4.5×10^{-2}	14.22	1.86	P1
100 g	2.5	0.256	2.92	3.1×10^{-2}	30.63	12.91	P2
Field – backhoe bucket (bucket size: 1 m × 1 m)							
1000 kg (~ 1 m^3)	2.5	0.068	0.35	8.0×10^{-4}	660.0	132.2	P2
Field – bottom-split barge (barge dimensions: 1000 m × 10 m × 1 m)							
1000 ton (~ 1000 m^3)	2.5	0.068	0.35	2.5×10^{-4}	6600	12388	P3

Note: In the laboratory study, the sediments are assumed to release through a cylindrical tube with an opening of 1.8 cm

Appendix B

B. Asymptotic Solution for 2D Sediment Thermal

A 2D thermal is the motion formed when a line of buoyant fluid is released from rest instantaneously (Lee and Chu 2003) as illustrated in Figure B.1. The motion of the line thermal can be described by an integral model tracking the change in its mass per unit length $m_{2\mathrm{D}T}$, momentum per unit length $M_{2\mathrm{D}T}$ and buoyancy per unit length $b_{2\mathrm{D}T}$.

$$\frac{dm_{2\mathrm{D}T}}{dt} = 2\pi\gamma r_T \alpha_{2\mathrm{D}T} \rho_a u_f \tag{B.1}$$

$$\frac{dM_{2\mathrm{D}T}}{dt} = b_{2\mathrm{D}T} \tag{B.2}$$

$$\frac{db_{2\mathrm{D}T}}{dt} = 0 \tag{B.3}$$

where $m_{2\mathrm{D}T} = \rho V_{2\mathrm{D}T} /L$; $M_{2\mathrm{D}T} = (1+C_M)\rho\pi\gamma r_T^2 u_f$; $b_{2\mathrm{D}T} = V_{2\mathrm{D}T}(\rho-\rho_a)g/L$; $V_{2\mathrm{D}T} = LA_{2\mathrm{D}T} = \pi\gamma r_T^2 L$ is the total volume; $A_{2\mathrm{D}T}$ is the cross-sectional area of the line thermal; ρ is the mean density of the sediment thermal; and γ is the height to width ratio of the sediment thermal. Lee and Chu (2003) suggested γ =0.69 and $C_M = 1$ for a two-dimensional thermal, and the same values are adopted in the present study. Equation (B.1) is based on the entrainment assumption (i.e. the rate of entrainment at the edge is proportional to the characteristic velocity of the thermal) by Morton *et al.* (1956). The proportionality constant is referred to as the entrainment coefficient, denoted as $\alpha_{2\mathrm{D}T}$ in Equation (B.1). Equation (B.2) is based on the conservation of momentum due to buoyancy and added mass (C_M); and Equation (B.3) is based on the assumption that there is no buoyancy loss to the wake and thus $b_{2\mathrm{D}T}$ is a constant ($b_{2\mathrm{D}T} = b_o = (\rho_s - \rho_a)gV_o/L$).

The above equations can be solved analytically within the Boussinesq range (i.e. $\rho \approx \rho_a$), with initial conditions applied at the virtual point source (i.e. $z_f = z_{o2}$, $r_T = 0$, and $M_{2\mathrm{D}T} = 0$ at $t = t_{o2}$), yielding:

$$r_T = \alpha_{2\mathrm{D}T}\left(z_f - z_{o2}\right) \tag{B.4}$$

$$z_f = \left(\frac{3b_o}{2\left(1+C_M\right)\pi\gamma\alpha_{2\mathrm{D}T}^{\ 2}}\right)^{1/3}\left(t-t_{o2}\right)^{2/3} + z_{o2} \tag{B.5}$$

Equations (B.4) and (B.5) describe the growth and penetration behaviour of the two-dimensional sediment thermal. Lee and Chu (2003) deduced the value of $\alpha_{2\mathrm{D}T}$ to be 0.46, which is similar to the growth rate of two-dimensional sediment thermal observed in the experiments of Noh and Fernando (1993). By substituting $\gamma = 0.69$, $C_M = 1$ and $\alpha_{2\mathrm{D}T} = 0.46$, the frontal velocity, u_f can be derived by differentiating Equation (B.5) and expressed as:

$$u_f = 0.79 b_o^{1/3}\left(t-t_{o2}\right)^{-1/3} \tag{B.6}$$

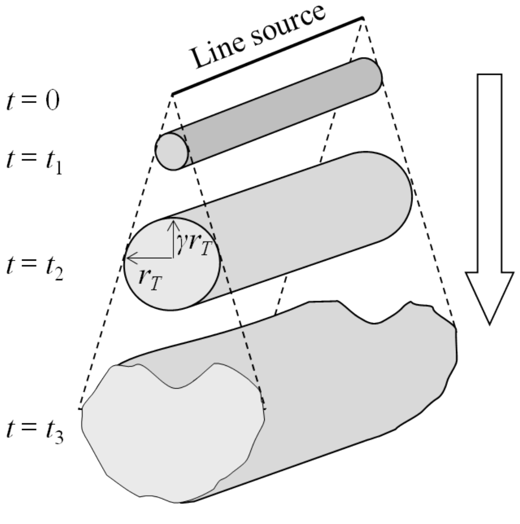

Figure B.1 Line thermal generated by releasing a cylinder of negatively buoyant material instantaneously

Appendix C

C. Asymptotic Solution for 3D Sediment Thermal

The model for the three-dimensional sediment thermal is based on the assumptions that the discrete solid and water phases within the sediment thermal can be approximated as a miscible dense fluid with equivalent buoyancy excess, and the Boussinesq approximation can be adopted (Ruggaber 2000). The governing equations of the model can be simplified by neglecting the effect of added mass and drag forces as suggested by Bush *et al.* (2003) yielding:

$$\frac{dm_{3\mathrm{D}T}}{dt} = \eta 4\pi\alpha_{3\mathrm{D}T} r_T^{\,2} \rho_a u_f \tag{C.1}$$

$$\frac{dM_{3\mathrm{D}T}}{dt} = B_{3\mathrm{D}T} \tag{C.2}$$

$$\frac{dB_{3\mathrm{D}T}}{dt} = 0 \tag{C.3}$$

where $m_{3\mathrm{D}T}$ is the total mass of a sediment thermal including both solid and liquid phases; $M_{3\mathrm{D}T}$ is the momentum; $B_{3\mathrm{D}T}$ is the excess buoyancy (i.e. $B_{3\mathrm{D}T} = (\rho - \rho_a) gV_{3\mathrm{D}T}$); $V_{3\mathrm{D}T} = 4\pi\eta r_T^3/3$ is the sediment thermal total volume where η is a shape factor to account for the non-spherical shape of the cloud as an oblate ellipsoid with width r_T and height ηr_T. Scorer (1957) suggested that $\eta = 9/4\pi$ and the same value is applied in present study. Note that Equation (C.3) is based on the assumption that no sediment loss is induced by the wake and thus that the total buoyancy force, $B_{3\mathrm{D}T}$ is a constant ($B_{3\mathrm{D}T} = B_o = (\rho_s - \rho_a)\, gV_o$).

The above equations can be solved analytically within the Boussinesq range (i.e. $\rho \approx \rho_a$) and applying the initial conditions at the virtual point source (i.e. $z_f = z_o$, $r = 0$, and $M_{3\mathrm{D}T} = 0$ at $t = t_o$), the solution can be expressed as:

$$r_T = \left(\frac{3\alpha_{3\mathrm{D}T} B_{\mathrm{o}}}{2\pi\eta} \right)^{1/4} \left(t - t_{o3} \right)^{1/2} \tag{C.4}$$

$$z = \left(\frac{3B_{\mathrm{o}}}{2\pi\eta\alpha_{3\mathrm{D}T}^{3}} \right)^{1/4} \left(t - t_{o3} \right)^{1/2} + z_{o3} \tag{C.5}$$

Equations (C.4) and (C.5) describe the size and penetration behaviour of the 3D sediment thermal, respectively. By substituting $\eta = 9/4\pi$ and $\alpha_{3\mathrm{D}T} = 0.25$ (Bush et al., 2003), the frontal velocity, u_f can be derived by differentiating Equation (C.5) as:

$$u_f = 1.28 B_{\mathrm{o}}^{1/4} \left(t - t_{o3} \right)^{-1/2} \tag{C.6}$$

Using Equation (C.5), Equation (C.4) can also be expressed as:

$$r_T = \alpha_{3\mathrm{D}T} \left(z_f - z_{o3} \right) \tag{C.7}$$

Appendix D

D. Two-Dimensional modified Box-Model and Determination of Coefficients

The Box-Model for two-dimensional gravity currents also consists of three main equations, which are presented below as Equations (D.1): the conservation of area, (D.2): a Froude number condition at the current head, and (D.3): the law of sedimentation.

$$a = h_o x_o = h_c x_c \tag{D.1}$$

$$u_c = \mathrm{d}x_c/\mathrm{d}t = \mathrm{Fr}\,(g'h_c)^{1/2} \tag{D.2}$$

$$\frac{\mathrm{d}a\varphi}{\mathrm{d}t} = -\,w_s \varphi x_c \tag{D.3}$$

where a is the area of gravity current in the rectangle, h_o and x_o are the initial height and width of the current, g' is the reduced gravitational acceleration, h_c is the current height, φ is the particle volume fraction and w_s is the particle settling velocity. The analytical solution of the above equations was derived by Dade and Huppert (1995).

To account for the constant flux due to the sediment plume, equations (D.1) and (D.3) have to be modified respectively:

$$\frac{\mathrm{d}a}{\mathrm{d}t} = u_f r_o \tag{D.4}$$

$$\frac{\mathrm{d}a\varphi}{\mathrm{d}t} = -\,w_s \varphi x_c + q_{2\mathrm{D}} \tag{D.5}$$

where the right hand side of equation (D.4) is the volume flux from the plume, u_f and r_o are the plume downward velocity and radius, q_{2D} is the sediment flux per unit length. We normalized the lengths, times, velocities and particle volume fraction by h_o (= 0.72 r_o), $(h_o/g_o')^{1/2}$, $(h_o g_o')^{1/2}$ and φ_o, where φ_o is the initial volume fraction. Note that, h_o, g_o', φ_o, r_o, u_f, and q_{2D} are computed from BSDM. Using uppercase symbols to represent dimensionless variables (e.g. $A = a/h_o^2$), the normalized governing equations can be expressed as:

$$\frac{\mathrm{d}A}{\mathrm{d}T} = U_f R_o \tag{D.6}$$

$$\frac{\mathrm{d}\Phi}{\mathrm{d}T} = -\frac{\beta\Phi}{H} + \frac{Q_{2D}}{A} - \frac{\Phi U_f R_o}{A} \tag{D.7}$$

$$\frac{\mathrm{d}X_c}{\mathrm{d}T} = \mathrm{Fr} H_c^{\ 1/2} \Phi^{1/2} \tag{D.8}$$

Equation (D.7) explains the elements that affect the sediment concentration in the gravity current. The first term on the right hand side represents the sedimentation rate. The second and third terms show the impacts of the sediment plume with the former denoting the increment in sediments due to the sediment flux. However, the sediment plume also increases the total area of the gravity current and hence dilutes the sediment concentration at the same time.

Equation (D.8) is an empirical law established by Huppert and Simpson (1980) to account for the complicated three-dimensional dynamics in the current head. Fr is dependent on h_c/h, where h is the water depth, in the following manner: (i) Fr = 1.19 when $h_c/h < 0.075$, and (ii) Fr = $C_1 (h_c/h)^{-1/3}$ when $0.075 \leq h_c/h < 1$. The current study is in this latter region. The value of C_1 was found to vary between 0.52 and 0.67 based on different studies. Here, we noticed that the value of C_1 is affected by the mechanism of how the buoyant fluids are released. We determined C_1 with the experimental data from Hallworth *et al.* (1998) and Nguyen *et al.* (2012), which had a similar setup as the current study. A value of 1.2 was found to best fit the data and the comparison of the results is shown in Figure D.1.

As discussed in Section 6.2.1, the deposition thickness can be computed from the second term of Equation (D.7) by collectively summing up the amount of sediments settled at each time. The sediments are assumed to be distributed in an exponentially decay manner as shown in Equation (6.14) with the h_s at source (h_{so}) can be expressed as Equation (6.15). By simulating the Bonnecaze *et al.* (1993)'s results, C_3 with a value of 8 was found to best fit the experimental results as shown in Figure D.2. The predicted sediment thickness near the source region (x < 75 cm) was over-estimated, especially for the case with larger amount of sediments (400 g). When x > 75 cm, the experimental results were under-predicted, yet the subsequent decreasing trend in h_s was well predicted. The slight deviation might be due to the fact that the present assumption on the sediment distribution was for constant flux gravity currents, whereas the gravity currents reported in Bonnecaze *et al.* (1993) were constant volume. Therefore, lesser sediments (from the constant flux) settled near the source region.

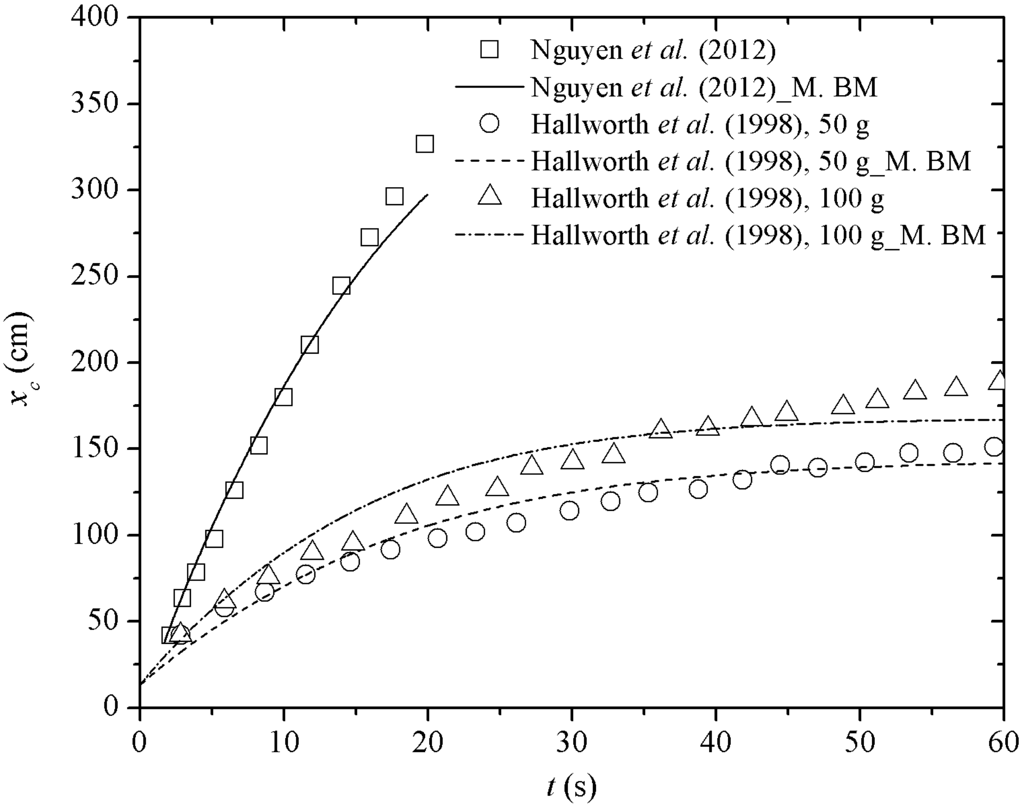

Figure D.1 Comparison between experimental results from previous studies and model predictions for M. BM with C_1 = 1.2

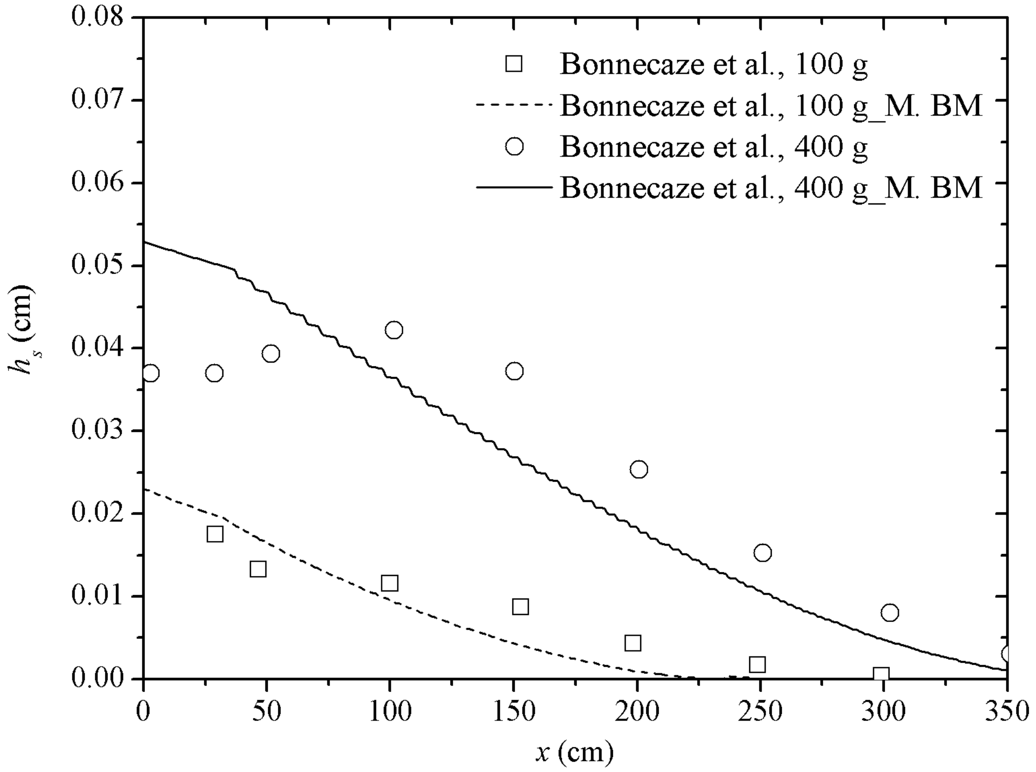

Figure D.2 Comparison between experimental results from Bonnecaze *at al.* (1993) and model prediction for M. BM with $C_3 = 8$